nature biomedical engineering

Article

https://doi.org/10.1038/s41551-023-01038-w

Stretchable ultrasonic arrays for the three-dimensional mapping of the modulus of deep tissue

Received: 28 January 2021

Accepted: 5 April 2023

Hongjie Hu[1,2,12], Yuxiang Ma[2,12], Xiaoxiang Gao[2,12], Dawei Song[3,12], Mohan Li[2], Hao Huang[2], Xuejun Qian[4], Ray Wu[2], Keren Shi[1], Hong Ding[2], Muyang Lin[2], Xiangjun Chen[1], Wenbo Zhao[5], Baiyan Qi[1], Sai Zhou[1], Ruimin Chen[4], Yue Gu[1], Yimu Chen[2], Yusheng Lei[2], Chonghe Wang[2], Chunfeng Wang[2], Yitian Tong[6], Haotian Cui[7], Abdulhameed Abdal[8], Yangzhi Zhu[2], Xinyu Tian[1], Zhaoxin Chen[2], Chengchangfeng Lu[6], Xinyi Yang[1], Jing Mu[1], Zhiyuan Lou[2], Mohammad Eghtedari[9], Qifa Zhou[4], Assad Oberai[10] & Sheng Xu[1,2,6,9,11] ✉

Serial assessment of the biomechanical properties of tissues can be used to aid the early detection and management of pathophysiological conditions, to track the evolution of lesions and to evaluate the progress of rehabilitation. However, current methods are invasive, can be used only for short-term measurements, or have insufficient penetration depth or spatial resolution. Here we describe a stretchable ultrasonic array for performing serial non-invasive elastographic measurements of tissues up to 4 cm beneath the skin at a spatial resolution of 0.5 mm. The array conforms to human skin and acoustically couples with it, allowing for accurate elastographic imaging, which we validated via magnetic resonance elastography. We used the device to map three-dimensional distributions of the Young's modulus of tissues ex vivo, to detect microstructural damage in the muscles of volunteers before the onset of soreness and to monitor the dynamic recovery process of muscle injuries during physiotherapies. The technology may facilitate the diagnosis and treatment of diseases affecting tissue biomechanics.

The mechanical properties of human tissues are vital for the structure and function of human physiological systems[1]. Frequent mechanical characterizations of various organs allow timely evaluation of tissue growth, metabolic state, immunologic function and hormone regulation[1–3]. Most importantly, the mechanical properties of diseased tissues can often reflect pathophysiological conditions. The monitoring of such properties can provide key information about disease progression, and guide intervention in a timely manner[4,5]. For instance, the

---

[1]Materials Science and Engineering Program, University of California San Diego, La Jolla, CA, USA. [2]Department of Nanoengineering, University of California San Diego, La Jolla, CA, USA. [3]Institute for Medicine and Engineering, University of Pennsylvania, Philadelphia, PA, USA. [4]Department of Biomedical Engineering, University of Southern California, Los Angeles, CA, USA. [5]Department of Osteology and Biomechanics, University Medical Center Hamburg-Eppendorf, Hamburg, Germany. [6]Department of Electrical and Computer Engineering, University of California San Diego, La Jolla, CA, USA. [7]Department of Computer Science, University of Toronto, Toronto, Ontario, Canada. [8]Department of Mechanical and Aerospace Engineering, University of California San Diego, La Jolla, CA, USA. [9]Department of Radiology, School of Medicine, University of California San Diego, La Jolla, CA, USA. [10]Department of Aerospace and Mechanical Engineering, University of Southern California, Los Angeles, CA, USA. [11]Department of Bioengineering, University of California San Diego, La Jolla, CA, USA. [12]These authors contributed equally: Hongjie Hu, Yuxiang Ma, Xiaoxiang Gao, Dawei Song. ✉e-mail: shengxu@ucsd.edu

stiffnesses of tumours are known to be different from those of healthy tissues[6]. Additionally, in some tumours, changes in stiffness can occur as they grow in certain developmental stages[7], and these changes can happen quickly (Supplementary Fig. 1a and Supplementary Note 1)[5,8–12]. Frequent inspections of the stiffness of these tumours are required for growth-stage assessment and therapy guidance[13]. Mechanical characterization is also critical in the diagnosis and rehabilitation of many musculoskeletal diseases and injuries. The monitoring of muscular moduli enables more proactive screening of the area at risk (Supplementary Fig. 1b)[14–22]. Surveillance of tissue moduli has also been demonstrated to help with early detection and tracking of cardiovascular diseases[23,24]. An ideal technology should provide non-invasive and three-dimensional (3D) mapping of deep tissues with accurate location, morphology and mechanical information[25]. However, existing methods are unable to address this critical need (Supplementary Figs. 2–5 and Supplementary Note 2).

In this article, to fill this technological gap, we report a stretchable ultrasonic array with advances in device engineering and imaging algorithms (Supplementary Note 3). With new microfabrication protocols, we can achieve excellent transducer electromechanical coupling. The coherent compounding imaging strategy enables accurate displacement calculations, and therefore enhances elastographic signal-to-noise ratio (SNR_e) and contrast-to-noise ratio (CNR_e) in the entire sonographic window[26]. By solving an inverse elasticity problem, we can derive quantitative modulus distribution, which is a leap forward compared with the qualitative strain distribution obtained with conventional quasi-static elastography[27] (Supplementary Note 4). We show the reliability of this technology by testing on various artificial phantom models and ex vivo biological specimens, with quantitative validation by magnetic resonance elastography (MRE). In vivo studies on delayed-onset muscle soreness shows that this technology can track the recovery progress of muscular injury in a non-invasive serial manner, providing therapeutic guidance. These results suggest a convenient and effective approach to monitor tissue mechanical properties, facilitating the diagnosis and treatment of many diseases and symptoms.

Results

Working principle, design and fabrication of the device

Measurements by traditional rigid ultrasound probes may suffer from poor acoustic coupling, because their rigid surfaces cannot accommodate the curvilinear shape of the human body (Supplementary Note 5). To solve this problem, we designed a stretchable ultrasonic array for modulus sensing. Figure 1a shows the schematic working mechanism of a 16-by-16 array (for the detailed process, see Supplementary Figs. 6 and 7 and Supplementary Movie 1). The array can conform to and acoustically couple with the human skin via a type of silicone-based couplant for high-quality imaging (Supplementary Fig. 5 and Supplementary Note 5). After the array is activated, ultrasound waves are sent into the tissue underneath the device. Scattering sources (for example, tissue interfaces) can reflect the ultrasound waves, which carry location information of these scattering sources. The reflected waves are then received by the transducer elements in the array as radiofrequency data. The collected radiofrequency data by each element are then enhanced by receive beamforming (Supplementary Fig. 8). After that, ~0.5–1% strain is applied to the tissue by quasi-static uniaxial compression. The low strain ensures that the tissues exhibit linear stress–strain behaviour—that is, their Young's modulus does not vary with load[28]. After compression, the maximum change in the array's pitch is only 0.02% (Supplementary Fig. 9). Therefore, the associated phase aberration is negligible for both transmit and receive beamforming, especially for deep-tissue inspections (Supplementary Note 6 and Supplementary Figs. 10 and 11). As a result, we can use the same time-delay profile for both post- and pre-compression receive beamforming (Supplementary Note 6). A normalized cross-correlation algorithm is used to compare the radiofrequency data before and after compression, and calculate the displacements of the scattering sources with high sonographic sensitivity and accuracy (Supplementary Note 7 and Supplementary Fig. 12a,b)[29,30]. A least-squares strain estimator is used to transform displacements to strain while minimizing possible fluctuations (Supplementary Note 8 and Supplementary Fig. 12)[31]. A graphical user interface that consists of real-time display windows and control panels is designed for locating the device and quantifying the compression to the subject (Supplementary Note 9 and Supplementary Fig. 13). An inverse elasticity problem is solved to quantify the modulus distribution inside the tissue (Supplementary Note 10).

We choose a centre frequency of 3 MHz to balance the requirement of high spatial resolution[32] and frequency-dependent linear attenuation of ultrasound waves in tissues[33]. The characterized mean resonant and anti-resonant frequencies show small standard deviations, indicating the consistency across the entire array (Fig. 1b). Given the corresponding ultrasound wavelength of ~500 µm in soft tissues, we choose a pitch of 800 µm that is suitable for generating wave convergence[34], producing high-quality images and minimizing crosstalk[35]. The pitch is altered upon conformation to a curvature. However, in this study, we continue using the initial planar pitch of 800 µm in the beamforming of a curved surface, due to the negligible changes of no more than 0.003% in the pitch within the adoptable curvature range of the array (Supplementary Note 11 and Supplementary Fig. 14). A scalable method is used to align the backing material and the transducer elements, which enhances the fabrication throughput and performance consistency, and avoids potential phase aberrations (Supplementary Fig. 15 and Methods)[35,36]. To individually address the 256 elements, six layers of activation electrodes and one layer of common ground in a serpentine shape are transfer-printed and routed to the same plane by vertical interconnect accesses (Supplementary Figs. 16–18). A low-temperature bonding technique is used to preserve the high electromechanical coupling coefficient of the 256 elements (average 0.64, Fig. 1b inset), with performance comparable to elements in commercial ultrasound probes (0.58–0.69) (ref. 37). The 0.022 of average dielectric loss of the array indicates the energy consumption caused by transducer heating is minimal (Supplementary Fig. 19). The time- and frequency-domain characterizations of pulse-echo response show ~50% bandwidth (Supplementary Fig. 19 and Methods).

Because of the well-designed pitch, the suppression of shear vibrations by the 1–3 composite, and the damping effect of silicone elastomer between the elements, crosstalk between the elements is below the standard −30 dB (Fig. 1c). A matching circuit effectively reduces the insertion loss to 16.98 dB at the resonant frequency (Supplementary Fig. 20), comparable to a commercial probe (17 dB) (ref. 38). The low insertion loss leads to excellent sonographic sensitivity (Fig. 1d), which is pivotal for modulus imaging[39]. The high-performance 1–3 composite material, together with the new fabrication protocol and effective matching circuit, results in an average sonographic signal-to-noise ratio of 39 dB, comparable to a commercial probe (41 dB) (ref. 39). The standard deviation of the sonographic signal-to-noise ratio measured underwater for 2 weeks is small (0.87 dB), because of the excellent waterproof property of the encapsulating silicone elastomer (Supplementary Fig. 21). The device can be reversibly deformed in various modes (Fig. 1e–g). The maximum biaxial stretchability of the device without affecting its electromechanical properties is ~40%, indicating its reliability for skin integration (Supplementary Figs. 22 and 23)[40].

Strategies for elastography

To determine the transmission mode for elastography, we simulated two-dimensional (2D) strain distributions in a bilayer phantom under three different transmission modes: single plane wave, mono-focus and coherent plane-wave compounding (Supplementary Fig. 24)[26], and then analysed the SNR_e and CNR_e, the two most critical metrics for modulus mapping (Supplementary Notes 12 and 13)[41]. Among the

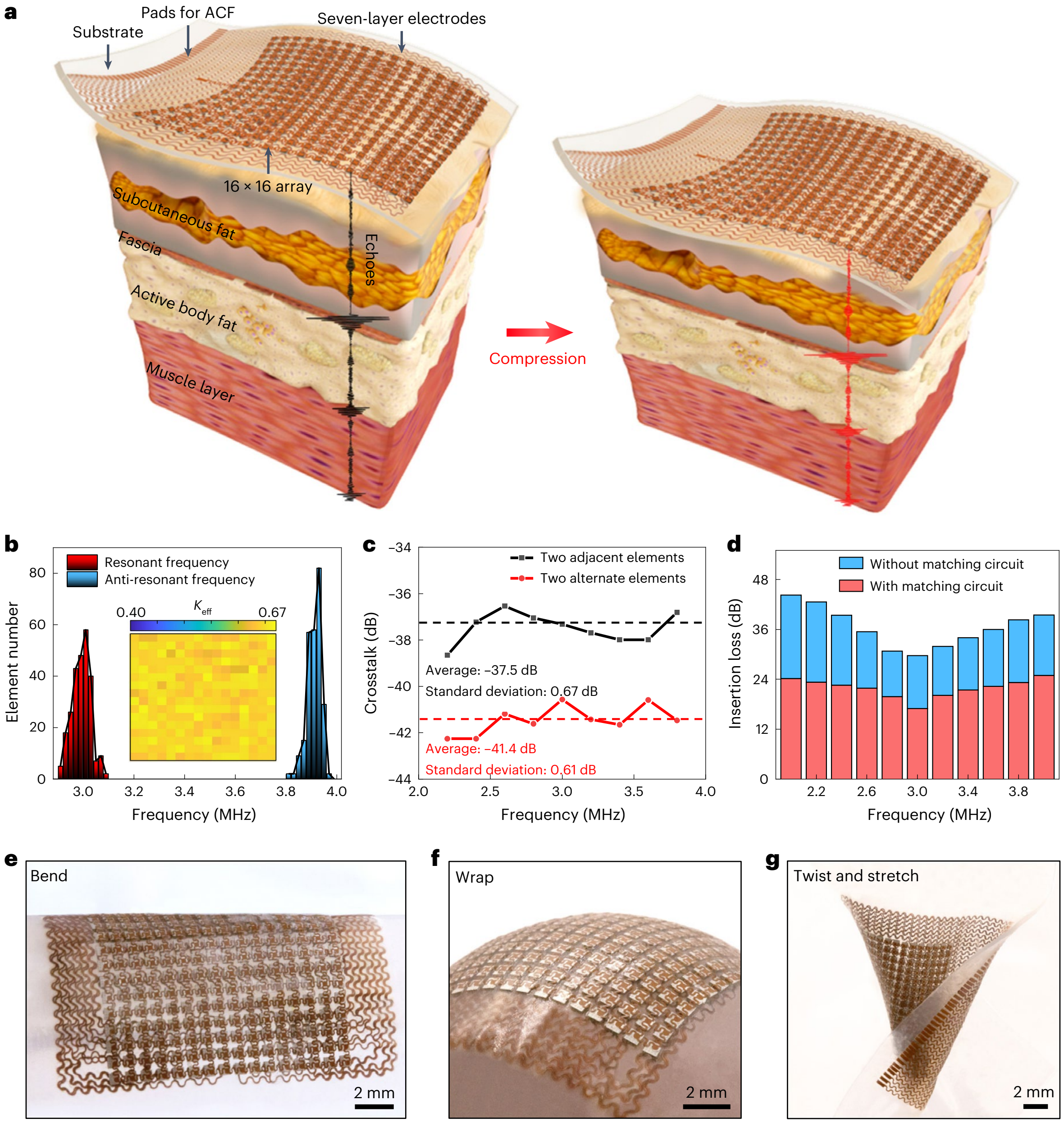

Fig. 1 | Working principle, design and fabrication of the stretchable ultrasonic array. **a**, Schematics of the stretchable ultrasonic array laminated on a soft tissue. The device consists of a 16-by-16 array of transducer elements connected in-parallel by a seven-layer electrode and encapsulated with waterproof and biocompatible silicone elastomer. The exploded view of each element is in Supplementary Fig. 6, showing the structure and components of the element. This layout allows activation of each element individually with a particular time-delay profile and capture of the reflected echoes from scattering sources, pre- (left) and post-compression (right). The beamformed pre- and post-compression signals are cross-correlated to derive the displacement, strain and modulus fields. ACF, anisotropic conductive film. **b**, Resonant frequency, anti-resonant frequency and calculated effective electromechanical coupling coefficient (K_{eff}) distribution (inset) of the 256 elements. **c**, Evaluation of the crosstalk between two adjacent elements and two alternate elements. **d**, Insertion loss of the transducers with and without the matching circuit. The insertion loss has a minimum value at the resonant frequency because of the maximum electrical power generated by the echoes. **e**–**g**, Optical images of the device when bent (**e**) or wrapped (**f**) on complex-shaped surfaces, and twisted and stretched (**g**), showing its mechanical compliance and robustness.

three modes, the single plane wave mode produces the lowest SNR_e and CNR_e, because of the low transmission energy from non-focal scanning (Fig. 2a). The mono-focal mode provides better SNR_e and CNR_e, but only in regions near the focal point. The coherent plane-wave compounding mode consists of a series of single plane waves at different transmission angles, and these steered frames are coherently integrated to reconstruct a multi-angle compounding image, with multiplexed signal intensities across the entire region (Supplementary Note 13). The resulting SNR_e and CNR_e levels are substantially enhanced in all regions[26]. The performance of the compounding strategy highly depends on the step size and the number of the steering angles. In this work, we used 19 steering angles and a step size of 1°, which were found in experiments to give the best elastographic image quality (Fig. 2b,c and Supplementary Figs. 25 and 26).

A high SNR_e is critical for high-quality elastographic imaging. The SNR_e is influenced by the magnitude of applied strain and the normalized cross-correlation coefficient (NCC), which reflects the similarity of the radiofrequency signals before and after compression. The smallest

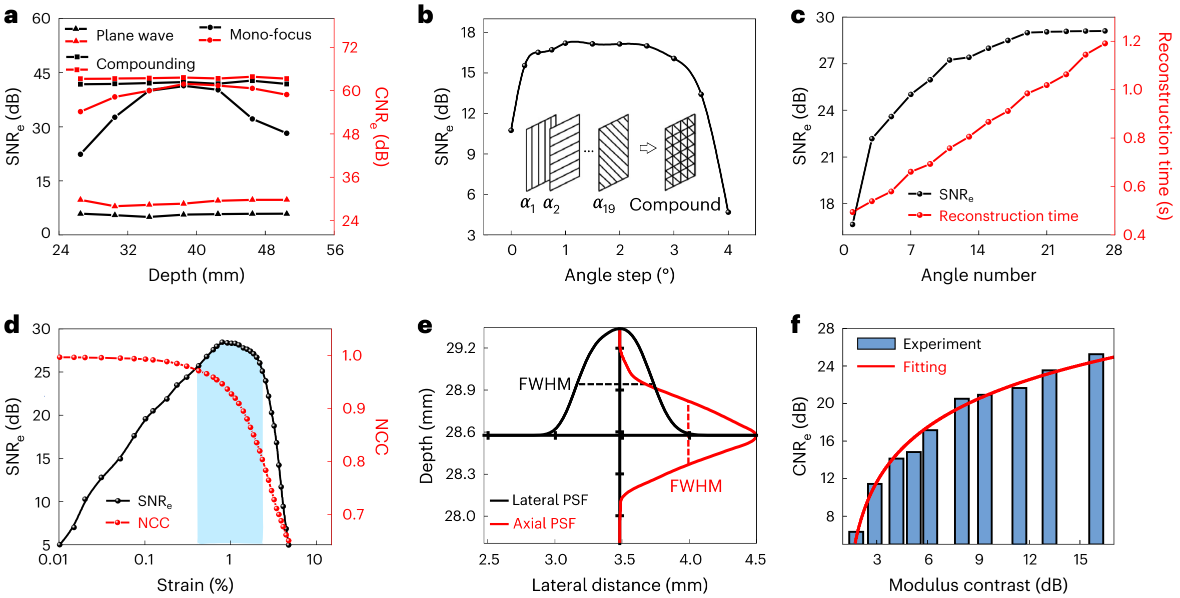

Fig. 2 | Strategies for elastography. **a**, Simulations showing the SNR$_e$ and CNR$_e$ of the coherent plane wave compounding, mono-focus and single plane wave transmission modes in a bilayer phantom. These data are extracted at seven different depths along the central line of strain images in Supplementary Fig. 24. **b**, The SNR$_e$ as a function of the step size of the steering angle. Inset is a schematic diagram showing the process of compounding: a set of plane waves are transmitted with different steering angles and a final compounded image is built by coherently adding all beamformed images. **c**, The SNR$_e$ and reconstruction time with different numbers of steering angles. **d**, The SNR$_e$ and NCC as a function of applied strain. In NCC, data were normalized by the product of the standard deviations of pre- and post-compression signals. The shaded area with >0.8 NCC by a −3 dB strain filter shows the dynamic range. **e**, Lateral and axial resolutions of the stretchable ultrasonic array based on the FWHMs of PSFs. **f**, Quantification of the contrast resolution based on the relationship between the CNR$_e$ and modulus contrast of phantoms.

detectable strain with an SNR$_e$ of 6 dB is 0.0125%, which indicates the high elastographic sensitivity of the stretchable array (Fig. 2d). At low strain levels, the displacement signals are small, so the relatively large intrinsic electrical noise in the radiofrequency signals leads to large deviations in the elastographic images and thus a low SNR$_e$. As the applied strain increases, the displacement signals increase proportionally, while the intrinsic electrical noise remains relatively constant, leading to an increase in the SNR$_e$. The SNR$_e$ becomes the highest at ~1% strain. Beyond 1% strain, the radiofrequency signals distort in shape and amplitude[42], resulting in a sharp fall in the NCC and therefore SNR$_e$ (Fig. 2d). The dynamic range (that is, the strain range with high SNR$_e$) is determined by a −3 dB cut-off from the maximum SNR$_e$, which is ~0.36–2.34% in this work, corresponding to a NCC >0.8.

Both spatial resolution and contrast resolution are critical for elastographic imaging[43]. To characterize the spatial resolution, we imaged the modulus distribution and extracted the lateral and axial transition edges of an inclusion phantom (Supplementary Fig. 27 and Methods). The first derivatives of the modulus distribution yield the point spread functions (PSFs) (Supplementary Fig. 28), whose full widths at half maximum (FWHMs) are used to estimate the elastographic spatial resolutions[25], which are determined to be 0.56 mm in the lateral and 0.50 mm in the axial directions (Fig. 2e). Because of the synthetic focusing effect of the coherent plane-wave compounding mode, the spatial resolution remains high and consistent at different locations across the entire imaged region[26].

Similar to the spatial resolution, the contrast resolution is defined as the modulus contrast with a corresponding CNR$_e$ of 6 dB. To quantify the contrast resolution, we perform tests on bilayer phantoms, composed of two homogeneous gelatin phantoms with different elastic moduli. The modulus of each layer is within ~10–100 kPa, covering the modulus range of all typical healthy and diseased tissues (Supplementary Fig. 29)[44], which creates an interfacial modulus contrast ranging from 1.79 dB to 15.94 dB. The CNR$_e$, determined by the ratio of the strain contrast to the standard deviation of strain distribution, decreases as the modulus contrast becomes lower (Fig. 2f and Supplementary Note 12). Logarithmic curve fitting, with a coefficient of determination >0.98, demonstrates the reliability of the experimental results (Supplementary Note 12)[43]. The contrast resolution of the device is determined to be ~1.79 dB (that is, a modulus ratio of 1.22).

Characterizations on phantom models

Following the clinical practice for tumour screening and diagnosis, we used four types of phantom to simulate different pathological tissue environments (Supplementary Fig. 27)[43,45]: a one-dimensional phantom consisting of two layers with different Young's moduli, which mimics muscles with an area of disease or injury[15,17]; a 2D phantom consisting of a cylindrical cavity filled with fluid, which simulates cysts that frequently appear in central organs[46]; a 2D phantom with a solid cylindrical inclusion; and a commercial 3D breast phantom with a spherical mass. The last two phantoms mimic tumours and nodes with various morphologies in the breast[47]. Young's moduli of all components have been characterized by either standard apparatus (for customized phantoms, Supplementary Fig. 29) or a clinical ultrasound machine (for the commercial phantom, see Supplementary Fig. 30). Many masses (except for the cyst phantom) have materials and constituents, and thus acoustic impedances, similar to the surrounding tissues. Thus, they exhibit a homogeneous echogenicity and a minimal sonographic contrast that can be hardly distinguished by B-mode imaging (Fig. 3a–d, first column)[48,49].

The tests on phantom models focus on the axial displacement fields (Fig. 3a–d, second column). Compared with the lateral and elevational displacements, the axial displacements can reflect the movement of each scattering source more accurately, because it is parallel to the direction of ultrasonic wave transmission[50]. The strain is higher when the modulus of the component is lower (the third column in Fig. 3a–d and Supplementary Note 8). A common practice for computing strain

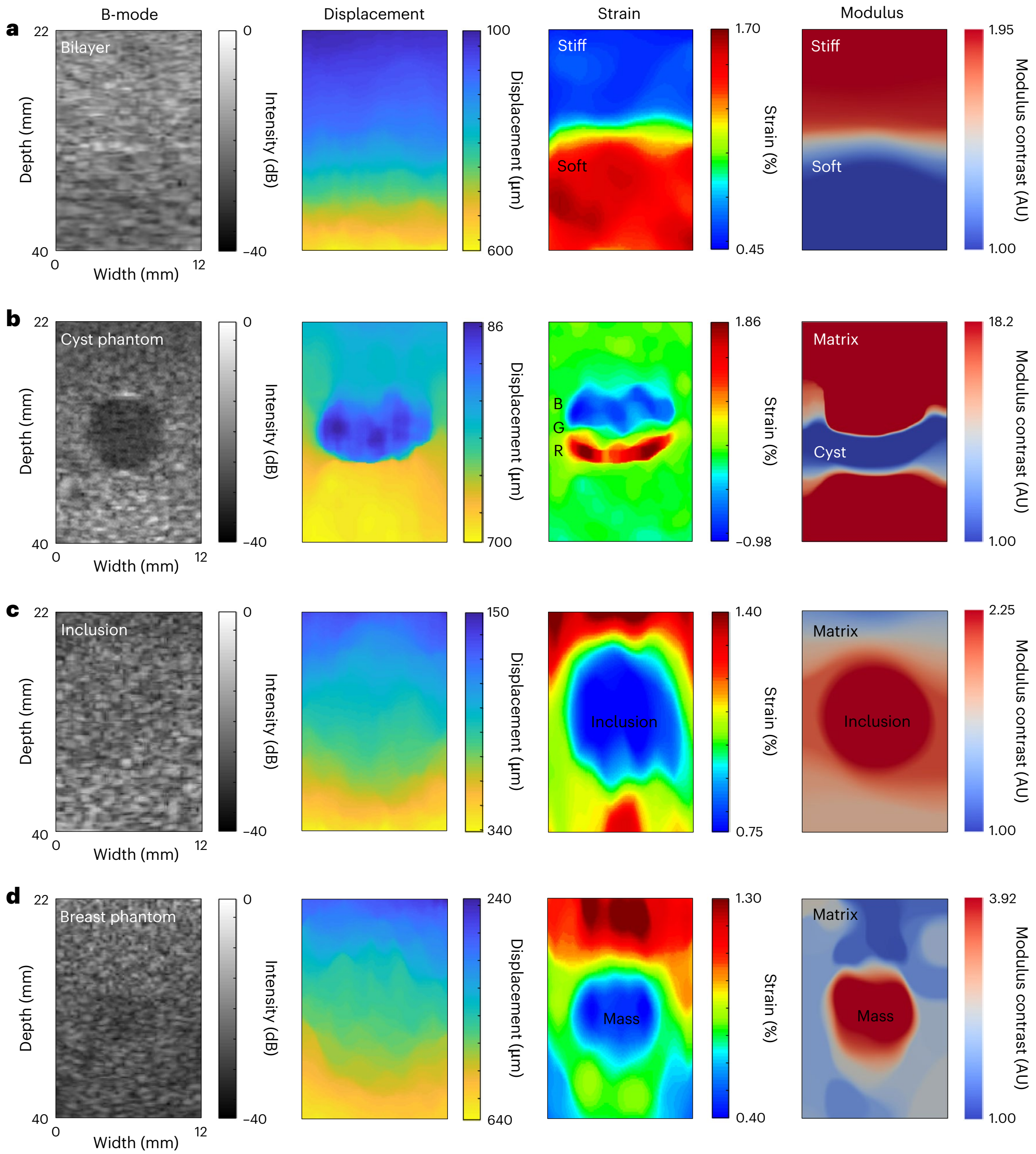

Fig. 3 | Characterizations on phantom models. a–d, Four types of phantom are used to simulate different pathological tissue environments: a bilayer phantom where the top layer is 2.03 times stiffer than the bottom layer (**a**), a cyst phantom consisting of a cylindrical cavity filled with fluid (**b**), phantoms with a cylindrical inclusion that is 1.61 times stiffer than the matrix (**c**) and a spherical mass that is 2.54 times stiffer than the matrix (**d**). B-mode images of all phantoms acquired by a commercial ultrasound probe are shown in the first column. Displacement fields estimating the motion of each scattering source in the phantoms during compression are shown in the second column. The ultrasonic array's position is defined as the origin. Corresponding strain distributions are shown in the third column. Solving the inverse elasticity problem with the displacement distributions yields quantitative modulus contrasts, shown in the fourth column.

is to take the spatial derivative of the displacement field[51], which amplifies small unphysical fluctuations in the displacement field (Supplementary Fig. 12). To remedy this problem, we applied a least-squares strain estimator with a piecewise linear curve fitting method, which allows us to calculate the 2D strain distributions while smoothing unphysical fluctuations (Supplementary Fig. 12)[52]. The resulting strain distributions clearly reveal the inclusion. An exception is the cyst phantom, whose strain distribution map has a blue (B)–green (G)–red (R) region (Supplementary Figs. 31 and 32), a signature of cysts that has been used clinically to distinguish between cystic and solid lesions[46,53]. We reconstructed 3D strain images of the phantoms by integrating 16 cross-sectional images obtained by the array. The 3D imaging results match those of a commercial ultrasound probe with a similar centre frequency (2.8 MHz) (Supplementary Figs. 33–36 and Supplementary Note 14). The measurements are highly reproducible, reflecting the reliability of the stretchable array (Supplementary Fig. 37).

Strain depends on applied loads, and thus strain mapping can be subjective and operator dependent. Additionally, strain maps cannot faithfully reveal quantitative modulus information if the load is non-uniform[54]. To avoid these issues, we quantify the spatial distribution of the shear modulus by solving an inverse elasticity problem[55]. Specifically, we formulate the inverse elasticity problem as a constrained optimization problem. The objective is to seek a shear modulus distribution that produces a predicted displacement field that both satisfies the equilibrium equation of the 2D linear elasticity model[56] and matches the measured displacement field. We solve the optimization problem by a gradient-based minimization approach and compute the gradient efficiently using the adjoint method (Supplementary Fig. 38)[55]. The Young's modulus is three times the shear modulus[57,58]. For a measured displacement field, the derived modulus distribution can be accurately determined. Note that the non-uniform external compressions do not influence the reconstructed modulus distribution because the inverse approach does not assume a uniform stress field to a given cross-section (Supplementary Note 10 and Extended Data Fig. 1).

The modulus distribution maps visualize the morphology of the internal structures, which accurately match the design (the fourth column of Fig. 3a–d). Shadowing artefacts, usually caused by inclusions (Supplementary Fig. 39), do not appear in the mapping results here, because of the high transmission energy of the coherent compounding method and the excellent sonographic sensitivity of the stretchable ultrasonic array. The mean modulus contrasts between the stiff and soft components of the bilayer, inclusion and breast phantoms are 1.94, 1.50 and 2.21, with a difference of 4.59%, 6.81% and 12.78%, respectively, from those obtained by a standard apparatus. Note that, for the cyst phantom, the acquired values indicate only that the stiffness of the cyst is much lower than that of the surrounding matrix, and do not represent the exact modulus ratios (Supplementary Note 15)[59]. There is a slight underestimation of modulus contrast in all cases because the total variation regularization used to solve the inverse elasticity problem tends to sacrifice the contrast to generate less noisy images (Supplementary Fig. 40)[60]. The overall >87% accuracy of the results here is well above the average accuracy of 80% in the literature[27], because of the outstanding transducer performance and the advanced coherent compounding approach.

Validation and serial monitoring on biological tissues

We validated the 3D imaging performance of the stretchable array against MRE on 4-cm-thick, multi-layered porcine abdominal tissues[61]. Each 1 × 16 linear array in the ultrasonic patch can map a 2D cross-sectional displacement field and the corresponding modulus distribution (Supplementary Fig. 41). A 3D elastographic image is reconstructed by integrating 16 slices of modulus maps with a 0.8 mm pitch (Fig. 4a), with an average discrepancy between the measured and predicted displacement fields of 3% (Fig. 4b and Methods). The 3D image illustrates the heterogeneous nature of the soft tissue. The same porcine abdominal tissue is then measured by MRE (Fig. 4c and Methods). The volumetric mapping result from the stretchable array is highly comparable to that from MRE in both morphology and modulus distribution. The average measured modulus contrasts of transversus abdominis muscle, obliquus internus abdominis muscle, fascia and intermuscular fat are approximately 1.92:1.67:1.30:1 by the stretchable array, and 2.26:1.83:1.46:1 by MRE; both are comparable to those in the literature[62,63].

A method for serial surveillance needs to be stable for long-term reproducibility, with a high sensitivity for picking up dynamic changes in the target tissue. A longitudinal study is carried out by testing a commercial phantom with the stretchable ultrasonic array and a commercial probe over 8 weeks. We compared the strain contrast between the mass and matrix measured by the two methods and conducted Bland–Altman analysis. All data points are within 95% confidence interval, showing excellent agreement between the stretchable array and the commercial probe. Additionally, a small bias error of 0.02 shows the high accuracy of the stretchable array and a small precision error of 0.09 indicates the stability of the device for repeated measurements over the long term (Fig. 4d and Supplementary Fig. 42). To test the elastographic sensitivity of the stretchable array, we measure a piece of bovine gluteobiceps muscle[64] under controlled unilateral heating as its modulus gradually increases (Supplementary Fig. 43). The measurement lasts for 165 min. The results clearly show that, before heating, the tissue has a low modulus across the entire depth (Fig. 4e). When heated from the bottom, the region of the tissue close to the heat source starts to stiffen, because the actin in the myofibrils becomes firm and short, expelling liquid and making the structure dense[65]. As the heating continues, the high-modulus region gradually grows, while the boundary between the high- and low-modulus regions remains clearly defined. These recordings demonstrate the capability of the stretchable array for serial monitoring of deep tissue mechanics.

Multi-site mapping of the human body

In vivo measurements can further illustrate the clinical value of the stretchable ultrasonic array. Multiple sites on the human body where muscle injuries usually happen are selected in this study (Supplementary Note 16 and Supplementary Fig. 44). Figure 5a–d shows the results of strain mapping within 4 cm depth from the lateral side of the shoulder joint (Fig. 5a), the anterior forearm (Fig. 5b), the anterior thigh (Fig. 5c) and the posterior calf (Fig. 5d) with the anatomies labelled, juxtaposed with the corresponding B-mode images acquired by a commercial probe. The stretchable array can effectively resolve the mechanical properties of various tissue components (Supplementary Figs. 45 and 46).

Testing on ten more volunteers confirmed the feasibility and reliability of the stretchable ultrasonic patch (Supplementary Note 16 and Supplementary Fig. 47). To verify the reliability of this device, we performed intra-session and inter-day testing on six participants[66] (Extended Data Fig. 2). To quantitatively evaluate those results, we calculated the mean values of the biceps brachii region in the strain images and used a two-way mixed-effect model[67] to derive the intraclass correlation coefficient[67] and standard error of measurement[68] (Supplementary Table 1), which indicate excellent relative and absolute reliabilities[66], respectively, of using the stretchable ultrasonic device for mapping deep-tissue modulus.

Serial surveillance of delayed-onset muscle soreness

Over-exercise introduces injuries to the musculoskeletal system, associated with damages in the sarcolemma and others[69]. These disruptions lead to inflammation, stiffness increase and function impairment of the tissues[69]. Very often, the sensation of soreness does not occur until a few days later[70]. The delayed onset of body responses precludes timely treatments, and the injury often gets neglected and worsens. There are several studies that have reported modulus variation of the muscle after the eccentric exercise[19,71,72]. However, the initial test was performed 1 h after the participants had exercised, while by that time, muscle damage might have already occurred, making it impossible to pinpoint the exact time of the initial muscle damage. Additionally, the modulus changes were only sporadically tested over a period[19], which was easy to miss the turning point in the change of the muscular modulus and failed to offer accurate trends of muscle recovery. Additionally, serial evaluation of the tissue can guide the rehabilitation strategy[71,72]. MRE is often used to evaluate the tissue stiffness to diagnose any injuries[71,72]. However, MRE is not viable for long-term testing, due to its large size, limited availability and high cost.

The stretchable ultrasonic array addresses these needs. A healthy volunteer was selected to perform eccentric elbow joint exercise to develop delayed-onset muscle soreness[73] (Fig. 5e, Supplementary Fig. 48 and Supplementary Note 17). Before exercise, well-defined anatomic components of the upper arm can be visualized in 3D (Supplementary Figs. 49 and 50). After exercise, the muscles are either allowed to recover naturally, or treated with massotherapy or hyperthermia. In all experiments, the normalized modulus contrast of the biceps brachii is surveyed every day for 5 days to track the dynamic recovery process. Meanwhile, the intensity of the soreness is evaluated on the

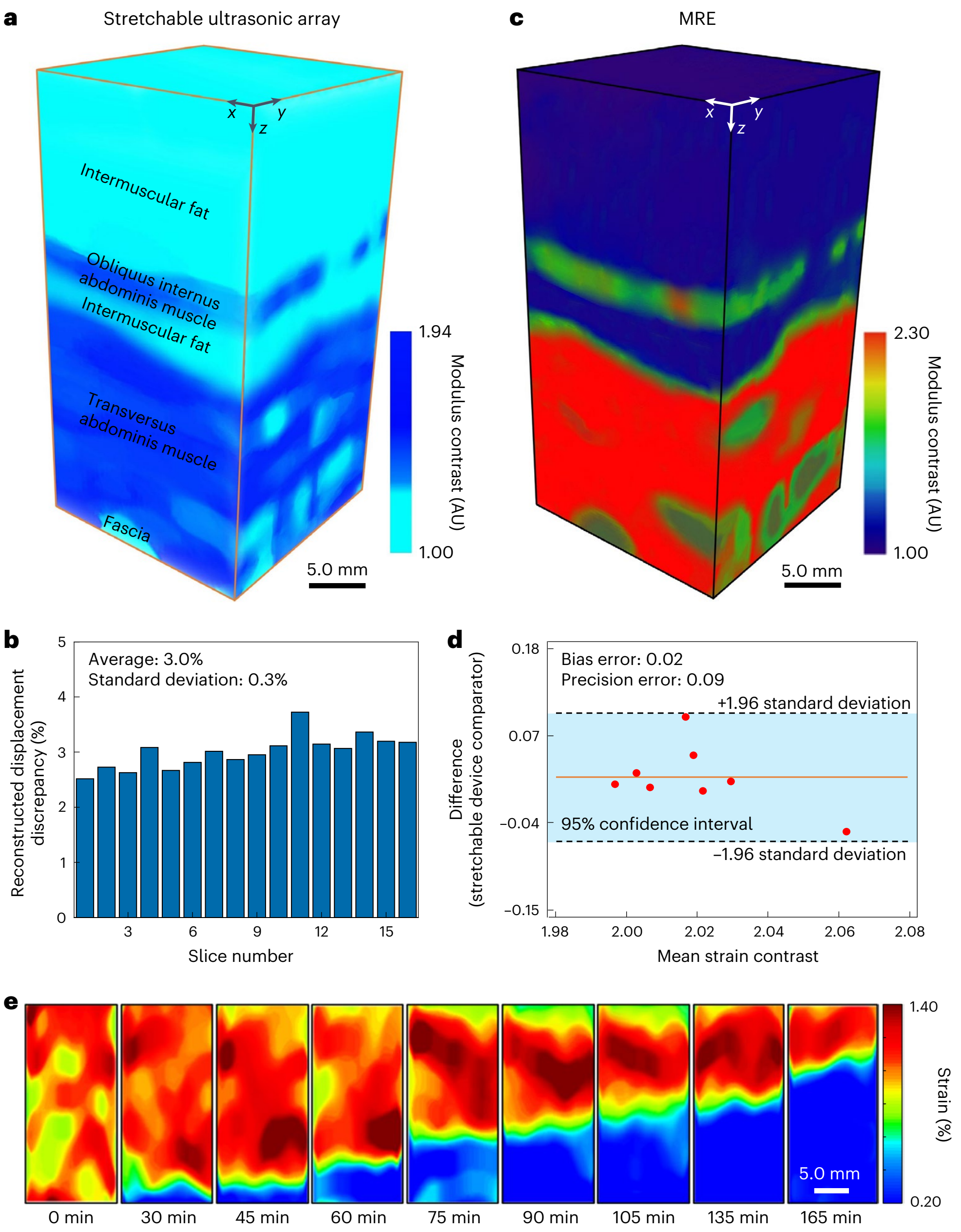

Fig. 4 | Validation and serial monitoring on biological specimens. **a**, A 3D quantitative elastographic image of a porcine abdominal tissue by the stretchable ultrasonic array. In the tissue, two muscle layers intersect with the intermuscular fat, and the fascias are embedded in the transversus abdominis muscle. The 3D elastogram embodies homogeneous, lower modulus fat layers made of glycerol and fatty acids molecules, and relatively heterogeneous muscle groups with higher modulus made from criss-crossing and confluence fibres. **b**, The average 3% discrepancy of the 16 pairs of measured and predicted displacement fields, with a high degree of correspondence between the reconstructed mechanical model by solving the inverse elasticity problem and the experimental conditions, suggesting a robust foundation for yielding the accurate modulus distributions. **c**, A 3D MRE image of the porcine abdominal tissue. **d**, Bland–Altman analysis of the strain contrast of a commercial breast phantom for 8 weeks. Each data point represents the difference in the measured strain contrasts between the stretchable ultrasonic array and the commercial probe. **e**, Time-dependent stiffness variation of a piece of bovine gluteobiceps muscle under controlled unilateral heating.

basis of the pain visual analogue scale[19] (Supplementary Fig. 48). Wearing the device 1 h per day for 5 days does not induce any skin irritation (Supplementary Fig. 51).

Figure 5f shows the monitoring results, where normalized modulus contrast (top) and soreness intensity score (bottom) of each measurement are collected. The modulus of biceps brachii increases within 20 min after the exercise due to the muscle contracture induced by sarcolemmal disruption (Supplementary Note 17)[71,72]. However, the sensation of soreness does not arise until 1 day after exercise (Supplementary Note 17)[74]. As more time goes by, sarcolemmal disruption continues, and the muscle modulus keeps increasing. Meanwhile, the circulation system delivers supplies to repair the sarcolemma, and eventually tissue modulus drops (Supplementary Note 17)[75]. During natural recovery, the muscle modulus continues to increase for 2 days before dropping. When physiotherapies are applied, the increase sustains for only 1 day, with lower maximum moduli. The intensity of soreness has a latency but evolves in a trend similar to the modulus. The experiments have been performed on more participants, and the results are

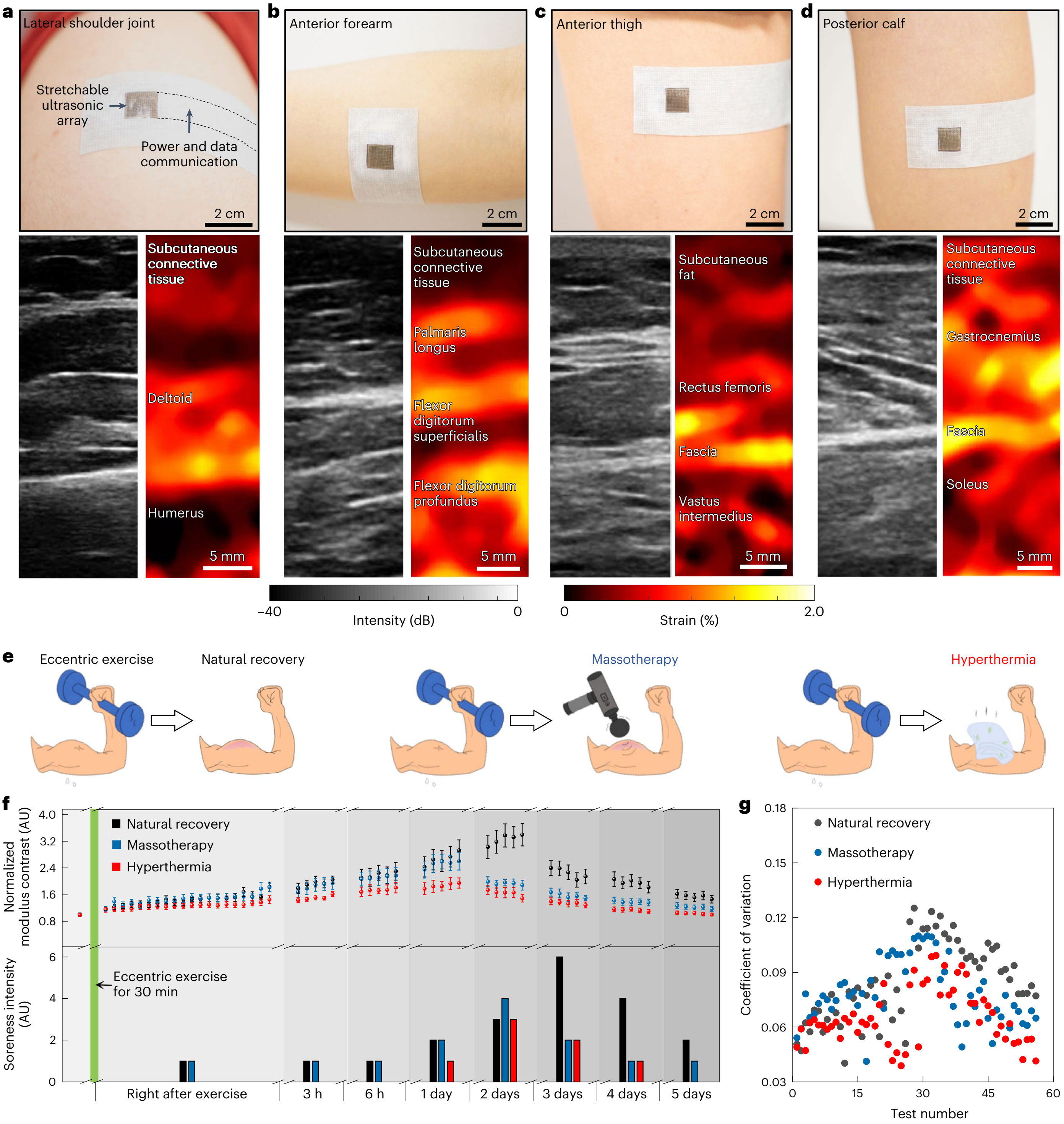

Fig. 5 | Multi-site mapping and serial surveillance of delayed-onset muscle soreness in human. a–**d**, Optical images, B-mode images and corresponding strain mapping results of a lateral shoulder joint (**a**), an anterior forearm (**b**), an anterior thigh (**c**) and a posterior calf (**d**). Key anatomical structures are labelled in the strain images. **e**, Schematics showing the exercise and physiotherapy protocols. **f**, Serial monitoring results of normalized modulus contrast and soreness intensity of the biceps brachii muscle before and after the eccentric exercise. We map the modulus distribution of the muscle and then calculate the mean and standard deviations of the biceps brachii area, which are plotted at the top. Each point and error bar represent the result of one measurement. The time interval between adjacent tests is 1 min. In each physiotherapy session, data are normalized by the modulus contrast of the biceps brachii muscle before exercise. At the bottom, soreness scores are evaluated following the pain visual analogue scale. **g**, Coefficient of variation of all tests. The lowest variation of the hyperthermia therapy indicates its best efficacy in recovering muscle injuries.

similar (Extended Data Fig. 3). Blood cannot circulate well through the injured myofibrils, leading to involuntary tremors of the muscle during testing[76], which induces variations in the measured modulus results. The coefficient of variation, defined as the ratio of the standard deviation to the mean, is smaller for physiotherapies than that of the natural recovery (Fig. 5g). These findings show the quicker healing pace of physiotherapies compared with natural recovery (Supplementary Note 18). The stretchable ultrasonic array demonstrates the feasibility of effectively monitoring the tissue stiffness under different muscle conditions.

We expand the sample size and use maximal voluntary contraction, a standard clinical approach to evaluate muscle activity[77], as a comparator to quantify the degree of the muscle damage after eccentric exercise (Supplementary Note 16). There is a notable drop in maximal voluntary contraction torque after doing the exercise followed by a gradual increase, which indicates the process of muscle damage followed by recovery (Extended Data Fig. 4)[78]. This trend corresponds to that of the modulus contrast variation, showing the reliability of the stretchable ultrasonic array to detect muscle activity (Extended Data Fig. 4). *P* value is the probability of one result equalling another under the assumption that the null hypothesis is correct. *P* values of both methods are all much less than 0.001, which further confirm this conclusion.

Discussion

The stretchable ultrasonic array can perform serial, non-invasive 3D mapping of the mechanical properties of deep tissues, which has not been realized by any existing devices. The array has high SNR_e, CNR_e, spatial resolution and contrast resolution, which can be attributed to the strategic array design, new microfabrication techniques and the effective ultrasound transmitting mode. Solving the inverse elasticity problem provides accurate and reliable quantitative information of modulus distribution in a 3D tissue. The stretchable ultrasonic array can detect muscle injuries before the subject's own feeling, and therefore enable timely intervention to prevent cumulative trauma disorders. Moving beyond muscle injuries, this technology has the potential to monitor the size and modulus of tumour in real time and inform therapeutic decisions, providing a new profiling method for both fundamental oncology research and clinical practice. Collectively, these findings demonstrate that the stretchable ultrasonic array is complementary to existing clinical monitoring modalities and can be used as a unique enabling technology for quantitatively sensing and treating many deep-tissue conditions.

Future developments may leverage advanced lithography, dicing and pick-and-place techniques to further optimize the array design and fabrication, which can reduce the pitch and extend the aperture to achieve a higher spatial resolution and a broader sonographic window. Additionally, the stretchable ultrasonic array is currently wired for data and power transmission. Those back-end tasks, undertaken by a desktop-based interfacing system, such as electronic control, pulser and receiver, and data processing, can be achieved by a flexible printed circuit board. With the advent of lower-power integrated circuits and flexible lithium-polymer battery technologies, we envision the entire hardware to be fully portable while maintaining its high performance.

Methods

Fabrication of the stretchable ultrasonic array

The fabrication of the stretchable ultrasonic array begins with preparing the multi-layered activation electrodes. To individually control each element of the array, 256 activation electrodes and 1 common ground are needed. It would be very challenging to place so many electrodes in a single layer while keeping the device layout compact and stretchable. We choose to integrate the electrodes in a multi-layered manner[79]. We use AutoCAD software to design the six layers of the activation electrodes to individually address each element (Supplementary Fig. 16), which minimizes the footprint of the entire device to a size much smaller than the stretchable ultrasonic device in our previous work[80]. The pitch of the array is shrunk from the previous 2 mm by 2 mm to the present 0.8 mm by 0.8 mm, and the kerf also has been decreased from the previous 0.8 mm to the present 0.2 mm, which enhances the active component density from the previous 39.06% to the present 58.05%. To route all elements to the same plane, vertical interconnect accesses based on laser ablation are adopted[79].

For each single element, we use 1–3 composite as the active material given its superior electromechanical coupling properties, appropriate acoustic impedance[81], and suppressed crosstalk between adjacent elements[35]. We choose silver-epoxy composites as the backing material. To make the backing layer more condensed and reduce the overall device thickness (~0.8 mm), uncured silver-epoxy mixture is centrifuged for 10 min at 3,000 r.p.m, which separates the extra liquid hardener, removes air bubbles in the silver-epoxy and improves the acoustic damping effect and the axial resolution.

The array with such a small footprint and large scale requires optimized fabrication techniques. We develop a new method of automatic alignment of the transducer elements to the bonding electrodes. We first bond a large piece of the backing layer to the 1–3 composite and then dice the bonded bilayer to the designed array configuration. A strong adhesion tape is used to fix the bilayer without delamination during dicing by the dicing saw (DAD3220, DISCO). The 2D array with designed element size and pitch is automatically formed. To prevent the array from tilting or moving when the array is bonded to the electrodes, a silicone elastomer (Ecoflex-0030, Smooth-On) is filled in the kerf and connects individual elements together.

Then conductive epoxy (Von Roll 3022 E-Solder) is used to bond the copper-based stretchable interconnects with the 1–3 composite. The device is put at room temperature for 8 h and at 40 °C for 2 h for tight bonding. High-temperature bonding in previous studies[35,36] generates serious damages to piezoelectric materials. First, dipoles in the piezoelectric materials are lost under high temperatures, which seriously damages its ability to transmit and receive ultrasonic waves, causing low signal-to-noise ratios of measurements. Although the dipoles can be re-aligned after applying an external electric field, the polarization is very time consuming. Additionally, an excessive electrical field will break down the piezoelectric element[36]. Second, high-temperature bonding will cause thermal damage to the epoxy in 1–3 composites. It softens and irreversibly deforms the epoxy so that the alignment of piezoelectric pillars in 1–3 composites is reduced. As a result, their electromechanical coupling performance decays. The low-temperature bonding method in this study avoids thermal damage of the epoxy and any possible depolarization of the piezoelectric materials in the 1–3 composite, which maximizes the piezoelectric performance of the elements. Before bonding the other electrode to the transducer array, the interface between the transducer array and the dicing tape is exposed to UV light (254 nm wavelength, PSD series Digital UV Ozone System, Novascan) for 10 min for surface de-adhesion. Then the array can be delaminated from the tape and bond with the other electrode using the same method.

Preparation and mechanical characterization of phantoms

The tissue-mimic phantoms are made by gelatin (Type A, Fisher Chemical) and silicon dioxide particles (325 mesh, Amazon) with different concentrations. We control the Young's moduli of the phantoms by tuning the concentration of gelatin in water. Concentrations of gelatin including 5%, 7%, 8%, 9%, 10%, 12%, 13% and 14% are selected, and the corresponding Young's moduli are 10.24 kPa, 21.82 kPa, 30.41 kPa, 39.66 kPa, 49.12 kPa, 64.27 kPa, 81.25 kPa and 99.89 kPa, respectively.

As shown in Supplementary Fig. 27, gelatin is added into boiling de-ionized water. 1-Propanol (Sigma-Aldrich) is dropped into the solution (9.2 g per 100 g de-ionized water) to facilitate the crosslinking of gelatin. Silicon dioxide particles (3% mass fraction of all ingredients) are added into the solution after the solution becomes clear. The particles serve as the markers for displacement tracking. After thorough mixing for 10 min, the suspension is poured into specific molds for cooling. When we make the bilayer phantoms for measurements of CNR_e and those in Fig. 3a, the bottom layer is cured into a cuboid geometry first and then the suspension of the second layer is poured and cured on the cuboid. Before pouring, the solution needs to be cooled to ~40 °C to prevent melting and osmosis of the bottom phantom by the hot solution[82].

The process of making the cyst and inclusion phantoms is different from making the bilayer phantom. To build a cylindrical cavity in the matrix, a tube with a 9.2 mm outer diameter is inserted into the uncured matrix solution. The tube is then removed after the matrix is cured. Solution or water is filled into the cavity to form the inclusion or cyst.

To calibrate the phantom modulus, eight pieces of homogeneous phantoms, including all concentrations of gelatin, are made. Compressive measurements are performed to characterize the Young's modulus of each component (Instron 5965). The testing rate is 0.05 min^{-1}, and the total compressive strain is ~2%. In this region, the phantoms obey the linear stress–strain behaviour and the Young's moduli are the slopes of the stress–strain curves (Supplementary Fig. 29).

Characterization of the device

We measure the frequency-dependent electrical impedance and phase angle curves following the conventional methods to characterize the electromechanical coupling performance of the ultrasound transducers (Fig. 1b). A network analyser (Hewlett-Packard 4195A) is used to do the testing with a frequency range of 1 MHz to 5 MHz. The effective electromechanical coupling coefficient K_{eff} evaluates the electromechanical conversion efficiency of the transducer, which can be derived on the basis of the resonant (f_r) and anti-resonant (f_a) frequencies of the transducers[39]:

$$K_{\text{eff}} = \sqrt{1 - \frac{f_r^2}{f_a^2}} \tag{1}$$

Crosstalk is characterized by calculating the ratio between the measured and reference voltages. A peak-to-peak voltage of 5 V under a sinusoid burst mode is applied by a function generator (Keithley 3390) to excite the element. The reference voltage signal received by neighbouring elements is collected with a frequency increment step of 0.2 MHz. The voltage ratio is transformed to the logarithmic scale.

Insertion loss is used to reflect the sonographic sensitivity of the transducer, and these two variables are inversely proportional. The measurement is done in water using a functional generator with an output impedance of 50 Ω and an oscilloscope (Rigol DS1104) in a 1 MΩ coupling mode. A tone burst of a sine wave from 1.5 MHz to 4.5 MHz is generated to excite the element, and the ultrasound echoes reflected from a quartz crystal are captured by the same element. After compensating the 1.9 dB energy loss of transmitting into the quartz crystal and 2.2×10^{-4} dB mm^{-1} MHz^{-2} loss due to the attenuation in water[83], the insertion loss can be calculated by

$$\text{Insertion loss} = \left| 20 \log \frac{V_r}{V_t} + 1.9 + 2.2 \times 10^{-4} \times 2d \times f_r^2 \right| \tag{2}$$

where V_r and V_t are the receiving and transmitting voltages, respectively, d is the distance between the transducer and the quartz crystal, and f_r is the resonant frequency[83]. The matching circuit substantially improves the received signal amplitude, yielding a high sonographic sensitivity of the transducer (Fig. 1d and Supplementary Fig. 20).

To characterize its waterproof performance, the device is put underwater for 2 weeks (Supplementary Fig. 21). Pulse-echo signals are collected every day to analyse the variation in the sonographic signal-to-noise ratio. During the measurements, the transmitting distance and the ultrasound incident angle are kept consistent all the time to ensure the accuracy of the testing results.

The time- and frequency-domain characterizations of pulse-echo response and bandwidth are shown in Supplementary Fig. 19b,c. An experimental setup, including a multi-channel control system (Verasonics 256) and an aluminium block, is used to obtain the raw data. We put the aluminium block into water and ultrasonic waves are transmitted and received by the same transducer element. After getting the radiofrequency signal, a fast Fourier transform is applied to convert the signals from the time domain to the frequency domain. The frequency bandwidth of the signals at −6 dB is determined by

$$\text{BW} = \frac{f_u - f_l}{f_c} \times 100\% \tag{3}$$

where f_u is the upper frequency, f_l is the lower frequency and f_c is the central frequency[84]. The signal-to-noise ratio of the transducer element can be calculated from Supplementary Fig. 19b, which is around 39 dB. Such a high signal-to-noise ratio is mainly attributed to the superior electromechanical coupling properties of the 1–3 composite, the low-temperature bonding technique and the electrical matching circuit. The bandwidth of the element is around 50% (Supplementary Fig. 19c), which still has room to improve. The relatively thin backing layer cannot completely dampen the excessive vibrations of the piezoelectric materials, leading to a long spatial pulse length. However, a thick backing layer will compromise the mechanical compliance of the device. Therefore, future improvements will focus on the development of new backing materials with high acoustic attenuation coefficients[85,86] while maintaining a small thickness of the backing layer.

The spatial resolution is characterized on the basis of the PSF of the transitional edges of an inclusion phantom[25]. The modulus distribution curves along the lateral and axial transition edges (that is, edges between the inclusion and matrix that are perpendicular and parallel to the ultrasound propagation direction, respectively) are extracted from the reconstructed 2D modulus mapping image (Supplementary Fig. 28). Then we apply the first derivative of the modulus distribution curves to derive the PSF, whose FWHM is defined as the spatial resolution.

Simulation of different imaging modes

The MATLAB software allows simulation of the three different ultrasound imaging modes: coherent plane-wave compounding, mono-focus and single plane wave. A model of 2 cm by 5 cm is built up for the simulations, where a bilayer structure with random points filling the entire region is set up. Here 1.5% and 0.5% of strain are added to the top and bottom layers with different moduli, respectively, and a new model with a compressed configuration is generated. Then, ultrasound waves are excited using the three transmission modes. Corresponding radiofrequency signals from pre- and post-compression are collected. The toolbox of MATLAB, Field II, is used to simulate the radiofrequency signals. These radiofrequency signals are beamformed to enhance the signal-to-noise ratio. Displacement fields are derived using the normalized cross-correlation algorithm. Finally, the spatial strain is mapped using the least-squares strain estimator (Supplementary Figs. 7 and 24).

System setup and data collection

Our imaging system is mainly composed of two parts: the front end and the back end. The stretchable ultrasonic array as the front-end device transmits and receives ultrasound waves. The back-end device is a commercial multi-channel controller (Verasonics Vantage 256 system) that can be programmed to generate an arbitrary waveform. Cables are used to connect both ends for power supplying and data transmission. The MATLAB software (MathWorks) is used to code to control the back-end hardware and drive the front-end stretchable patch, involving the processes of plane wave compounding excitation, echo signals collection and storage, and data processing. As shown in Supplementary Fig. 7, two receive buffers are designed by MATLAB to collect and store the radiofrequency signals. The first and second receive buffers are used to store the radiofrequency signals before and after compression, respectively. Then these stored radiofrequency data are retrieved and processed to form the displacement fields.

For the in vivo data collection, all human tests were approved under University of California, San Diego Institutional Review Board protocol 801085, which was obtained retrospectively due to the delays caused by coronavirus disease disruptions.

Phantom verifications by the commercial probe and ex vivo testing protocols

The commercial probe for verifying and reconstructing the 3D phantom images is a 64-element phased array transducer (P4-2v, Verasonics) with 2.8 MHz resonant frequency that is almost on a par with that of the stretchable ultrasonic array (f_r = 3 MHz). During the experiments, a 3D linear stage (Newport) is used to fix the commercial ultrasound probe, apply pressure to get 2D strain images and move to the next position. Each moving step is 0.8 mm, the same as the elevational pitch of the stretchable patch. Sixteen slices of the 2D images are post-processed to reconstruct the 3D images (Supplementary Figs. 34b and 36b). 3D rendering is accomplished with the Amira software (Visualization Sciences Group).

All ex vivo studies are approved by the Institutional Animal Care and Use Committee at the University of California, San Diego. A frozen food-grade porcine abdominal tissue is used for ex vivo testing by the stretchable ultrasonic array and MRE. The porcine abdominal tissue is selected because of the well-defined anatomy and modulus distributions[61]. When the device is in conformal contact with the tissue surface, ~0.5–1% strain is applied, which can be followed in real time by a customized graphical user interface. If needed, the large strain with high NCCs can potentially be achieved by combining successive steps of small strain[87]. Then, 16 slices of 2D displacement fields are collected sequentially under the compressive strain. The inverse elasticity problem model yields the modulus mapping images when the predicted displacement fields match the measured ones (Supplementary Fig. 41). More details of the inverse elasticity problem calculation are in Supplementary Note 10.

The MRE test (General Electric Discovery MR750 3.0T) is performed right after the ultrasound test. A hermetic bag is used to preserve the porcine abdominal tissue during travelling and testing to prevent any dehydration-induced changes in the modulus. A mechanical vibration paddle is tightly bonded to the sample tissue to generate shear waves in the tissue. Fifteen scanning slices with 0.9 mm × 0.9 mm spatial resolutions of each are obtained. The total measuring time is about 30 min. The shear modulus of each slice can be displayed in ImageJ software. Specifically, Young's modulus equals to three times of shear modulus in soft tissues[58]. The modulus ratios of all slices are then calculated to compare with the results from the stretchable ultrasonic arrays. The Amira software is applied to combine all slices (reconstructed in y and z directions) of ultrasound elastographic images and MRE results along the x direction to generate the 3D volumetric image. Cubic spline interpolation is used to compensate and smooth the image in the x direction.

The possible sacrifice of contrast due to the variation regularization and the 2D finite element model may have resulted in the slightly higher modulus contrast of MRE than ultrasound elastography. Besides, the 2D elasticity model used in solving the inverse elasticity problem may introduce unavoidable discrepancies when applied to cross-sections of anisotropic 3D samples[60]. Additionally, different imaging equipment manufacturers using proprietary data processing algorithms may also bring systematic deviations[88].

Reporting summary

Further information on research design is available in the Nature Portfolio Reporting Summary linked to this article.

Data availability

The main data supporting the results of this study are available within the paper and its Supplementary Information. The data generated in this study are available from figshare at https://doi.org/10.6084/m9.figshare.22197139.v1. Source data are provided with this paper.

References

1. Fung, Y.-C. & Skalak, R. Biomechanics. Mechanical properties of living tissues. *J. Appl. Mech.* **49**, 464 (1982).
2. Habibi, H. A. et al. In vivo assessment of placental elasticity in intrauterine growth restriction by shear-wave elastography. *Eur. J. Radiol.* **97**, 16–20 (2017).
3. Huh, J. H. et al. Obesity is more closely related with hepatic steatosis and fibrosis measured by transient elastography than metabolic health status. *Metabolism* **66**, 23–31 (2017).
4. Lee, G. Y. & Lim, C. T. Biomechanics approaches to studying human diseases. *Trends Biotechnol.* **25**, 111–118 (2007).
5. Mehrara, E., Forssell-Aronsson, E., Ahlman, H. & Bernhardt, P. Specific growth rate versus doubling time for quantitative characterization of tumor growth rate. *Cancer Res.* **67**, 3970–3975 (2007).
6. Wellman, P., Howe, R. D., Dalton, E. & Kern, K. A. *Breast Tissue Stiffness in Compression is Correlated to Histological Diagnosis* (Harvard BioRobotics, 1999).
7. Wang, Y. et al. Assessment of tumor stiffness with shear wave elastography in a human prostate cancer xenograft implantation model. *J. Ultrasound Med.* **36**, 955–963 (2017).
8. Furukawa, H., Iwata, R. & Moriyama, N. Growth rate of pancreatic adenocarcinoma: initial clinical experience. *Pancreas* **22**, 366–369 (2001).
9. Hasegawa, M. et al. Growth rate of small lung cancers detected on mass CT screening. *Br. J. Radiol.* **73**, 1252–1259 (2000).
10. Winer-Muram, H. T. et al. Volumetric growth rate of stage I lung cancer prior to treatment: serial CT scanning. *Radiology* **223**, 798–805 (2002).
11. Nakajima, T. et al. Simple tumor profile chart based on cell kinetic parameters and histologic grade is useful for estimating the natural growth rate of hepatocellular carcinoma. *Hum. Pathol.* **33**, 92–99 (2002).
12. Saito, Y. et al. Multiple regression analysis for assessing the growth of small hepatocellular carcinoma: the MIB-1 labeling index is the most effective parameter. *J. Gastroenterol.* **33**, 229–235 (1998).
13. Katyan, A., Mittal, M. K., Mani, C. & Mandal, A. K. Strain wave elastography in response assessment to neo-adjuvant chemotherapy in patients with locally advanced breast cancer. *Br. J. Radiol.* **92**, 20180515 (2019).
14. Botar-Jid, C. et al. The contribution of ultrasonography and sonoelastography in assessment of myositis. *Med. Ultrason.* **12**, 120–126 (2010).
15. Brandenburg, J. E. et al. Quantifying passive muscle stiffness in children with and without cerebral palsy using ultrasound shear wave elastography. *Dev. Med. Child Neurol.* **58**, 1288–1294 (2016).
16. Gao, J. et al. Quantitative ultrasound imaging to assess the biceps brachii muscle in chronic post-stroke spasticity: preliminary observation. *Ultrasound Med. Biol.* **44**, 1931–1940 (2018).
17. Illomei, G., Spinicci, G., Locci, E. & Marrosu, M. Muscle elastography: a new imaging technique for multiple sclerosis spasticity measurement. *Neurol. Sci.* **38**, 433–439 (2017).
18. Lv, F. et al. Muscle crush injury of extremity: quantitative elastography with supersonic shear imaging. *Ultrasound Med. Biol.* **38**, 795–802 (2012).
19. Lacourpaille, L. et al. Time-course effect of exercise-induced muscle damage on localized muscle mechanical properties assessed using elastography. *Acta Physiol.* **211**, 135–146 (2014).
20. Drakonaki, E. Ultrasound elastography for imaging tendons and muscles. *J. Ultrason.* **12**, 214 (2012).

21. Brandenburg, J. E. et al. Ultrasound elastography: the new frontier in direct measurement of muscle stiffness. *Arch. Phys. Med. Rehabil.* **95**, 2207–2219 (2014).
22. Gao, J., Du, L.-J., He, W., Li, S. & Cheng, L.-G. Ultrasound strain elastography in assessment of muscle stiffness in acute levodopa challenge test: a feasibility study. *Ultrasound Med. Biol.* **42**, 1084–1089 (2016).
23. Wen, H., Bennett, E., Epstein, N. & Plehn, J. Magnetic resonance imaging assessment of myocardial elastic modulus and viscosity using displacement imaging and phase-contrast velocity mapping. *Magn. Reason. Med.* **54**, 538–548 (2005).
24. Mercuri, M. Noninvasive imaging protocols to detect and monitor carotid atherosclerosis progression. *Am. J. Hypertens.* **7**, 23S–29S (1994).
25. Qian, X. et al. Multi-functional ultrasonic micro-elastography imaging system. *Sci. Rep.* **7**, 1230 (2017).
26. Montaldo, G., Tanter, M., Bercoff, J., Benech, N. & Fink, M. Coherent plane-wave compounding for very high frame rate ultrasonography and transient elastography. *IEEE Trans. Ultrason. Ferroelectr. Freq. Control* **56**, 489–506 (2009).
27. Francois Dord, J. et al. in *Ultrasound Elastography for Biomedical Applications and Medicine* (eds Nenadic, I. Z. et al.) 129–142 (Wiley, 2018).
28. Goenezen, S. et al. Linear and nonlinear elastic modulus imaging: an application to breast cancer diagnosis. *IEEE Trans. Med. Imaging* **31**, 1628–1637 (2012).
29. Pellot-Barakat, C., Frouin, F., Insana, M. F. & Herment, A. Ultrasound elastography based on multiscale estimations of regularized displacement fields. *IEEE Trans. Med. Imaging* **23**, 153–163 (2004).
30. Jiang, J. & Hall, T. J. A coupled subsample displacement estimation method for ultrasound-based strain elastography. *Phys. Med. Biol.* **60**, 8347 (2015).
31. Kallel, F. & Ophir, J. A least-squares strain estimator for elastography. *Ultrason. Imaging* **19**, 195–208 (1997).
32. Cloostermans, M. & Thijssen, J. A beam corrected estimation of the frequency dependent attenuation of biological tissues from backscattered ultrasound. *Ultrason. Imaging* **5**, 136–147 (1983).
33. Bader, K. B., Crowe, M. J., Raymond, J. L. & Holland, C. K. Effect of frequency-dependent attenuation on predicted histotripsy waveforms in tissue-mimicking phantoms. *Ultrasound Med. Biol.* **42**, 1701–1705 (2016).
34. Shung, K. K. *Diagnostic Ultrasound: Imaging and Blood Flow Measurements* (CRC Press, 2015).
35. Hu, H. et al. Stretchable ultrasonic transducer arrays for three-dimensional imaging on complex surfaces. *Sci. Adv.* **4**, eaar3979 (2018).
36. Wang, C. et al. Monitoring of the central blood pressure waveform via a conformal ultrasonic device. *Nat. Biomed. Eng.* **2**, 687–695 (2018).
37. Mi, X., Qin, L., Liao, Q. & Wang, L. Electromechanical coupling coefficient and acoustic impedance of 1–1–3 piezoelectric composites. *Ceram. Int.* **43**, 7374–7377 (2017).
38. Haller, M. & Khuri-Yakub, B. Micromachined 1–3 composites for ultrasonic air transducers. *Rev. Sci. Instrum.* **65**, 2095–2098 (1994).
39. Chen, R. et al. Eco-friendly highly sensitive transducers based on a new KNN-NTK-FM lead-free piezoelectric ceramic for high-frequency biomedical ultrasonic imaging applications. *IEEE Trans. Biomed. Eng.* **66**, 1580–1587 (2018).
40. Arumugam, V., Naresh, M. D. & Sanjeevi, R. Effect of strain-rate on the fracture-behavior of skin. *J. Biosci.* **19**, 307–313 (1994).
41. Wang, Y., Bayer, M., Jiang, J. & Hall, T. J. Large-strain 3-D in vivo breast ultrasound strain elastography using a multi-compression strategy and a whole-breast scanning system. *Ultrasound Med. Biol.* **45**, 3145–3159 (2019).
42. Céspedes, I. & Ophir, J. Reduction of image noise in elastography. *Ultrason. Imaging* **15**, 89–102 (1993).
43. Varghese, T. & Ophir, J. An analysis of elastographic contrast-to-noise ratio. *Ultrasound Med. Biol.* **24**, 915–924 (1998).
44. Kennedy, K. M. et al. Quantitative micro-elastography: imaging of tissue elasticity using compression optical coherence elastography. *Sci. Rep.* **5**, 15538 (2015).
45. Ding, H. et al. Ultrasonic imaging of muscle-like phantoms using bimorph pmuts toward wearable muscle disorder diagnostics. In *2018 IEEE Micro Electro Mechanical Systems (MEMS)* (eds Despont, M. & Ducrée, J.) 396–399 (IEEE, 2018).
46. Dietrich, C. F. et al. Strain elastography—how to do it? *Ultrasound Int. Open* **3**, E137 (2017).
47. Taylor, K. et al. Ultrasound elastography as an adjuvant to conventional ultrasound in the preoperative assessment of axillary lymph nodes in suspected breast cancer: a pilot study. *Clin. Radiol.* **66**, 1064–1071 (2011).
48. DeWall, R. J. Ultrasound elastography: principles, techniques, and clinical applications. *Crit. Rev. Biomed. Eng.* **41**, 1–19 (2013).
49. Krouskop, T. A., Wheeler, T. M., Kallel, F., Garra, B. S. & Hall, T. Elastic moduli of breast and prostate tissues under compression. *Ultrason. Imaging* **20**, 260–274 (1998).
50. Lopata, R. G. et al. Performance evaluation of methods for two-dimensional displacement and strain estimation using ultrasound radio frequency data. *Ultrasound Med. Biol.* **35**, 796–812 (2009).
51. Hÿtch, M., Snoeck, E. & Kilaas, R. Quantitative measurement of displacement and strain fields from HREM micrographs. *Ultramicroscopy* **74**, 131–146 (1998).
52. Papadacci, C., Bunting, E. A. & Konofagou, E. E. 3D quasi-static ultrasound elastography with plane wave in vivo. *IEEE Trans. Med. Imaging* **36**, 357–365 (2016).
53. Hayakawa, M., Hatano, T., Tsuji, A., Nakajima, F. & Ogawa, Y. Patients with renal cysts associated with renal cell carcinoma and the clinical implications of cyst puncture: a study of 223 cases. *Urology* **47**, 643–646 (1996).
54. Sigrist, R. M., Liau, J., El Kaffas, A., Chammas, M. C. & Willmann, J. K. Ultrasound elastography: review of techniques and clinical applications. *Theranostics* **7**, 1303 (2017).
55. Oberai, A. A., Gokhale, N. H. & Feijóo, G. R. Solution of inverse problems in elasticity imaging using the adjoint method. *Inverse Prob.* **19**, 297 (2003).
56. Ferreira, E. R., Oberai, A. A. & Barbone, P. E. Uniqueness of the elastography inverse problem for incompressible nonlinear planar hyperelasticity. *Inverse Prob.* **28**, 065008 (2012).
57. Song, D., Hugenberg, N. & Oberai, A. A. Three-dimensional traction microscopy with a fiber-based constitutive model. *Comput. Methods Appl. Mech. Eng.* **357**, 112579 (2019).
58. Yu, X. et al. Needle-shaped ultrathin piezoelectric microsystem for guided tissue targeting via mechanical sensing. *Nat. Biomed. Eng.* **2**, 165–172 (2018).
59. Risholm, P., Ross, J., Washko, G. R. & Wells, W. M. Probabilistic elastography: estimating lung elasticity. In *Biennial International Conference on Information Processing in Medical Imaging* (eds Székely, G. & Hahn, H. K.) 699–710 (Springer, 2011).
60. Gokhale, N. H., Barbone, P. E. & Oberai, A. A. Solution of the nonlinear elasticity imaging inverse problem: the compressible case. *Inverse Prob.* **24**, 045010 (2008).
61. Brouwer, I., Ustin, J., Bentley, L., Dhruv, A. & Tendick, F. in *Medicine Meets Virtual Reality* (eds Westwood, J. D. et al.) 69–74 (IOS Press, 2001).
62. Van Houten, E. E., Doyley, M. M., Kennedy, F. E., Weaver, J. B. & Paulsen, K. D. Initial in vivo experience with steady-state subzone-based MR elastography of the human breast. *J. Magn. Reson.* **17**, 72–85 (2003).

63. Xie, Y., Thomas, L., Hug, F., Johnston, V. & Coombes, B. K. Quantifying cervical and axioscapular muscle stiffness using shear wave elastography. *J. Electromyogr. Kinesiol.* **48**, 94–102 (2019).
64. Van Sligtenhorst, C., Cronin, D. S. & Brodland, G. W. High strain rate compressive properties of bovine muscle tissue determined using a split Hopkinson bar apparatus. *J. Biomech.* **39**, 1852–1858 (2006).
65. Ishiwatari, N., Fukuoka, M. & Sakai, N. Effect of protein denaturation degree on texture and water state of cooked meat. *J. Food Eng.* **117**, 361–369 (2013).
66. Cipryan, L. & Litschmannova, M. Intra-day and inter-day reliability of heart rate variability measurement. *J. Sports Sci.* **31**, 150–158 (2013).
67. Koo, T. K. & Li, M. Y. A guideline of selecting and reporting intraclass correlation coefficients for reliability research. *J. Chiropr. Med.* **15**, 155–163 (2016).
68. Sorbie, G. G. et al. Intra-session and inter-day reliability of the Myon 320 electromyography system during sub-maximal contractions. *Front. Physiol.* **9**, 309 (2018).
69. Pearcey, G. E. et al. Foam rolling for delayed-onset muscle soreness and recovery of dynamic performance measures. *J. Athl. Train.* **50**, 5–13 (2015).
70. Hotfiel, T. et al. Advances in delayed-onset muscle soreness (DOMS): part I: pathogenesis and diagnostics. *Sportverletz. Sportschaden* **32**, 243–250 (2018).
71. Kishimoto, K., Sakuraba, K., Kubota, A. & Fujita, S. The effect of concentric and eccentric exercise on muscle hardness. *Juntendo Med. J.* **64**, 371–378 (2018).
72. Niitsu, M., Michizaki, A., Endo, A., Takei, H. & Yanagisawa, O. Muscle hardness measurement by using ultrasound elastography: a feasibility study. *Acta Radiol.* **52**, 99–105 (2011).
73. Murayama, M., Nosaka, K., Inami, T., Shima, N. & Yoneda, T. Biceps brachii muscle hardness assessed by a push-in meter in comparison to ultrasound strain elastography. *Sci. Rep.* **10**, 20308 (2020).
74. Peake, J. M., Neubauer, O., Della Gatta, P. A. & Nosaka, K. Muscle damage and inflammation during recovery from exercise. *J. Appl. Physiol.* **122**, 559–570 (2017).
75. Nelson, N. Delayed onset muscle soreness: is massage effective? *J. Bodyw. Mov. Ther.* **17**, 475–482 (2013).
76. Lippold, O. The tremor in fatigue. *Ciba Found. Symp.* **82**, 234–248 (1981).
77. Lee, S.-Y. & Jo, M.-E. Comparison of maximum voluntary isometric contraction of the biceps on various posture and respiration conditions for normalization of electromyography data. *J. Phys. Ther. Sci.* **28**, 3007–3010 (2016).
78. Clarkson, P. M., Nosaka, K. & Braun, B. Muscle function after exercise-induced muscle damage and rapid adaptation. *Med. Sci. Sports Exerc.* **24**, 512–520 (1992).
79. Huang, Z. L. et al. Three-dimensional integrated stretchable electronics. *Nat. Electron.* **1**, 473–480 (2018).
80. Yang, Y. et al. Stretchable nanolayered thermoelectric energy harvester on complex and dynamic surfaces. *Nano Lett.* **20**, 4445–4453 (2020).
81. Kwok, K. W., Chan, H. & Choy, C. L. Lead zirconate titanate/poly (vinylidene fluoride-trifluoroethylene) 1–3 composites for ultrasonic transducer applications. *IEEE Trans. Ultrason. Ferroelectr. Freq. Control* **46**, 626–637 (1999).
82. Madsen, E. L., Hobson, M. A., Shi, H., Varghese, T. & Frank, G. R. Tissue-mimicking agar/gelatin materials for use in heterogeneous elastography phantoms. *Phys. Med. Biol.* **50**, 5597 (2005).
83. Li, X. et al. 80-MHz intravascular ultrasound transducer using PMN-PT free-standing film. *IEEE Trans. Ultrason. Ferroelectr. Freq. Control* **58**, 2281–2288 (2011).
84. Chen, Z. et al. High-frequency ultrasonic imaging with lead-free (Na, K)(Nb, Ta) O_3 single crystal. *Ultrason. Imaging* **39**, 348–356 (2017).
85. Webster, R., Button, T., Meggs, C., MacLennan, D. & Cochran, S. P3K-5 passive materials for high frequency ultrasound components. In *2007 IEEE Ultrasonics Symposium Proceedings* (ed. Passini Yuhas, M.) 1925–1928 (IEEE, 2007).
86. Sayers, C. & Tait, C. Ultrasonic properties of transducer backings. *Ultrasonics* **22**, 57–60 (1984).
87. Varghese, T. & Ophir, J. A theoretical framework for performance characterization of elastography: the strain filter. *IEEE Trans. Ultrason. Ferroelectr. Freq. Control* **44**, 164–172 (1997).
88. Tang, A., Cloutier, G., Szeverenyi, N. M. & Sirlin, C. B. Ultrasound elastography and MR elastography for assessing liver fibrosis: part 2, diagnostic performance, confounders, and future directions. *Am. J. Roentgenol.* **205**, 33–40 (2015).

Acknowledgements

We thank Z. Wu for the guidance on ultrasonic imaging algorithm and data processing, N. Szeverenyi for the help with MRE testing, S. Sinha for the discussions about eccentric exercise experiments, Y. Wang and R. Kou for the help with Young's modulus characterizations by a mechanical apparatus, and S. Xiang for the feedback on paper preparation. The material is based on research sponsored by Air Force Research Laboratory (AFRL) under agreement number FA8650-18-2-5402. The US Government is authorized to reproduce and distribute reprints for government purposes notwithstanding any copyright notation thereon. The views and conclusions contained herein are those of the authors and should not be interpreted as necessarily representing the official policies or endorsements, either expressed or implied, of Air Force Research Laboratory or the US Government. This work was partially supported by the National Institutes of Health (NIH) grants 1R21EB025521-01, 1R21EB027303-01A1, 3R21EB027303-02S1 and 1R01EB033464-01, and the Center for Wearable Sensors at the University of California, San Diego. The content is solely the responsibility of the authors and does not necessarily represent the official views of the NIH.

Author contributions

Ho.H., Y.M., X.G., D.S. and S.X. designed the research. Ho.H., Y.M., M.L. and Ha.H. performed the experiments. Y.M., X.G. and D.S. performed the data processing and simulations. Ho.H., Y.M. and X.G. analysed the data. Ho.H., D.S., X.G. and S.X. wrote the paper. All authors provided constructive and valuable feedback on the manuscript.

Competing interests

The authors declare no competing interests.

Additional information

Extended data is available for this paper at https://doi.org/10.1038/s41551-023-01038-w.

Supplementary information The online version contains supplementary material available at https://doi.org/10.1038/s41551-023-01038-w.

Correspondence and requests for materials should be addressed to Sheng Xu.

Peer review information *Nature Biomedical Engineering* thanks Antoine Nordez, Xiaoning Jiang and the other, anonymous, reviewer(s) for their contribution to the peer review of this work.

Reprints and permissions information is available at www.nature.com/reprints.

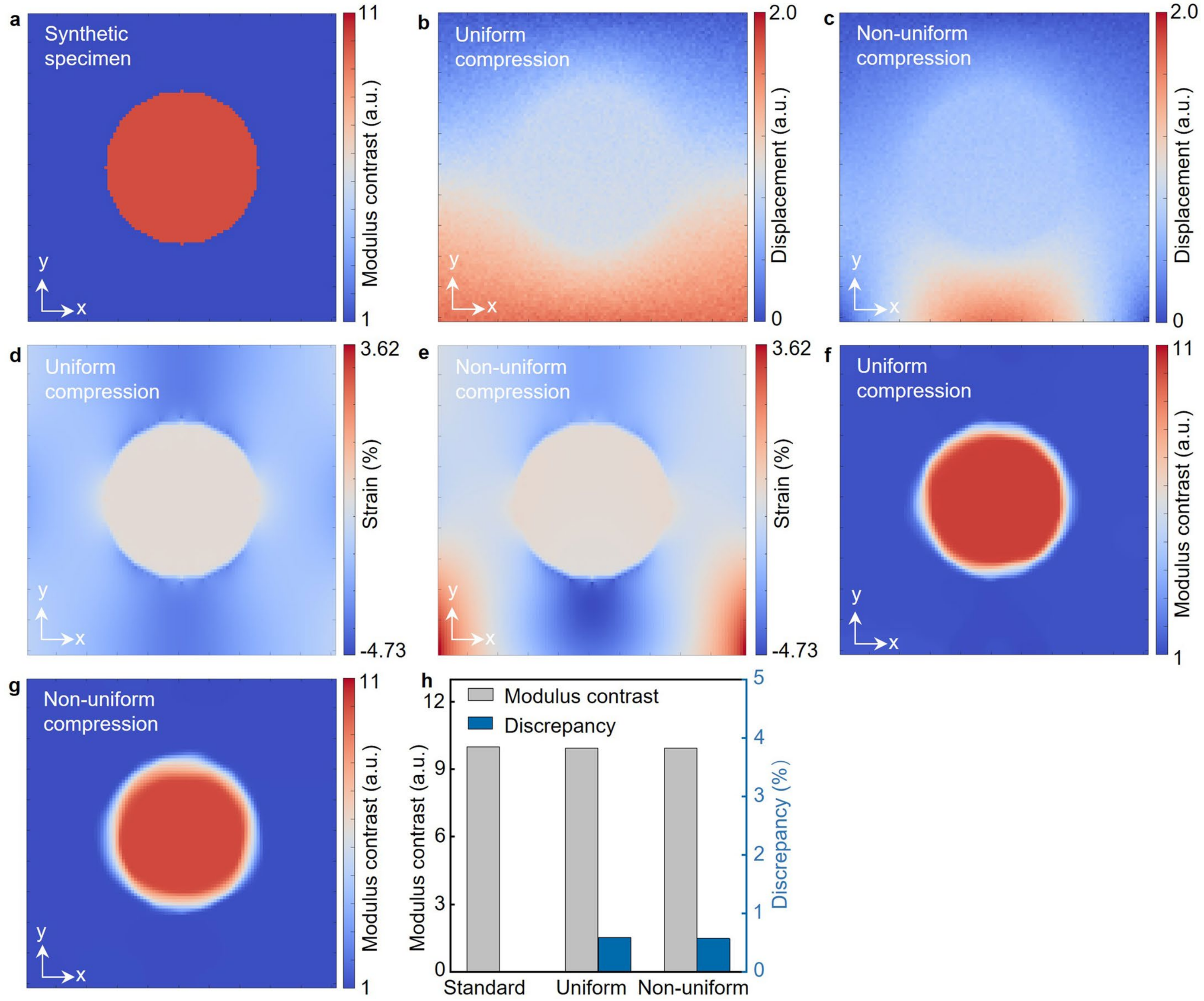

Extended Data Fig. 1 | Simulation results of uniform and nonuniform compressions. (**a**) A synthetic specimen with an inclusion that has a shear modulus 10 times higher than that of the surrounding matrix. The synthetic "measured" displacement fields based on (**b**) uniform compression and (**c**) non-uniform compression on the specimen. (**d**) and (**e**) show the strain distributions from uniform and non-uniform compression, respectively. The strain distributions vary upon different applied loads, which indicates that the strain-based elastography is qualitative only reflecting a relative stiffness of each component. The reconstructed modulus distributions obtained from solving inverse elasticity problems based on (**f**) uniform compression and (**g**) non-uniform compression. (**h**) Quantitative analysis of modulus contrasts and their deviations from the ground truth in (**a**).

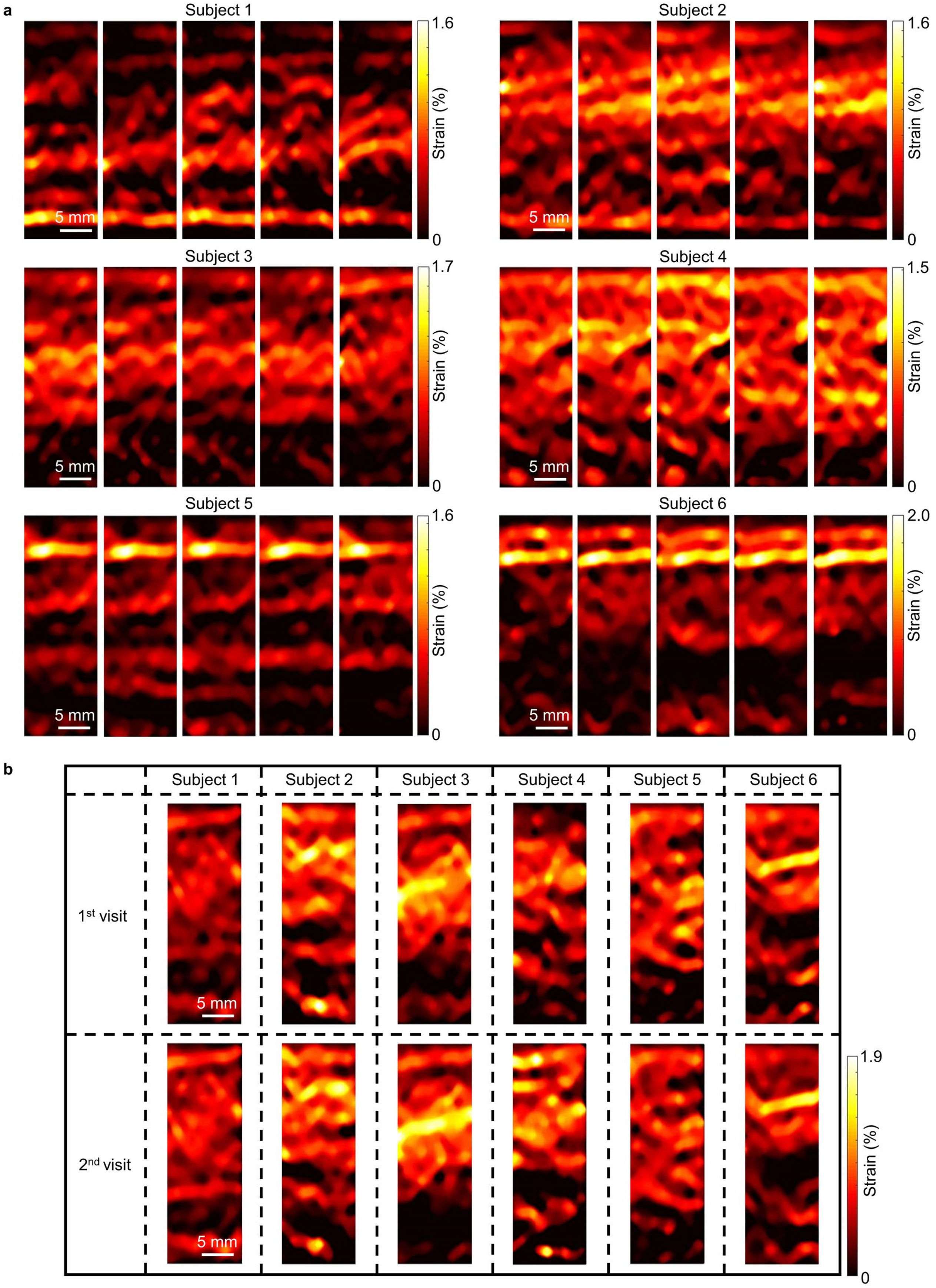

Extended Data Fig. 2 | Validating the device's reliability on six subjects. (**a**) Strain mapping results of upper arms of six subjects for the evaluation of the intra-session reliability. (**b**) Strain mapping results of upper arms of six subjects for the evaluation of the inter-day reliability.

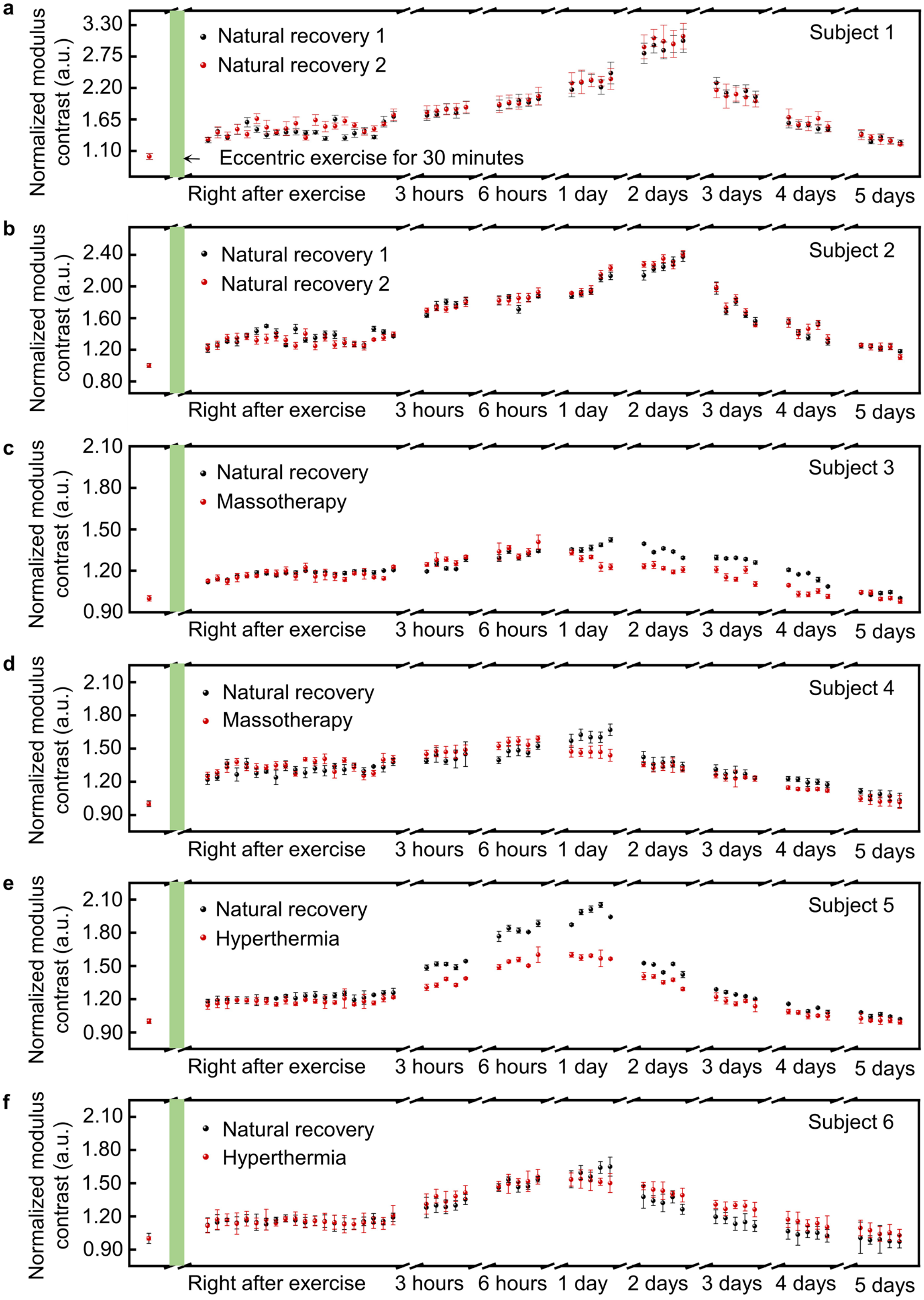

Extended Data Fig. 3 | Serial surveillance of delayed-onset muscle soreness in multiple subjects. Serial monitoring results of normalized modulus contrast of the biceps brachii muscle before and after the eccentric exercise. All six subjects did two rounds of experiments. In the first round, all subjects took the natural recovery after doing the exercise. In the second round, subjects in (**a**), (**b**) took natural recovery, subjects in (**c**), (**d**) took massotherapy, and subjects in (**e**), (**f**) took hyperthermia. For each test, we mapped the modulus distribution of the muscle. Then, we calculated the mean and standard deviations of the biceps brachii area. In each physiotherapy session, data are normalized by the modulus contrast of the biceps brachii muscle before exercise.

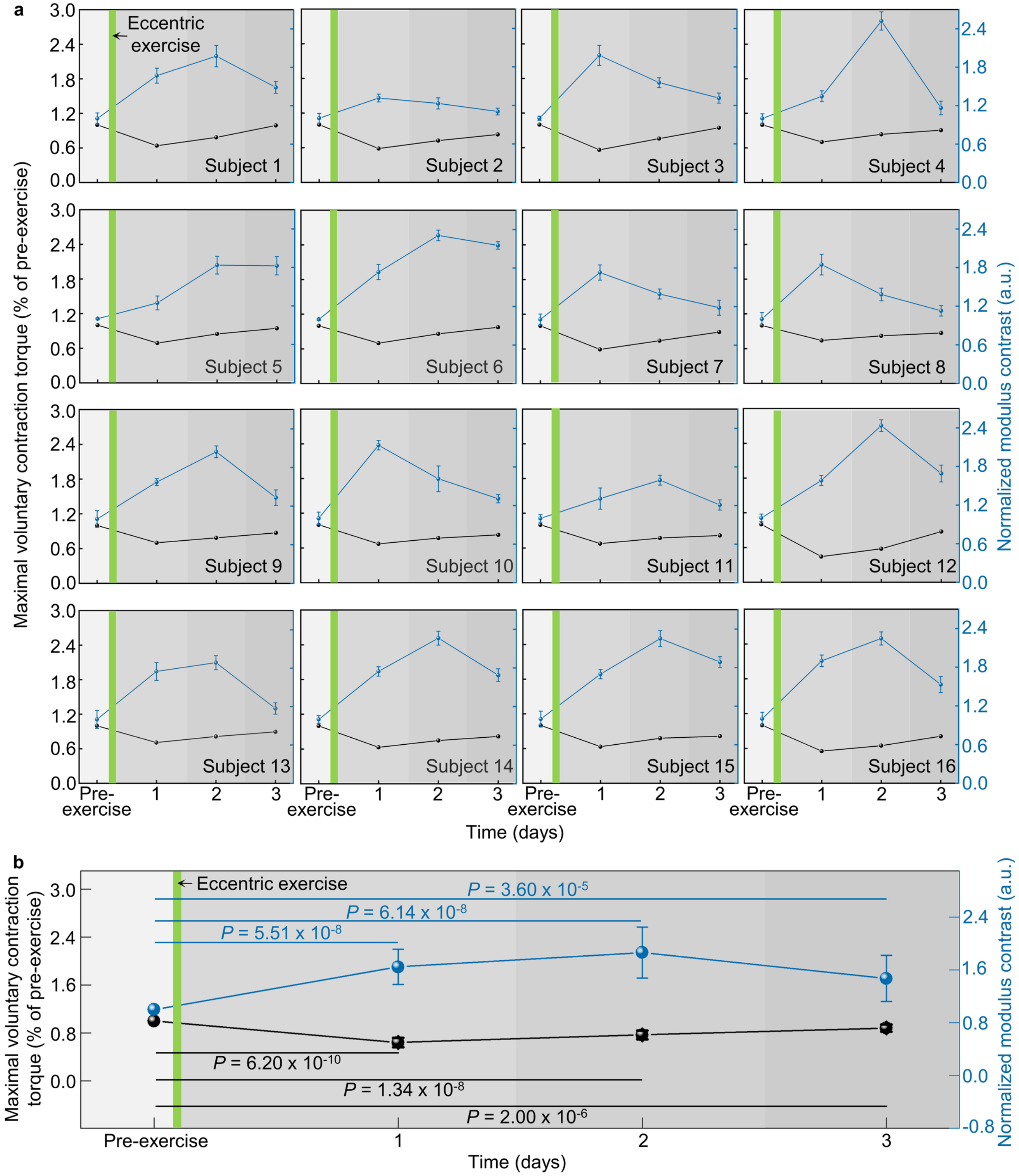

Extended Data Fig. 4 | Validation by a clinical standard method on a larger sample size. (**a**) Changes in the maximal voluntary contraction torque (black) and normalized modulus contrast (blue) of the biceps brachii muscle measured by the stretchable ultrasonic array before and after the eccentric exercise of 16 subjects. The points and error bars of the blue curves indicate the mean and standard deviation of modulus contrast of the biceps brachii muscle of every test. For each test, we mapped the modulus distribution of the muscle. Then, we calculated the mean and standard deviations of the biceps brachii area. In each physiotherapy session, data were normalized by the modulus contrast of the biceps brachii muscle before exercise. As a clinical standard approach, the maximal voluntary contraction can validate the muscle strength and muscle damage. (**b**) *P*-values of the clinical standard method and the stretchable ultrasonic array, which were calculated by single-sided paired t-test. Error bars are standard deviations of the data of 16 subjects ($n = 16$).

nature portfolio

Corresponding author(s): Sheng Xu

Last updated by author(s): Feb 27, 2023

Reporting Summary

Nature Portfolio wishes to improve the reproducibility of the work that we publish. This form provides structure for consistency and transparency in reporting. For further information on Nature Portfolio policies, see our Editorial Policies and the Editorial Policy Checklist.

Statistics

For all statistical analyses, confirm that the following items are present in the figure legend, table legend, main text, or Methods section.

n/a	Confirmed	
☐	☒	The exact sample size (*n*) for each experimental group/condition, given as a discrete number and unit of measurement
☐	☒	A statement on whether measurements were taken from distinct samples or whether the same sample was measured repeatedly
☐	☒	The statistical test(s) used AND whether they are one- or two-sided *Only common tests should be described solely by name; describe more complex techniques in the Methods section.*
☒	☐	A description of all covariates tested
☒	☐	A description of any assumptions or corrections, such as tests of normality and adjustment for multiple comparisons
☐	☒	A full description of the statistical parameters including central tendency (e.g. means) or other basic estimates (e.g. regression coefficient) AND variation (e.g. standard deviation) or associated estimates of uncertainty (e.g. confidence intervals)
☐	☒	For null hypothesis testing, the test statistic (e.g. *F*, *t*, *r*) with confidence intervals, effect sizes, degrees of freedom and *P* value noted *Give P values as exact values whenever suitable.*
☒	☐	For Bayesian analysis, information on the choice of priors and Markov chain Monte Carlo settings
☒	☐	For hierarchical and complex designs, identification of the appropriate level for tests and full reporting of outcomes
☒	☐	Estimates of effect sizes (e.g. Cohen's *d*, Pearson's *r*), indicating how they were calculated

Our web collection on statistics for biologists contains articles on many of the points above.

Software and code

Policy information about availability of computer code

Data collection	The data were collected via the commecial software Matlab R2019a.
Data analysis	The curves were analysed in the commercial software Matlab R2019a and Origin 2018. Magnetic resonance elastographic images were analysed by ImageJ 1.46r. 2D images were reconstructed on the basis of published algorithms for coherent plane-wave compounding, cross-correlation, least-squares strain estimation, and nonlinear adjoint coefficient estimation. 3D images were reconstructed by Amira 2019.1.

For manuscripts utilizing custom algorithms or software that are central to the research but not yet described in published literature, software must be made available to editors and reviewers. We strongly encourage code deposition in a community repository (e.g. GitHub). See the Nature Portfolio guidelines for submitting code & software for further information.

Data

Policy information about availability of data

All manuscripts must include a data availability statement. This statement should provide the following information, where applicable:

- Accession codes, unique identifiers, or web links for publicly available datasets
- A description of any restrictions on data availability
- For clinical datasets or third party data, please ensure that the statement adheres to our policy

The main data supporting the results of this study are available within the paper and its Supplementary Information. Source data for Figs. 1 and 2 are provided with this paper. The data generated in this study are available from figshare at https://doi.org/10.6084/m9.figshare.22197139.v1.

Human research participants

Policy information about studies involving human research participants and Sex and Gender in Research.

Reporting on sex and gender	We recruited 16 volunteers (14 males and 2 females). Gender was self-reported. Gender was not a factor considered in the experimental design, as the experiments were mainly about tissue-modulus testing, and gender is not a variable that affects the results of these experiments.
Population characteristics	Healthy subjects, 20–30 years old.
Recruitment	We posted recruitment flyers in the office building to recruit volunteers. Volunteers contacted us of their own accord. They were not selected from our own research group or from any group that had a partnership with us. The consent process was conducted by the research assistants of the project while the PI was not present. The volunteers were informed that participation was voluntary and could be withdrawn at any time without penalty. The PI affirmed that the volunteer's decision to participate or not did have no impact on their academic standing. Participants determined to join the research and who had contacted us via the email or phone number on the flyer were informed of the exercise protocol. We asked if they had experienced injury or soreness within 1 month and whether their health status allowed them to perform the exercise in this study. Only those subjects whose health status allowed them to complete the exercise were recruited. If they did not know their health status, they would inquire their personal doctors and then recontact us. We did not request the medical records of the subjects.
Ethics oversight	The institutional review boards at the University of California San Diego.

Note that full information on the approval of the study protocol must also be provided in the manuscript.

Field-specific reporting

Please select the one below that is the best fit for your research. If you are not sure, read the appropriate sections before making your selection.

☒ Life sciences ☐ Behavioural & social sciences ☐ Ecological, evolutionary & environmental sciences

For a reference copy of the document with all sections, see nature.com/documents/nr-reporting-summary-flat.pdf

Life sciences study design

All studies must disclose on these points even when the disclosure is negative.

Sample size	Sixteen consenting participants were recruited for the experiments. The participants were healthy and didn't have any soreness or injuries.
Data exclusions	No data were excluded.
Replication	Data acquisition was performed on participants multiple times to verify the functioning of the device.
Randomization	The participants were randomly recruited from outside the research group.
Blinding	No blinding measures were taken, and all data were processed together by multiple authors.

Reporting for specific materials, systems and methods

We require information from authors about some types of materials, experimental systems and methods used in many studies. Here, indicate whether each material, system or method listed is relevant to your study. If you are not sure if a list item applies to your research, read the appropriate section before selecting a response.

Materials & experimental systems

n/a	Involved in the study
☒	☐ Antibodies
☒	☐ Eukaryotic cell lines
☒	☐ Palaeontology and archaeology
☒	☐ Animals and other organisms
☒	☐ Clinical data
☒	☐ Dual use research of concern

Methods

n/a	Involved in the study
☒	☐ ChIP-seq
☒	☐ Flow cytometry
☒	☐ MRI-based neuroimaging

nature biomedical engineering

Article

https://doi.org/10.1038/s41551-023-01038-w

Stretchable ultrasonic arrays for the three-dimensional mapping of the modulus of deep tissue

Contents

Note S1. Significance of the stretchable ultrasonic array for serial monitoring 4

Note S2. Existing sensors and approaches for modulus testing 4

Note S3. Review of flexible/stretchable ultrasonic transducers and justification of the 2D array................ 6

Note S4. Discussions on qualitative and quantitative elastography 7

Note S5. Coupling conditions of traditional and stretchable ultrasonic devices on curved surfaces 7

Note S6. Characterization of the skin curvature on a breast phantom pre- and post-compression............. 8

Note S7. Displacement calculation by the normalized cross-correlation algorithm.................................... 9

Note S8. Strain calculation by a least-squares strain estimator algorithm 10

Note S9. Graphical user interface design.. 11

Note S10. Inverse elasticity problem formulation 11

Note S11. Determination of the adoptable range of curvatures of the stretchable array 14

Note S12. Elastographic and sonographic signal-to-noise ratios and contrast-to-noise ratios................. 17

Note S13. The transmission mode of coherent plane wave compounding 17

Note S14. Differences in strain distributions obtained by the stretchable and commercial probes 18

Note S15. The modulus contrast mapping of the cyst phantom 19

Note S16. Multi-site tissue mapping and protocols of the exercise and physiotherapy 19

Note S17. Mechanism of delayed onset muscle soreness.. 21

Note S18. Evaluation of repeated bout effect.. 22

Supplementary Figure 1. Significance of the stretchable ultrasonic array for serial tissue modulus monitoring. 24

Supplementary Figure 2. Comparison among all existing methods for tissue modulus mapping............. 25

Supplementary Figure 3. Common pitfalls in commercial ultrasonic shear-wave elastography operations.26

Supplementary Figure 4. Modulus imaging by a commercial ultrasonic shear-wave elastography machine.27

Supplementary Figure 5. Testing performance of the traditional rigid ultrasound probe and the stretchable ultrasonic array on curved surfaces.. 28

Supplementary Figure 6. Schematics of the exploded view of one element. All components have been labelled to illustrate the structure of an element... 30

Supplementary Figure 7. The workflow of reconstructing elastographic images by the stretchable ultrasonic array... 31

Supplementary Figure 8. Effects of the receive beamforming. 32

Supplementary Figure 9. Simulation of the change of transducers' locations by finite element analysis.. 34

Supplementary Figure 10. Characterizing the skin curvature of a breast phantom. 35

Supplementary Figure 11. Determination of the time-delay profile. 36

Supplementary Figure 12. Illustration of the normalized cross-correlation and least-squares strain estimator algorithms. 37

Supplementary Figure 13. The layout of the graphical user interface... 38

Supplementary Figure 14. Determination of the curvature range of the stretchable array. 39

Supplementary Figure 15. Transmission and receiving uniformity. 41

Supplementary Figure 16. Design and fabrication of the seven-layered electrodes................................ 42

Supplementary Figure 17. Optical images of the stretchable ultrasonic array bonded with anisotropic conductive films. 43

Supplementary Figure 18. Evaluation of the effective laser beam size and depth of focus....................... 44

Supplementary Figure 19. Electromechanical characterizations of transducer array. 45

Supplementary Figure 20. The setup for characterizing the transducers' sonographic sensitivity and the corresponding design of the electrical matching circuit.. 46

Supplementary Figure 21. Hydrophobicity characterization.. 47

Supplementary Figure 22. Optical images of the stretchable ultrasonic array under stretchability tests... 48

Supplementary Figure 23. Performance characterization of the transducers under deformation............. 49

Supplementary Figure 24. Comparison of three different transmission modes. 50

Supplementary Figure 25. Factors affecting the step size and the number of the compounding angle. ... 51

Supplementary Figure 26. Processing time for reconstructing images at different angle numbers........... 52

Supplementary Figure 27. Fabrication processes and optical images of tissue-mimic phantoms............ 53

Supplementary Figure 28. Characterizing the elastographic spatial resolutions. 54

Supplementary Figure 29. Stress-strain plots of tissue-mimic gelatin phantoms in quasi-static strain rate regimes. 55

Supplementary Figure 30. Modulus validation of a commercial breast phantom. 56

Supplementary Figure 31. Displacement and strain curves at the central lines of different phantoms. 57

Supplementary Figure 32. Schematic plots showing the mechanism of generating the displacement curve in the cyst phantom. 59

Supplementary Figure 33. 16 slices of 2D strain images of the inclusion phantom by the stretchable ultrasonic array. 60

Supplementary Figure 34. 3D strain images of an inclusion phantom by the stretchable and commercial ultrasonic probes. 61

Supplementary Figure 35. 16 slices of 2D strain images of the commercial breast phantom by the stretchable ultrasonic array. 62

Supplementary Figure 36. 3D strain images of the commercial breast phantom by the stretchable and commercial ultrasonic probes.. 63

Supplementary Figure 37. Repetitive tests. 64

Supplementary Figure 38. Flow chart of the process for calculating the forward and inverse elasticity problem. 65

Supplementary Figure 39. Simulated shadowing artifacts. 66

Supplementary Figure 40. The L-curve of calculating the inverse elasticity problem. 67

Supplementary Figure 41. Comparisons between the measured and predicted displacement fields of the porcine abdominal tissue.. 68

Supplementary Figure 42. Longitudinal studies of the strain curves of a commercial breast phantom..... 69

Supplementary Figure 43. Serial monitoring of the modulus evolution of a bovine gluteobiceps muscle. 71

Supplementary Figure 44. A schematic plot demonstrating the anatomical structures and locations for in vivo measurements. 72

Supplementary Figure 45. Comparing the coupling performance between ultrasonic gel and Silicone. ... 73

Supplementary Figure 46. The length of the muscle fiber before and after compression. 74

Supplementary Figure 47. Validating the device’s feasibility on 10 subjects. 75

Supplementary Figure 48. Soreness visual analog scale and testing protocol. 76

Supplementary Figure 49. A 3D elastographic reconstruction of the upper arm. 77

Supplementary Figure 50. The full view of the upper arm measured by a commercial ultrasonic system. 78

Supplementary Figure 51. Optical images of skin before and after monitoring. 79

Table S1. Reliability quantification in intra-session and inter-day testing. 80

Movie S1. Simulation illustrating the principle of ultrasound elastography. 81

Supplementary References 82

Note S1. Significance of the stretchable ultrasonic array for serial monitoring

From inflammation to cyst, fibrosis, and carcinoma, many pathological manifestations alter the mechanical properties, especially the elastic modulus, of the soft tissue, which can serve as biomarkers for clinical diagnosis[1]. Specifically, the increase in Young's modulus is typical in the development of both benign and malignant tumors in the human breast, primarily due to the proliferation of denser collagen fibers in the extracellular matrix[2]. Cysts filled with liquids exhibit much lower stiffness than the normal tissue[3]. Musculoskeletal and tendinous tissues associated with injury or inflammation, such as myositis and delayed onset muscle soreness, embody distinct differences in local stiffness[4-11]. Moreover, differentiation of Parkinson's disease from Parkinsonian syndrome requires strain ratio tests of biceps brachii muscles every minute, before and after drug administration[12]. The lack of frequent examination and long-term monitoring abilities prevents quick and effective tracking of tumor growth, cysts development, and diagnosis and rehabilitation processes of multiple musculoskeletal diseases and injuries. A stretchable ultrasonic array can meet this critical need that cannot be addressed by any existing approaches (Supplementary Fig. 1).

Note S2. Existing sensors and approaches for modulus testing

Conventional approaches for measuring tissue modulus can be divided into two main categories. The first are those relying on Hooke's law to derive elastic modulus through establishing the relationship between the displacement and the applied force, such as vacuum-based suction[13], compression[14], extension[15], and micro-/nano-indentation[16] (Supplementary Fig. 2). These methods are either limited to shallow regions beneath the skin[13-15,17] or lack of fine spatial resolution for anisotropic human tissues[13-15]. Currently, elastography can be done using 3 modalities, magnetic resonance imaging (MRI)[18], ultrasound[19], and optical coherence imaging[20]. Elastography itself is split into 2 types, static and dynamic methods. Static methods use strain elastography and can be imaged using ultrasound and optical coherence imaging.

Quasi-static elastography is an imaging modality that can assess the stiffnesses of tissues using ultrasound imaging or optical coherence tomography[21,22]. From the perspective of its working principle, it relies on applying tractions to generate and measure a small quasi-static deformation (strain) in the target tissue[19]. Two different sets of signals are acquired before and after deforming the target tissue and the displacement vectors between the two signals are estimated to map the strain distributions within the tissue[23]. From the perspective of how this measured deformation is used subsequently, quasi-static elastography includes strain-based elastography, which provides strain distributions to qualitatively reconstruct the stiffness within the tissue[23] using a least-squares strain estimator algorithm, and modulus-based elastography, which generates modulus distributions by solving the inverse elasticity problem to quantify the stiffness mapping results[24]. In the strain-based elastography approach, it is assumed that the stress in the tissue is uniform, and Hooke's Law ($\sigma = \varepsilon E$) is used to determine the Young's modulus as the reciprocal of axial strain. This approach can lead to artifacts in the resulting modulus map. When the stress distribution is not uniform this assumption is violated. In contrast to this, modulus-based elastography (the approach used in this manuscript) does not make the assumption of uniform stress. Instead, it involves solving an inverse problem to determine the spatial distribution of the modulus that is consistent with the measured displacement and the equations of equilibrium, which are valid under any stress distribution.

When compared with dynamic elastography, quasi-static elastography requires fewer external parts (i.e., no external oscillators required) and no high energy for the generation of acoustic radiation force, and is thus safe for long-term use[23]. The strain-based version of quasi-static elastography suffers from the drawback that its results depend on applied traction and are therefore subjective and operator-dependent. However, the modulus-based version eliminates this drawback and yields a spatial map of the modulus that is independent of the applied tractions and is equal to the true modulus distribution up to a multiplicative factor. In doing so, it comes closer to the absolute modulus obtained using dynamic elastography while retaining the advantages of quasi-static elastography. Finally, we note that when compared with dynamic elastography, ultrasound-based quasi-static elastography is much more viable in wearable devices. It makes wearable ultrasound transducers a platform technology for serial, non-invasive, and three-dimensional mapping of mechanical properties of deep tissues.

Dynamic methods, by contrast, are based on time-varying forces. Some dynamic methods can provide an absolute measure by quantifying the tissue modulus parameters. There are 2 main types of dynamic elastography techniques: shear wave elastography and vibro-acoustography[19].

Shear wave elastography generates shear waves within a tissue that travel perpendicularly to the excitation force, and relates their speed of propagation to the stiffness of the tissue, as shear waves travel faster within stiffer tissues. This can be imaged using ultrasound, MRI, or optical coherence imaging. The shear waves are generated using external vibrators, or in the case of ultrasound, acoustic radiation force impulse, in which high intensity ultrasound beams are focused on a single point to excite a shear wave[19]. Acoustic radiation force impulse has the advantage of not needing external vibrators due to its use of ultrasound transducers, but is very slow due to the singular focal point. Furthermore, it transfers a significant amount of energy into the tissue, and due to the long scan time, can cause significant heating of the tissue[19]. Thus neither form of shear wave elastography is suitable for wearable devices – external vibrators are too bulky, and the heat generation of acoustic radiation force impulse-based devices is not fit for long-term usage.

Shear wave elastography can also suffer from wave interference as the transmitted waves are reflected at the boundaries and interfere with the main signal. The main advantage of MRI over ultrasound shear wave elastography is the very wide field of coverage that can provide a more comprehensive diagnosis. However, MRI-based shear wave elastography is expensive, bulky, and slow compared to other methods of elastography. Besides, effective diagnostic ultrasound measurements based on shear-wave ultrasound elastography are highly operator-dependent (Supplementary Fig. 3). Results are prone to errors due to mishandling of the probe, such as moving the probe too quickly, offsetting scanning angle (by ~10 degrees), and pressing the probe too hard (~50 Newtons) against the human body. Professional technicians are required to properly position the probe perpendicular to the surface and scan slowly, being careful not to press on the target region excessively[25].

The robotic-assisted ultrasound procedure is an emerging technology by integrating the robotic arm with an ultrasound probe, which can achieve semi-automatic ultrasound scanning by an external machine instead of an operator. The robotic arm can control the scanning trajectory, area of interest, and holding forces, and is more stable than human operators, which is a promising candidate for long-term monitoring[26]. However, the robotic system is still far away from personalized healthcare because the overall system is already heavy and inaccessible to most healthcare providers. Moreover, the system has to be coupled with complicated cameras, algorithms, and a software interface to compensate for subject movement. Specifically, in an ideal case, the robotic-assisted ultrasound monitoring system has to be coupled with a complicated ultrasound image guiding program, which uses machine learning algorithms to evaluate the image quality and recognize human motions to adjust the robotic holding[27]. However, such an ideal long-term monitoring system has yet to be demonstrated.

In addition, the window for selecting the region of interest in the ultrasonic shear-wave elastography is very limited, which can only locate a small area of human tissue for elastographic measurements (Supplementary Fig. 4). This is because the energy of acoustic radiation force and thus shear wave generated by focused ultrasound is pretty low, leading to the limited propagation range and quick attenuation of the shear wave. Therefore, the test area is limited to only the region close to the focused ultrasound. It is not applicable for simultaneous surveillance of multiple tissues and muscles (e.g., biceps brachii and brachialis in the upper arm)[28].

Vibro-acoustography uses 2 different vibrational sources placed apart from each other, which vibrate at slightly different frequencies. The resulting interference of the two waves produces a radiation force at the focal point which oscillates at the difference of the two frequencies. The dynamic response of the tissue to this low-frequency excitation produces an acoustic emission that is detected by a hydrophone. The acoustic emission of the tissue is a function of its size, shape, stiffness, damping, and mass. The major advantages of this method are its high contrast and high spatial resolution. However, it has slow scan times and heats the tissue similarly to acoustic radiation force impulse due to the point-by-point scanning. In addition, the received signals reflect multiple different tissue properties at the same time, and the stiffness parameter cannot be fully isolated. Therefore, vibro-acoustography can also only qualitatively gauge the relative tissue stiffness[21,29].

Many portable ultrasound probes with miniaturized post-end for precision healthcare have been developed substantially in recent years. Those portable ultrasound probes are powerful and versatile to accomplish various tests outside the clinics. But no matter how portable/compact the existing ultrasound systems could be (such as Butterfly, Lumify, SonoQue, etc.), the necessity of being a long-term and continuous stable holding by the operator during usage prevents those systems from providing continuous monitoring.

Recent developments in wearable technologies are based on piezoresistance, piezoelectrics, or capacitors. Flexible piezoresistive microcantilevers allow mechanical measurements of diseased breast tissues. But the small testing depth (<4 μm) limits them for measuring only epithelial and stromal areas of the specimen[30]. Wearable piezoelectric systems achieve conformal contact with the human skin and rapid tests of mechanical properties of the tissue through the responses of the piezoelectric actuator–sensor pairs[31]. However, they are only suitable for the shallow tissue under the epidermis, lacking resolution in the depth dimension (Supplementary Fig. 2). Additionally, laminating on the dynamic surface of human skins may cause inaccurate results since the amplitude of the sensing voltage changes when the distance between actuators and sensors is varied. Compliant tactile sensors permit non-invasive detection of soft tissues and present their mechanical imaging, using capacitance-based pressure sensing array[32]. Although providing 2D qualitative mapping of internal strain distribution, they suffer from a similar limitation in detection depth (<5 mm). Besides, for lump-containing tissues, the embedded depth of the lumps influences the capacitance response, leading to a misdiagnosis of the lesion. Flexible needle-shaped microsystems based on piezoelectricity can be used to measure and distinguish the modulus of shallow tissues (<4.5 mm)[33]. This device for invasive biopsy mainly works in an in-patient environment, which is inappropriate for long-time serial monitoring in 3D spaces (Supplementary Fig. 2).

Note S3. Review of flexible/stretchable ultrasonic transducers and justification of the 2D array

Previously reported flexible ultrasonic transducers have been made of either intrinsically flexible piezoelectric polymers[11] or micromachined ultrasonic transducers[12]. Piezoelectric polymers have outstanding performance as ultrasound receivers due to their similar acoustic impedance to human tissues and broad bandwidth[13]. However, they are poor ultrasound transmitters due to their low piezoelectric coefficient (d_{33})[13], low dielectric constants[14], and high dielectric loss[13]. Micromachined transducers use the bending motion of a thin membrane to achieve their low device profile and flexibility[15] but sacrifice their electromechanical coupling properties in doing so[16]. There are two types of micromachined transducers: capacitive and piezoelectric. In the capacitive micromachined transducers[17,18], the membrane is caught between two opposing forces – an attractive electrostatic force pulling it towards the substrate and a mechanical restoring force opposing the deformation, which dampens the vibration amplitude significantly and reduces energy conversion efficiency. Piezoelectric micromachined transducers[19,20] have a bi-layer unimorph structure, with one layer providing actuation and the other providing passive mechanical support. The actuation layer is an active piezoelectric layer working in the d_{31} mode, while the passive layer creates strain asymmetry along the thickness direction. The device sensitivity of piezoelectric micromachined transducers is compromised by the passive layer[22], as it is unable to convert between mechanical and electrical energies like the actuation layer[21], but still consumes mechanical energies during the bending process.

As a result, while flexible ultrasonic arrays are a major step towards optimal acoustic coupling between the device and nonplanar surfaces, they sacrifice some of the transducer performance of traditional devices. Furthermore, they still lack one more critical aspect – stretchability. A flexible array can only conform to a developable surface (e.g., cylinders)[23-25], while the surface of the human body is nondevelopable (e.g., spheres). To conform to a nondevelopable surface, the device must possess stretchability in addition to flexibility. Thus, previously reported flexible ultrasonic transducers are still not fully compatible with the surfaces of the human body. To achieve stretchability, we integrate high-performance piezoelectric materials linked by an “island-bridge” structure where the piezoelectric “islands” are connected by serpentine-shaped metallic “bridges”. The array is then encapsulated by thin elastomers. The islands are locally stiff, but their connective serpentine bridges give the overall array stretchability and flexibility. Thus, we can preserve the advantages of traditional rigid transducers, while granting the device mechanical compliance. This approach offers >40% biaxial stretchability with little sacrifice to the performance of the transducers and allows the array to closely conform to the nondevelopable surface of the human body.

There are multiple reasons why we build a 2D array though still providing non-real time 3D imaging. First, the traditional and typical linear probe can hardly generate reliable 3D images. The only way to reconstruct a 3D image based on the linear probe is to slice the target into segments and slightly move the probe to acquire the data. However, this method can introduce a lot of errors: (1) The movement of the linear array along the elevational direction generates errors, because it’s challenging to control the interval distance, the compression force and angles to be the same every time; (2) Even with the help of a linear motor or robotic arm, the complicated process for equipment setup and the dozens of times for moving the probe are considerably time-consuming. A 2D array is absolutely preferred for 3D imaging, because there is no need to move around the 2D array on the surface of the target. Also, the applied strain to all slices is the same and we don’t have to worry about the related discrepancies. Besides, it takes less time to acquire the data for the image reconstruction than the linear probe.

Additionally, this work has paved the way for further work on real-time 3D reconstructions. The main reason that we currently are not able to achieve real-time results is the workload of data processing. There are roughly four steps for a single 3D image reconstruction: raw data acquisition, elastography computation for each slice, solving the inverse elasticity problem, and reconstruction from 2D to 3D. Even though the stretchable array is able to acquire data relatively fast with the Verasonic system, the rest of the processing still suffers from unavoidable long-time work. But we are sure the data processing can be further accelerated in the near future with technologies like parallel computing[34], graphics processing unit accelerating[35], or supercomputer[36]. Collectively, those advantages of the 2D array represent an important step in the progress of achieving real-time 3D imaging.

Note S4. Discussions on qualitative and quantitative elastography

Strain-based elastography is regarded as a qualitative method because it assumes that stress is uniform in the subject, so that strain is inversely proportional to modulus. Since the stress in heterogeneous samples is non-uniform, strain maps typically do not reflect accurate modulus distributions, offering only qualitative information about the relative stiffness of the subject. In other words, we can only know that one component is softer than another, rather than quantitative information about tissue stiffness. Additionally, because different external loads may cause different strain distributions inside the same subject, strain-based elastography is considered to be subjective and operator-dependent. As a result, this method can only show the morphology of the lesion and its relative stiffness to the surrounding tissues.

On the other hand, the modulus-based elastography is quantitative because it can reflect the objective biomechanical properties of tissues. There are two types of modulus-based elastography in existing studies. One type is shear-wave elastography, which can map the quantitative, absolute values of the shear modulus using detected shear wave velocity[19]. Another type combines the quasi-static elastography and an inverse elasticity problem, which can accurately provide the modulus ratio of each component[19]. Specifically, based on the displacement field of the tissue in response to quasi-static compressions, one can solve an inverse elasticity problem to determine modulus distributions, but only up to a multiplicative parameter. While this method does not provide the absolute values of the shear modulus, it generates quantitative, “normalized” values of the shear modulus that are objective and insensitive to external loadings. In this work, we used the second type, thereby performing quantitative, modulus-based elastography.

Note S5. Coupling conditions of traditional and stretchable ultrasonic devices on curved surfaces

Traditional rigid ultrasound probes have flat or convex bases, which cannot achieve solid interfacial contact and good coupling with irregular nonplanar surfaces, which are ubiquitous in the human body. Because of the geometric mismatch of the base of the probe and the curved surface of the subject, air gaps will inevitably appear at the interface between them (Supplementary Fig. 5). The large mismatch of acoustic impedance between air and human skin prevents the acoustic energy from transmitting into the deep tissues of the subject, causing artifacts and information loss.

There are two common ways to solve this problem. First, for those tissues that are compressible, clinicians usually press the probe to fit the curvature of the skin and achieve a good acoustic coupling situation. However, the pressing introduces pain in some cases and may also cause changes in the shape, position, and intrinsic properties of the target area, leading to test results of little diagnostic significance. A typical example is the stiffness measurement using ultrasonic shear-wave elastography, where improper operation caused by pressure can easily make the stiffness value abnormal (Supplementary Fig. 3) and then generate data of no use when evaluating the stages of tumors[37]. Second, tissues close to bones are hard to be compressed to accommodate the geometric mismatch. Therefore, clinicians always place a gel pad between the probe and the skin to enhance acoustic coupling. However, too much ultrasonic gel will serve as a high-pass filter, filtering out some weak but useful signals from tiny structures[38]. Additionally, the redundant gel will lead to significantly higher measurement results than the real modulus in the elastogram[39]. The development of stretchable ultrasonic probes completely solves this problem. The mechanical compliance of the device can accommodate all kinds of curvature without any mechanical damage and maintain robust and intimate contact with the human skin via Van der Waals, offering a stable interface for ultrasound waves transmission and receiving.

Although the stretchable device conforms tightly to the human skin, tiny air bubbles may still exist at the interface of the device and the skin. To achieve the best acoustic coupling condition, we added couplants underneath the device. However, traditional hydrophilic ultrasonic gels are volatile and cannot provide adequate acoustic coupling for the long-term monitoring of stretchable ultrasonic probes. Therefore, we selected a type of uncured silicone called Silbione as the couplant. Its acoustic impedance (1.03 MRayl)[40] is very close to the skin, and it does not volatilize at room temperature, which can provide a good acoustic coupling environment for a long time.

To investigate the coupling performance of the silicone couplant, we first made the most basic comparison experiment using a single transducer to sense a specific target under both traditional ultrasonic gel and silicone, and then compare the signal-to-noise ratio of the received signals. We did the experiments on a commercial phantom (CIRS Model 539) where there was a reflector 40 mm deep inside. The results in Figures S45a to c show a comparable signal-to-noise ratio with ultrasonic gels and silicone, indicating the good acoustic coupling performance of the silicone.

We then compared the imaging performance of the stretchable array on the human body (the upper arm) with ultrasonic gels and silicone. As Figures S45d and e show, the imaging results with clear anatomic structures and similar strain distributions reveal the comparable performance of those two couplants. Characterization of human tissues shows the practicability and excellent coupling conditions of silicone-based couplant for the stretchable ultrasonic array.

Note S6. Characterization of the skin curvature on a breast phantom pre- and post-compression

We take a commercial breast phantom as a typical example since its skin surface has a large curvature. Before mapping the modulus distribution of the breast phantom, the skin curvatures are characterized to determine the correct time-delay profile to be added to the array elements before and after compression. The skin surface of the breast phantom is scanned using a 3D scanner (HDI Advances, LMI Technologies, Vancouver, Canada), by which a digital model with 3D meshes is built to portray the surface morphology. This digital model is then imported into the Catia software (Dassault Systèmes, France) for curvature extraction. Forty-two data planes are drawn to intersect at the normal direction to the skin surface, producing forty-two intersection curves with 2 mm interval along the y direction (Supplementary Fig. 10b). The intersection interfaces are used to identify the maximum curvature of the surface. To obtain quantitative curvature distribution across the entire skin, the minimum curvature radii with 12 mm aperture among the forty-two intersection interfaces are calculated by applying circular curve-fitting[41]. The curve with the minimum curvature radius of 69 mm in this study has been selected to represent the maximum curvature of the skin (Supplementary Fig. 10d). The coordinates of the curve are extracted by the Catia software (the black curve in Supplementary Fig. 10f). To study the morphology of the skin after compression, the breast phantom model with relevant physical properties (e.g., density: 1000 kg/m^3, Young's modulus: 50 kPa, and Poisson's ratio: 0.5)[42] is established by the COMSOL Multiphysics software (COMSOL Inc, USA). 1% uniaxial strain along the z direction is exerted to the model. The coordinates of the curve after compression are extracted by the Catia software (the red curve in Supplementary Fig. 10f). The compression flattens the skin curvature to a certain degree.

Coordinates of the skin surface before and after compression are input into Field II for ultrasonic elastography simulations (Supplementary Fig. 11). The time-delay profiles of the array elements on the planar surface are applied to the array elements on the curvilinear surfaces, for both pre- and post-compression. Beamformed radiofrequency signals from these curvilinear surfaces are obtained (red curves in Supplementary Fig. 11a and b). To quantitatively evaluate the influence of the time-delay profiles, the beamformed radiofrequency signals from the planar surfaces are simulated (black curves in Supplementary Fig. 11a and b), which are then compared with the corresponding radiofrequency signals from the curvilinear surfaces (red curves in Supplementary Fig. 11a and b). The correlation coefficients are calculated (Supplementary Fig. 11c). The displacement field of the entire breast phantom model with the curvilinear surface is reconstructed and compared with that of the model with the planar surface. The difference in displacement distribution between the two fields is plotted to evaluate the image difference and quality (Supplementary Fig. 11d).

As illustrated in Supplementary Fig. 11a and b, most parts of the beamformed radiofrequency signals on planar and curvilinear surfaces overlap very well. The corresponding correlation coefficients are more than 0.9 for both pre- and post-compression. The major discrepancy in the near field (within 3.40 μs, corresponding to 2.62 mm depth in the soft tissue) is due to the relatively large difference in the transmission distances between the target area and the transducer elements on planar and curvilinear surfaces. The correlation coefficient of beamformed signals in the near field after compression is slightly higher than that before compression, because the compression flattens the skin curvature to a certain degree (Supplementary Fig. 10f). When the imaging area is in the far field, the difference in the transmission distances on planar and curvilinear surfaces becomes small.

The same phenomenon is also present in the displacement distribution (Supplementary Fig. 11d). The difference between two fields is very small across the entire image, with sporadic moderate values in the near field region. To further evaluate the difference quantitatively, the structural similarity index measure[43] and mean squared errors[44] are introduced to evaluate the similarity and average square difference between the two fields, respectively. The structural similarity index measure can be calculated by[45]:

$$\text{Structural similarity index measure} = \frac{(2\mu_x\mu_y+c_1)(2\sigma_{xy}+c_2)}{(\mu_x^2+\mu_y^2+c_1)(\sigma_x^2+\sigma_y^2+c_2)} \quad (1)$$

where μ_x, σ_x^2 are the average and the variation of the displacement field from the curvilinear surface, respectively. μ_y, σ_y^2 are the average and the variation of the displacement field from the planar surface, respectively. σ_{xy} is the covariance of these two fields. c_1 and c_2 are constants. The mean squared errors can be calculated by[45]:

$$\text{Mean squared errors} = \frac{1}{n}\sum_{i=1}^{n}(x_i - y_i)^2 \quad (2)$$

where the n is the number of the pixels, x_i and y_i are the values in both fields. The 0.9880 structural similarity index measure and 5.4×10^{-5} mean squared error demonstrate high correspondence of the two fields. This high correspondence is attributed to the 3 MHz resonant frequency with 500 μm wavelength of the transducer elements, which provides significant tolerance to the phase aberration induced by the geometry deformation and yields accurate displacement measurements.

Note S7. Displacement calculation by the normalized cross-correlation algorithm

Only uniaxial displacement along the compression direction is considered in this study. The normalized cross-correlation algorithm estimates the displacement based on the beamformed signals before and after compression, which are denoted as $p_a(n)$ and $p_b(n)$, $n = 1, 2, \ldots$, and N, respectively, where n is the index of sampling point, and N is the total length of the signal. To detect the detailed local displacement at different depths, a rectangular window slides from the beginning to the end of the signals to choose the signal interval. The normalized cross-correlation between the signals before and after compression is[46]:

$$R_{NCC}(m,l) = \frac{\sum_{n=m}^{m+W-1} p_a(n)p_b(n+l)}{\sqrt{\sum_{n=m}^{m+W-1} p_a^2(n)\cdot\sum_{n=m}^{m+W-1} p_b^2(n+l)}}, (l_{min} \leq l \leq l_{max}) \quad (3)$$

where m is the index of the sampling starting point of signal $p_a(n)$, l is the time shift between the signals before and after compression, l_{max} and l_{min} are the lower and upper boundaries of the time shift, and W is the window length. As shown in the equation, a period of signal $p_a(n)$ ($m \leq n \leq m+W-1$) before compression is selected. Another period of signal $p_b(n)$ ($m-l_{min} \leq n \leq m-l_{min}+W-1$) with the same length is then selected to calculate the similarity between the two periods. The values of l determine the possible range where the algorithm will search for the right time shift, which corresponds to the maximum $R_{NCC}(m, l)$. A strain filter (Fig. 2d) can screen the appropriate window length and step size when using the normalized cross-correlation algorithm to analyze the radiofrequency data[47,48]. By sliding m from 1 to N with a step size L, the displacement curve will be derived. For the displacement calculation, the window length W and the step size L are critical. A wider window will reduce the jitter error but result in lower spatial resolution. A smaller step size L can improve the spatial resolution but increase the computation time. Based on these considerations, we set the window length W and step size L to be 5 and 0.5 of the ultrasound wavelength, respectively (Supplementary Fig. 12).

Note S8. Strain calculation by a least-squares strain estimator algorithm

According to the strain-displacement equation, the strain can be calculated by:

$$\boldsymbol{\varepsilon} = \frac{1}{2}[\nabla \boldsymbol{u} + (\nabla \boldsymbol{u})^{\boldsymbol{T}}] \quad (4)$$

where $\boldsymbol{\varepsilon}$ is strain, and $\boldsymbol{u}$ is displacement. The right side of the equation is called the symmetric part of the displacement gradient[49]. However, the fluctuations in the displacement will be amplified in the strain images if this equation is directly used. Note that those fluctionations are unphysical, which are not from the shaking of human hand or the subject but rather from electromagnetic noise in the surrounding area that is involved when testing displacement. Therefore, the least-squares strain estimator algorithm is applied to calculate the strain because of the improvement of the signal-to-noise ratio compared to the simple gradient operation[50]. Assuming the displacement is $\boldsymbol{d}(i)$, where $1 \leq i \leq N$, a window with a length of N will slide from the beginning to the end to choose a period of displacement for computing the strain. The window length N is called the kernel size. The least-squares strain estimator algorithm will derive the precise linear fitting of the displacement curve within the window. For a period of displacement, it can be expressed as:

$$\boldsymbol{d}(n) = a \cdot z(n) + b, n = 1,2,\ldots,N \quad (5)$$

where z is the depth, and a and b are constants to be derived. The slope a is the strain to be obtained. The equation can be transformed to the matrix format:

$$\underline{\boldsymbol{d}} = A\begin{bmatrix} a \\ b \end{bmatrix} \quad (6)$$

A is an N×2 matrix, where the first column is the depth z, and the second column values are all one. The least-squares solution to this equation will be:

$$\begin{bmatrix} \hat{a} \\ \hat{b} \end{bmatrix} = [A^T A]^{-1} A^T \underline{\boldsymbol{d}} \quad (7)$$

where $\hat{a}$ and $\hat{b}$ are the estimated values of the least-squares strain estimator algorithm (Supplementary Fig. 12).

Note S9. Graphical user interface design

In the experiment, we used a palm to provide uniaxial compression to the device. To guide and quantify the external compression, we built up a graphical user interface that could display the current maximum strain in real-time (Supplementary Fig. 13). The graphical user interface consists of two parts: the left part that consists of three display windows, and the right part that is the control panel. The display window can show B-mode imaging, a displacement field, and a strain map in real-time. The maximum strain is shown on the top of the strain window, from which we can quantitatively control the external compression applied to the subject.

The Verasonics system provides the control panel with sufficient room for adjustment in the experiments. On the upper left of the control panel is the TGC (Time gain compensation) control center, where we may adjust the TGC in different segmentations on the image (by the eight bars above) or all together (by the TGC All Gain bar). TGC is a setting applied in diagnostic ultrasound imaging to account for sound-dampening of human tissues. It will increase the amount of gain given to an input signal as its sampling time increases monotonically. Above the TGC control center is the voltage control named 'High Voltage P1', which adjusts the exciting voltages of the ultrasonic array. On the lower left are two buttons of 'Rcv Data Loop', which controls receiving and storing of the radiofrequency signals from the transducers. The 'Simulate' button changes the mode from experiment to simulation, where effects of different probe designs can be foreseen. In the middle of the panel is the Processing area. The 'Acquire' bar determines how many frames we are going to store in the memory, and the 'Lock Rcv1' button can lock the first frame of radiofrequency signals before compression. The 'Freeze' button will pause the whole system without any data extraction. On the right are the 'Tools' dropdown and the 'Save'/'Load' buttons, which allow us to customize the filter parameters of the Verasonics system. Under 'Tools', we can select the filter parameters we want to edit, such as the center frequency and cutoff frequency, to generate the best raw radiofrequency data. We can then save and load these settings as presets using the 'Save' and 'Load' buttons. By default, the system applies a low-pass filter to remove noise.

We used B-mode imaging to find the target area and guide the compression without deviating from the imaging plane. Although the B-mode imaging quality is limited due to the small number of elements, big structures with strong reflections, such as interfaces between brachialis and humerus, can still be visualized. Those big structures are regarded as references for proper transducer location and compression guidance. Any deviations from the imaging plane will be seen as increased curvature of the interface between brachialis and humerus, suggesting the transducers have rotated during the compression and thus need to be corrected immediately.

Before compression, we click the "Lock Rcv1" in the graphical user interface to receive the initial radiofrequency signals. One frame of pre-compression radiofrequency signals will be temporally saved in the receive buffer 1. Then, we mildly compress the device, and 10 consecutive post-compression radiofrequency signals will be temporally saved in the receive buffer 2 and each of these signals is paired with the pre-compression radiofrequency signal to generate a series of strain images. According to Fig. 2d in the main text, the signal-to-noise ratio of the strain images becomes the highest at ~1% strain. Therefore, the displacement and strain mapping results with ~1% maximum strain will be selected for further modulus calculations.

Note S10. Inverse elasticity problem formulation

After measuring the displacement field in a sample in response to uniaxial compressions, we determine the shear modulus of the sample that generates-under the same loading conditions-a predicted displacement field that best matches the measured displacement field; this class of problems is often called inverse elasticity problems[51]. We formulate the inverse elasticity problem as a constrained optimization problem, with the objective of finding the shear modulus distribution that minimizes the objective function[24]:

$$\pi = \frac{1}{2}\int_{\Omega} |u_y - \tilde{u}_y|^2 d\Omega + \alpha\int_{\Omega} \sqrt{|\nabla\phi|^2 + \beta^2} d\Omega \ (8)$$

where the first term on the right represents the data mismatch between the measured and predicted displacement fields. More specifically, Ω is a chosen cross-section of the sample over which the shear modulus μ is computed, $\tilde{u}_y$ is the measured displacement field along the direction of compression, and u_y is the corresponding displacement field predicted by a computational model of the deformation of a sample with a shear modulus distribution μ. We utilize only the axial displacement because of the high noise level in the lateral and elevational displacements relative to the axial displacements.

The second term on the right side of the equation (8) denotes regularization that ameliorates the ill-posedness of the inverse elasticity problem[52]. In most cases, this term penalizes unphysical spatial oscillations of unknown fields, thus serving to ensure a certain smoothness of the solution to the inverse elasticity problem. In particular, we use a smoothened version of the total variation (TV) regularization[20,53-55], where ϕ=log(μ/μ_{ref}) with μ being the shear modulus and μ_{ref}=1 kPa being the reference shear modulus, and β is a small numerical parameter ($\beta \ll |\nabla\phi|$) that ensures the differentiability of the regularization term when $|\nabla\phi| = 0$. In this study, β is chosen to be 1×10^{-12}. In particular, it has been verified that $\beta \ll |\nabla\phi|$ in regions where ϕ varies significantly, and that the smoothened version of the TV term closely approximates the TV term. Further, α is the regularization parameter, which is noise dependent and must be chosen in such a way that the regularization term is balanced against the data mismatch term. If α is too small, one would tend to overfit measurement noise yielding a shear modulus distribution with unphysical oscillations. On the other hand, if α is too large, one would obtain an over-smoothed modulus distribution at the expense of significantly increasing the displacement mismatch. Thus, we select α using the standard L-curve approach[56]. Specifically, we solve the inverse elasticity problem for different α, and plot the data mismatch term against α on a log-log scale, with the goal of identifying the data point that lies at the bend of this curve (i.e., the point of the maximum curvature). The regularization parameter that corresponds to this point is thought to optimally balance the data mismatch term and the regularization term. Finally, we note that the TV regularization suppresses large oscillations of the shear modulus regardless of its steepness[20,53-55]. Since the shear modulus of a sample may vary significantly especially at the internal boundaries between different phases, the TV regularization is useful in preserving the sharp transition of the shear modulus.

The computational model of sample deformation can be described by a boundary-value problem:

$$\nabla \cdot \boldsymbol{\sigma} = 0 \ in \ \Omega \ (9)$$

$$u_y = \tilde{u}_y \ on \ \partial\Omega \ (10)$$

$$t_x = 0 \ on \ \partial\Omega \ (11)$$

Here the equation (9) represents the balance of linear momentum, where $\boldsymbol{\sigma}$ is the 2D Cauchy stress tensor given by a constitutive law that describes intrinsic sample properties (see below). On the other hand, equations (9) and (10) are the associated boundary conditions, where the axial displacements on the boundary, $\partial\Omega$, are prescribed to be equal to the corresponding measured axial displacements, while the lateral tractions t_x, on $\partial\Omega$, are set to zero, meaning that the sample is allowed to freely move in the lateral directions with no friction. Note that the traction vector $\mathbf{t} = \boldsymbol{\sigma n}$, where $\boldsymbol{n}$ is the unit outward normal vector of the boundary $\partial\Omega$.

The constitutive law of the sample is given by an incompressible, linear elasticity model under the assumption of plane stress[20,53,54,57], which is appropriate because all of the samples used in this study are unconstrained in the elevational direction and the resulting stress in this direction is expected to be small. In particular, the constitutive law can be written as:

$$\boldsymbol{\sigma} = 2\mu[tr(\boldsymbol{\varepsilon})\boldsymbol{I} + \boldsymbol{\varepsilon}] \ (12)$$

where $\boldsymbol{\varepsilon} = 1/2[\nabla\mathbf{u} + (\nabla\mathbf{u})^{\boldsymbol{T}}]$ (the equation (4)) is the 2D linear strain tensor (***T*** denotes the transpose of a given tensor), $tr(\boldsymbol{\varepsilon}) = \varepsilon_{xx} + \varepsilon_{yy}$ is the trace of the strain tensor, and ***I*** is the 2D second-order identity tensor ($I_{xx} = \mathrm{I}_{yy} = 1;\ I_{xy} = I_{yx} = 0$). Then, it can be seen that the Cauchy stress tensor $\boldsymbol{\sigma}$ depends on the displacement field $\mathbf{u}$ through $\boldsymbol{\varepsilon}$ in the equation (12). Thus, it is clear that equations (9) to (12) constitute a well-defined boundary-value problem for the displacement field $\mathbf{u}$ in the region Ω. That is, given an initial guess of the shear modulus μ, along with the constitutive law (the equation (12)) and boundary conditions (equations (10) and (11)), we can uniquely determine the displacement field $\mathbf{u}$ in Ω by solving the set of partial differential equation (the equation (9)).

The problem of minimizing π is reduced to a discrete optimization problem with nonlinear constraints once all of the field variables are represented using finite element basis functions, and the constraint equations are discretized using the finite element method[58]. Thus, the optimization variables are then the nodal values of ϕ=log(μ/μ_{ref}). The optimization problem is solved iteratively by means of a quasi-Newton method, L-BFGS-B[59], which requires-at each iteration-both the value of the objective function π and its gradient vector. This gradient vector is computed efficiently using the adjoint method[57]. The L-BFGS-B iterations are considered to be converged when the relative change in the displacement mismatch over the last five iterations is less than 1×10^{-8} (Supplementary Figs. 38 and 40). In summary, the steps to solve the inverse elasticity problems are as follows (Supplementary Fig 38):

1. For a given measured displacement field, and an initial guess of the shear modulus μ (and thus ϕ), solve the forward, boundary-value problem (equations (9) to (12)) to obtain a predicted displacement field.

2. Solve the adjoint problem driven by the mismatch between the predicted and measured displacement fields[57].

3. Evaluate the objective function π and its gradient with respect to ϕ, making use of the solutions of the forward and adjoint problems.

4. Use the objective function and its gradient to update ϕ.

5. Repeat steps 1-4 until convergence.

Finally, it is important to note that uniaxial compression is manually applied in this study, and our inverse formulation works for cases where applied loadings are non-uniform (e.g., different levels of compression or tension at different locations) as long as the resulting displacement field is accurately measured. This is essential because our inverse approach does not assume a uniform stress distribution; instead, it properly accounts for the balance of linear and angular momentums under arbitrary external loadings. In particular, by solving the inverse elasticity problem under the plane-stress assumption, the shear-modulus distribution of a given cross-section can be uniquely determined up to a multiplicative parameter[24,60]. In other words, the contrast between the shear moduli can be uniquely determined. Thus, if the measured displacement fields correspond to the response of the same material, the modulus contrast obtained by solving the inverse elasticity problem will always converge to the same solution, regardless of the external loading conditions. This feature is also consistent with the fact that the shear modulus (at small strains) is an intrinsic material property independent of loading conditions.

We used simulation to demonstrate that the shear modulus, obtained by solving the inverse elasticity problem, is practically independent of the applied loading conditions (e.g., uniformity of the applied compression). Briefly, we started from a “known” shear modulus distribution. We built a model with a specimen and determined the resulting displacement field in the specimen by solving the forward elasticity problem (see equations (9) to (12)). To make such a simulated displacement field close to real measurements, we added noise to it to generate the “measured” displacement field. Thereafter, we use these “measured” displacements to reconstruct the spatial distribution of strain by using the least-squares strain estimator algorithm and the shear modulus by solving the inverse problem (the flow chart of the process is in Supplementary Fig. 38). Finally, we compared these reconstructions with the “known” distributions to assess the performance of the approach. We performed the above procedures for (1) a uniform compression and (2) a non-uniform compression.

Extended Data Fig. 1a shows the shear modulus distribution of the synthetic sample, with a stiff inclusion embedded in a homogeneous and soft surrounding matrix. In particular, the matrix is a unit square and the inclusion is a circle with a radius that is a quarter of the edge length of the matrix. Moreover, the inclusion has a shear modulus of 10 and the background has a shear modulus of 1. Note that all these values are taken to be dimensionless because our calculations are insensitive to specific units (e.g., mm or cm, Pa or kPa). Such a sample mimics the one probed by the ultrasonic patch.

In the first case, we uniformly compressed the specimen in the vertical direction by applying to the bottom edge a uniform movement along the positive Y direction, while keeping the top edge fixed. Both the top and bottom edges are free to move in the X direction, and the two lateral edges are taken to be stress-free. The uniform, vertical movement applied to the bottom edge is assumed to be 0.02 units, corresponding to an overall compressive strain of 2% (such a small strain is ensured to be in the linear elastic regime). In the second case, we used the same setting as in the first case, except that we applied to the bottom edge a non-uniform, sinusoidal movement in the positive Y direction. This sinusoidal movement has an amplitude of 0.02 units and a wavelength of 2 units. For the exact displacement, u_{exact}, obtained by solving the forward elasticity problem, we added to it about 1% Gaussian noise to generate the “measured” displacement, u_{noise}, following reported methods[57,61]. Note that the noise level, e, can be derived using the L$_2$ norm and is given by

$$e = \frac{\|u_y - u_{noise}\|_2}{\|u_y\|_2} = 1\% \quad (13)$$

with $\|p\|_2 = \sqrt{\int_\Omega p^2 d\Omega}$ being the L$_2$ norm of a quantity p, and Ω being the specimen domain[57,61]. Having obtained the “measured” displacement field u_{noise}, we utilized the inverse algorithm to reconstruct the shear modulus for each loading case. Guided by the L-curve method described above, we chose the optimal regularization parameter to be $\alpha = 5\times10^{-4}$ for both cases.

As seen in Supplementary Extended Data Fig. 1b to h, the uniform and non-uniform compressions yield rather different displacement and strain distributions, which indicate that the strain-based elastography is a qualitative method only reflecting a relative stiffness of each component for a subject with inhomogeneous structures. On the contrary, the modulus distributions obtained by solving the inverse problem for the two cases are very similar. Concretely, the reconstructed inclusion moduli based on uniform and nonuniform compressions are the same: $\mu_{inclusion}$=10.2905. The reconstructed moduli of the surrounding matrix based on uniform and non-uniform compressions are $\mu_{matrix} = 1.0352$ and 1.0350, respectively. Furthermore, the modulus ratio between the inclusion and matrix under uniform and non-uniform compressions are 9.940 and 9.942, respectively, very close to each other. Most importantly, the differences between the reconstructed modulus ratios and the exact ratio (i.e., 10) are very small (<0.6%), demonstrating that the accuracy of the results is practically insensitive to non-uniform external loadings.

This technology cannot currently provide the absolute modulus value for each component, due to the unknown magnitude of the applied stress. This drawback can potentially be solved in future studies by integrating a calibration layer with known elastic properties with the stretchable ultrasonic array[20], or a force sensor on the back of the device.

Note S11. Determination of the adoptable range of curvatures of the stretchable array

A single pair of adjacent transducers within the array is examined and called x_1 and x_2 (Supplementary Fig. 14a and b). x_1 and x_2 are initially separated by a straight distance defined by the initial design pitch, $a = 0.8\ \mathrm{mm}$ in their initial planar state. When conformed to a curved surface, the straight distance between x_1 and x_2 changes to a shortened length, L, while a conforms to the curvature and becomes the arc length between x_1 and x_2. This arc has a radius of curvature, R, corresponding to the curvature of the surface being conformed to. Transducers x_1 and x_2 are separated by the arc angle, θ. L represents the conformed array pitch. Thus, we solve for L as follows:

First, we find the angle, θ, of the arc between transducers x_1 and x_2:

$$\frac{a}{R} = \theta \ (14)$$

Then, we can find the conformed array pitch, L, based on our surface's known radius of curvature:

$$L = \sqrt{2R^2 - 2R^2 \cos\frac{a}{R}} \ (15)$$

In this study, $a = 0.8$ mm. Thus L can be reduced to a function of R:

$$L(R) = \sqrt{2R^2 - 2R^2 \cos\frac{0.8 \text{ mm}}{R}} \ (16)$$

For the breast phantom used in this study, the curvature is 70 mm. Thus, at this curvature:

$$L(R = 70\ mm) = \sqrt{2(70^2) - 2(70^2) \cos\frac{0.8 \text{ mm}}{70 \text{ mm}}} = 0.7999956 \text{ mm} \ (17)$$

This is only a 0.00054% difference from the initial design pitch of 0.8 mm. Additionally, according to our simulations below, the stretchable array can conform to surfaces of curvature $\kappa \le \frac{1}{30}\ \text{mm}^{-1}$, or radii of curvature $R \ge 30\ mm$. At this maximum allowable curvature of $\kappa = \frac{1}{30}\ \text{mm}^{-1}$, we find:

$$L(R = 30\ mm) = \sqrt{2(30^2) - 2(30^2) \cos\frac{0.8 \text{ mm}}{30 \text{ mm}}} = 0.7999763 \text{ mm} \ (18)$$

This is still only a 0.0030% difference from the initial design pitch of 0.8 mm. Therefore, due to such a negligible difference in pitch generated within the allowed curvature range of our array, we consider it appropriate to use a constant 0.8 mm pitch for beamforming even when the array is conformed to a curved surface.

For the curvature range of the surfaces the stretchable array can be conformed to, there are two limiting factors. First is the mechanical limit of the copper serpentine interconnects. When the array is conformed to a curved surface, the serpentine interconnects are strained. This strain is positively correlated with the surface curvature, so there is a maximum curvature where the copper serpentines would reach their mechanical limits, i.e., the copper yield strength, beyond which plastic deformation takes place.

The second limitation is the ultrasonic strain imaging performance of the device. For this study, we used a planar beamforming algorithm. At small curvatures, this is a reasonable assumption that does not produce many errors, especially for deep tissues. At large curvatures, the transducers are no longer be in the same plane, which causes the delays that are used to align the ultrasound signals from each transducer to be erroneous in the algorithm. The amount of error increases with the surface curvature. Thus, there is a curvature limit where the errors produced in the displacement fields are no longer acceptable. For our study, we would like to retain an image structural similarity index of >95%, referenced against the image taken from a flat surface. We take this value because a structural similarity of 95% is the threshold where human observers are unable to tell whether or not an image has been distorted[62].

A single pair of adjacent transducer elements within the array is examined, connected by a copper serpentine electrode (Supplementary Fig. 14c). In the planar scenario, this unit is consistent with the initial design. Once strained, one end of the transducer's angles away from each other, while the other end angles toward each other, which creates strain and stress distributions along the serpentine. We would like to determine the curvature at which the maximum stress along the serpentine reaches the yield strength of copper.

The parameters used for this simulation are as follows:

Material	Parameter	Value
Copper	Young's Modulus	119 GPa[63]
	Poisson Ratio	0.34[63]
	Yield Strength	357 MPa[63]
1-3 composite	Young's Modulus	71 GPa[64]
	Poisson Ratio	0.31[65]

An ideal elastic-bilinear relationship was used for the copper behaviour. For each simulation in ANSYS, the two transducers and serpentine unit would begin in the planar configuration, and then be subjected to the deformation produced by a surface of a prescribed radius of curvature. The simulations began from a surface of 80 mm radius curvature and were repeated for various decreasing radii. The graphed data from the simulation trials are shown in Supplementary Fig. 14d. At a curvature of $\kappa = \frac{1}{6.6}\ \mathrm{mm}^{-1}$, the maximum stress along the copper serpentine reaches 355 MPa[63], which is effectively right below the yielding limit (Supplementary Fig. 14e).

A single row of 16 transducers in the array is examined. After conforming to the curved surface, the transducers are displaced out-of-plane, which causes the time delay used for aligning ultrasound signals from each transducer to be no longer accurate. The algorithm's perceived distances from the transducers to the scatterer are incorrect. Thus, we would like to determine the maximum curvature at which the strain image of the conformed array maintains >95% accuracy with respect to the planar reference image.

For this simulation, we used a similar methodology to that in Note S6. In quasi-static strain elastography, the displacement differences between a pre-compression and post-compression image are compared to map the strain distributions. Thus, we first simulate the phantom tissue compression, followed by the corresponding ultrasound displacement fields. A computer phantom was generated in COMSOL Multiphysics with identical properties to the commercial breast phantom used in this study. Its radius of curvature was decreased in steps until the resulting simulated strain image no longer maintained a >95% structural similarity index with respect to the planar reference image. In each simulation, a stiff square plate of 12 mm × 12 mm × 0.8 mm was used to exert a downwards compression of 1% uniaxial strain on the breast phantom. The simulation setup and results are shown in Supplementary Fig. 14f.

Following the compression simulation, we extracted the coordinates of the breast phantom's surface curvature from both before and after compression. The transducers' coordinates in each state were then derived from these surface curvatures, and input into Field II for ultrasonic elastography simulations. A similar process was performed on a phantom with a planar surface. The image taken by the conformed array is compared against that from the planar phantom to get a structural similarity index.

The final results of our simulation show that the strain images (Supplementary Fig. 14g) of a phantom with $\frac{1}{30}\mathrm{mm}^{-1}$ curvature result in a 95% structural similarity. Thus, the imaging performance constraint limits the curvatures to be below $\frac{1}{30}\mathrm{mm}^{-1}$, which is smaller than the curvature ($\frac{1}{6.6}\mathrm{mm}^{-1}$) allowed by the mechanical performance constraint. It is worthy noting that the errors in the conformed array imaging are confined almost entirely to the near field, <5 mm below the tissue surface, and are almost absent in the far field. The difference in signal travel time imposed by the curvature (as compared to a planar surface) makes up a significant error percentage in shallow tissues, where the signal travel time is very short, while the long signal travel time in deep tissues makes the error percentage very small. Thus, despite using a planar algorithm, the device can maintain near-perfect image accuracy in deep tissues. The errors in the near field can be further reduced by using lower transducer frequencies, which allows more tolerations for curvature-induced dislocations of the elements[66].

Based on the simulations and analyses of the mechanical limited and imaging performance limited curvature of the ultrasonic array, we determine that this device is limited to curvatures of $\kappa \leq \frac{1}{30}\mathrm{mm}^{-1}$, imposed by the imaging performance limitation.

Note S12. Elastographic and sonographic signal-to-noise ratios and contrast-to-noise ratios

The quality of the resulting elastogram is typically quantified by the elastographic signal-to-noise ratio ($\mathrm{SNR_e}$) and the elastographic contrast-to-noise ratio ($\mathrm{CNR_e}$) (Fig. 2a to f). $\mathrm{SNR_e}$ reflects the ratio between the mean intensity and the variance of the strain image. The formula for calculating $\mathrm{SNR_e}$ is:

$$SNR_e = \frac{s}{\sigma} \quad (19)$$

where s is the mean of the strain and σ is the standard deviation. There are some differences and relationships between the sonographic signal-to-noise ratio and $\mathrm{SNR_e}$. The sonographic signal-to-noise ratio is the signal and noise ratio of radiofrequency signals, which is only attributed to the performance of the ultrasonic probe, i.e., the hardware. Piezoelectric materials with high electromechanical coupling coefficient and good fabrication technologies improve the sonographic signal-to-noise ratio of the radiofrequency data. On the other side, excellent $\mathrm{SNR_e}$ depends not only on the good hardware performance, but also on the transmitting mode and the imaging algorithms involved.

The sonographic contrast-to-noise ratio reflects the echo intensity difference of two regions. Unlike the sonographic contrast-to-noise ratio, $\mathrm{CNR_e}$ reflects the ratio between strain contrast and standard deviation, which is defined as:

$$CNR_e = 20log_{10}\left(\frac{2(S_{in}-S_{out})^2}{\sigma_{in}^2+\sigma_{out}^2}\right) \quad (20)$$

where S_{in} and σ_{in} are the mean and standard deviation strain values inside the target region, respectively; S_{out}, and σ_{out} are the mean and standard deviation strain values outside the target region, respectively[67].

The values of $\mathrm{SNR_e}$ and $\mathrm{CNR_e}$ are attributed to the combined contributions of transducer performance, the imaging method, and the post data processing algorithms[68]. The function of fitting the $\mathrm{CNR_e}$ versus modulus contrast is[69]:

$$f(x) = 14.77\log_{10}(x-1) + 7.156 \quad (21)$$

With the coefficient of determination of >0.98, the measured data highly match the fitting function, indicating the reliability of the experimental results.

Note S13. The transmission mode of coherent plane wave compounding

One row of the linear array is composed of M transducer elements with the pitch of x_{pitch}. Thus, the position of i^{th} element is defined as $(x_i, 0)$, where x_i equals $x_{\mathrm{pitch}} \cdot (i-1)$. The detection region will be a rectangle below the array. By applying different time delays to each element, the array will emit K plane waves towards different directions with an angular interval of 1°. Each element starts to receive the echoes immediately after the transmission (Fig. 2b inset). Assuming the angle between the plane wave and the linear array is α_k, $k = 1, 2, \ldots,$ and K, the wave propagation time from the beginning of the transmission to the element pixel (x, z) will be[70]:

$$t_{i,k}^{e} = (z cos\alpha_k + x sin\alpha_k)/c \quad (22)$$

This transmission time delay is constant for all elements. The reflection time delay from the pixel (*x*, *z*) to the *i*-th element can be estimated as:

$$t_{i,k}^{r} = \sqrt{z^2 + (x - x_i^t)^2}/c \quad (23)$$

The total time delay will be:

$$t_{i,k}^{delay} = t_{i,k}^{e} + t_{i,k}^{r} \quad (24)$$

which determines the round-trip time of ultrasound waves from the emission to the moment received by the element *i*. The measured ultrasound signal by the *i*-th channel can be expressed as $s_i(t)$, $i = 1, 2, \ldots$, and M. Therefore, by applying the Delay-and-Sum algorithm, the reconstructed signal at pixel (*x*, *z*) corresponding to angle α_k will be:

$$p_{\alpha_k}(x, z) = \sum_{i=1}^{M} s_i(t - t_{i,k}^{delay}) \quad (25)$$

Without applying any envelope calculation or other post-processing, all of the images of different angles are added coherently, yielding the final beamformed signal (Supplementary Fig. 8):

$$p(x, z) = \sum_{k=1}^{K} p_{\alpha_k}(x, z) \quad (26)$$

The coherent compounding method adds the beamformed radiofrequency signals from the multi-angle transmissions before the demodulation process, which keeps phase information when executing the compounding process, and thus effectively removes the random noise and enhances the signal intensity[70]. We use 19 steering angles with 1° step size to reconstruct images. Plane waves with a smaller step size than 1° cannot achieve a synthetic focusing effect. The imaging contents are too similar for each angle and the accumulated artifacts caused by grating-lobes lead to a low SNR_e. When the step size is too big, the overlap between plane waves, and thus the SNR_e, decrease (Supplementary Fig. 25). The most appropriate step size (1° in this work) yields the most constructive interference of different plane waves in the tested region, ensuring the highest SNR_e (Fig. 2b). Large angle numbers enhance the SNR_e because the coherent superposition of all steered images contribute to the compounding elastographic image. When extra plane waves cannot contribute substantially to the central rectangular region directly beneath the transducer array, the SNR_e saturates. However, the time required for reconstructing the images grows linearly with the number of steering angles. To save the time for image reconstruction, especially the time for ultrasound wave transmitting/receiving and post-processing of receive beamforming (Supplementary Fig. 26), we use 19 steering angles in this work (Fig. 2c).

Note S14. Differences in strain distributions obtained by the stretchable and commercial probes

The reasons why the two strain distributions differ in some details, though having the same shape, can be categorized into two parts. One is from the different testing methods, and the other is due to the differences in probe properties.

First of all, the stretchable array is able to attach to the surface and acquire all radiofrequency signals from different slices at one time. While the commercial probe (Verasonic P4-2v) is linear-shaped, and we had to manually move the probe along the elevation direction slicing the project into multiple segments for the reconstruction. Unlike the stretchable ultrasonic probes, the commercial probes cannot always be perpendicular to the curved irregular surface of the breast phantom when testing multiple cross-sections. Such various testing angles cause the different tumour sizes and locations in 2D images compared with those from the stretchable array.

Secondly, the spatial resolutions in lateral, axial, and elevational directions of the commercial ultrasonic probe are better than those of the stretchable ultrasonic array. The lateral resolution of ultrasonography depends on the beamwidth of the ultrasound wave. Specifically, a finer pitch and longer aperture improve the focusing effect, which narrows the ultrasound beam at the focal point. Since the commercial probe is superior to the stretchable array in both pitch and aperture, it achieves a better lateral resolution than the stretchable array. The axial resolution depends on the frequency and bandwidth of the array element. The commercial and stretchable probes have the same resonance frequency (3 MHz). However, the commercial probe has a thick backing layer of centimetres, which endows it with a narrow spatial pulse length and a wide bandwidth (>75%). As a result, it has a high axial resolution. However, the backing layer of the stretchable probe is relatively thin, mainly for the benefit of better mechanical compliance to tightly conform to the human skin. Therefore, the bandwidth of the stretchable array is relatively narrow, causing inferior axial resolution. The commercial probe also performs better in the elevational resolution than the stretchable ultrasonic probe since the length of each element is larger than that of the stretchable probe. It improves the convergent ultrasonic beam in the elevational direction so that the interferences from adjacent slices are less in each 2D image. These factors collectively lead to differences between the original 2D images of the commercial and stretchable probe, further influencing the 3D reconstruction. An optimized transducer design with finer pitch, larger aperture, and longer elevational length will be explored in future studies to compensate for the performance weakness of the stretchable array.

Note S15. The modulus contrast mapping of the cyst phantom

The mapped modulus contrast of the cyst phantom does not reflect the actual modulus ratio, but only demonstrates the relative stiffness of the cyst and surrounding matrix, because there is only fluid inside the cyst and is absent of scattering particles or echogenic signals from the fluid (Fig. 3b, Supplementary Fig. 31b, and Supplementary Fig. 32). Noises in the radiofrequency lines from the fluid are used for calculating cyst displacements. Therefore, the measured displacements in the cyst are artifacts. Those artifacts generate modulus ratio mapping that can only provide a relative modulus distribution. The relative modulus distribution provides only a qualitative structural appearance of the cyst that facilitates its recognition and diagnosis in clinics.

Note S16. Multi-site tissue mapping and protocols of the exercise and physiotherapy

All human tests were approved under University of California, San Diego Institutional Review Board (IRB) protocol 801085, which was obtained retrospectively due to the delays caused by COVID disruptions. We mapped the tissue modulus at five different locations in the human body. For measuring the shoulder joint, the upper limb was drooped naturally in relaxation, with the palm facing inward. The device was applied conformally to the lateral side of the shoulder joint, on the midpoint of the medial head of the deltoid. For measuring the forearm, the upper limb was fully stretched on the table with the palm upward. Since the palmaris longus tendon is an essential anatomical landmark, the location of the device was recognized easily by exploring along the tendon, which was the midpoint of the muscle belly of the palmaris longus. For measuring the thigh, the subject laid on the back with the lower limbs stretched and relaxed, keeping the feet upwards. The device was placed on the rectus femoris, at the medium level between the upper pole of the patella and the greater trochanter of the femur. For measuring the calf, the subject stood vertically with feet together and forward. The location of the device was the midpoint of the muscle belly of the gastrocnemius medial head. For measuring the upper arm, the elbow joint was passively flexed at ninety degrees, with the upper arm lying on the table and the palm towards back. The device was placed at the midpoint of the muscle belly of the biceps brachii. In all tests, the device was placed on the medium site of the medial and lateral edges of all of the muscle bellies, parallel to the long axis of the upper or lower limbs.

Muscle has a heterogenous structure. To avoid anatomical differences as much as possible, in this study we have measured muscles, such as in the belly areas, which have a relatively homogenous structure and high measurement repeatability on different individuals. Due to the small footprint (12 mm × 12 mm) of the stretchable ultrasonic array, the full scope of the anatomic structure of the upper arm cannot be displayed. To demonstrate the relevance of the measurements, we mapped the upper arm on the same subject using a commercial ultrasonic shear-wave elastography system (GE Logiq E9 Ultrasound System, C1-6 probe), due to its higher spatial resolution than MRE. Additionally, MRE is also based on shear-wave elastography, which uses a paddle-like device to transmit the vibrations into the subject. The paddle has a large, rigid base that is not suitable for the upper arm, leading to poor coupling and many artifacts[71]. Due to its relatively larger footprint, the commercial probe can provide a broader sonographic window than the wearable patch. As seen in Supplementary Fig. 50, the entire anatomic structure of the upper arm is visualized in both transverse and longitudinal views. Key components have been labelled in the B-mode images. To correlate the results from the commercial system with those from the patch, we did more elastographic measurements in longitudinal view, with a zoomed-in window focusing on bicep brachii and brachialis (Supplementary Fig. 50b). We have taken multiple slices of B-mode images along the short axis of the upper arm, from which representative structures, such as the fascia in the bicep brachii and the interface between the bicep brachii and brachialis, highly match with slices from the patch. Additionally, we have measured the modulus of muscles using the commercial system. Due to the limited size of the window for selecting the region of interest, the modulus of bicep brachii and brachialis can only be measured separately. We have calculated the stiffness ratios of two muscles, which are very close to those tested by the patch (Supplementary Fig. 50b). The high correspondence between the results from the commercial system and the patch demonstrates the high relevance of the measurements by the stretchable ultrasonic patch to the real-world applications.

To verify the reliability, six people (four males and two females) with an average age of 25, who were physically healthy, without injury of the upper arm within the past 6 months, volunteered for this study. To avoid any confounding effects of muscle fatigue and soreness, participants stopped any physical activity for one week prior to the experiment. The same researcher performed the experiments and collected data. For the testing of intra-session reliability, all subjects came to the laboratory for one visit. During the testing, subjects were asked to sit down and place their left arm on a table with their elbow bent perpendicularly. The same device was used to test the same part of the upper arms along its long axis. Measurements were performed five times for each subject with 1 minute of rest between each measurement. For the testing of inter-day reliability, all subjects came to the laboratory for two visits, with the second visit three days after the first visit. The two visits were each performed at the same time of day to minimize the effects of diurnal variation. During each visit, the subjects were asked to sit down and put their left arms on the table. The elbow was always bent perpendicularly during the testing. The same device was used to test the same part of the upper arms along its long axis for both visits.

For in vivo studies, a healthy volunteer without any upper extremity injuries or soreness was selected to perform eccentric contractions of the elbow flexor muscles. The human experiments in this study are carried out following reported protocols[9,72,73]. All subjects signed informed consent forms. To ensure the effectiveness of the unaccustomed exercise, the subject was required to use the non-dominant arm to do the exercise. The measurements of experimental groups started when the muscle soreness caused in the control group has completely gone. Following the existing model, the subject maintained a seated position and performed the exercise with a 7.1 kg dumbbell. The forearm was forcedly extended from a fully flexed position. The exercise consisted of six sets of ten maximum eccentric contractions of the elbow flexors with 90 seconds of rests between sets. For collecting the data of the control group, the biceps brachii was tested immediately after the exercise. We ran a total of 20 tests,one per minute, which demonstrated the serial monitoring of the device within a short period of time. We did the same measurements 3 hours, 6 hours, and 1 to 5 days after the exercise. For each measurement, we ran five tests with one per minute (Supplementary Fig. 48b). Massotherapy and hyperthermia were applied every day before each test. For the massotherapy, a massage gun (Zfitei, China) was used for 20 minutes to vibrate the biceps brachii. For the hyperthermia, a hot towel was wrapped around the upper arm for 20 minutes. The modulus distribution of each test was reconstructed, from which a 12 mm × 5 mm window was picked and the mean and standard deviation of the modulus were calculated. The normalized modulus contrast (Fig. 5f) could be calculated by equation (21), which intuitively reflects the degree of muscle rehabilitation from injury. The coefficient of variation among all tests could be calculated by the equation (22)[74].

$$Normalized\ modulus\ contrast = \frac{\mu_{after}}{\mu_{before}} \quad (27)$$

$$\text{Coefficient of variation} = \frac{\sigma}{\mu_{after}} \text{(28)}$$

where μ_{after} and μ_{before} are the average modulus of biceps brachii before and after exercise, respectively, and σ is the standard deviation of the modulus distribution. Lower variation of the hyperthermia (Fig. 5g) indicates its better efficacy of recovering the muscle injury.

The muscle has different mechanical properties in different directions. In our study, the applied compressions are perpendicular to muscle fibers. However, because muscles are typically incompressible with a Poisson's ratio of 0.5[19], the applied compression also caused significant extension of fibers along the axial direction (axial is the direction along the long axis of the arm, Supplementary Fig. 46). As a result, the axial stiffness of fibers is also sensed by the applied compression. Because we use an isotropic model to infer tissue modulus, the obtained modulus should be interpreted as an "effective" modulus that measures the average stiffness over all orientations. This is likely why traditional clinical diagnosis can still identify damaged muscle regions with increased stiffness through characterizations that are only perpendicular to the muscle fiber directions[75]. For instance, in abdominal palpation, as an essential physical examination in clinical practice, the condition of the abdominal muscles is tested by applying compression and manually feeling for the tissues' mechanical responses[76]. Any abnormally stiff muscles can then be differentiated[75,76] because muscle damage leads to increased stiffness of muscle fibers in all directions, and thus to increased "effective" stiffness of muscles. Therefore, the characterization perpendicular to the muscle fiber directions in this study is valuable for identifying regions of muscle damage.

Additionally, the serial measurements in this study are consistent with the temporal evolution of exercise-induced muscle injuries reported using other methods. Clinical observations of muscle performance following exercise[75,77,78] and histological analysis[79,80] both confirm the respective metrics in this study. Moreover, both massotherapy[4] and hyperthermia[78] are shown to significantly mitigate muscle damage and increase the recovery speed, consistent with our results. Collectively, it is evident that the characterization of muscle stiffness along the direction perpendicular to the muscle fibers can accurately track muscle recovery from exercise-induced injuries.

To further verify the feasibility of our device for serial monitoring of muscle damage, we decided to increase the sample size to 16 (14 males and two females, average age: 25). This sample size was highly comparable to those of many relevant literatures[9,72,73,81-83] and has enough power to demonstrate the feasibility of the technology. In the experiments, subjects performed the eccentric exercise and natural recovery using their non-dominant arm. We used both maximal voluntary contraction and the stretchable ultrasonic array to measure the muscles before and after 1 day, 2 days, and 3 days of exercise. During maximal voluntary contraction measurements, an electrical dynamometer was used. Subjects always kept a seated position on a chair with an elbow angle of 90°. We tested the maximal isometric elbow flexion torque with 5 s duration of each test. Three trials were done each time with 2 mins rest between each trial and the trial with the highest torque was recorded and analyzed[9]. The testing procedures of muscular stiffness by the stretchable ultrasonic array were the same as before. The results are shown in Extended Data Fig. 4.

Note S17. Mechanism of delayed onset muscle soreness

Delayed onset muscle soreness is a common muscle injury that can be classified as an overexertion-functional muscle disorder[84]. There are many clinical mechanisms to explain this disease, and the injury mechanism is the one that is widely accepted among the others[75]. The external load applied in the eccentric exercise is much more than the isometric force generated by the muscle fibers. The overload causes muscle fibers to be lengthened and exposed to the elevated tension, which results in the loss of myofibrillar integrity and micro-structural damage of sarcoplasmic reticulum, transverse tubules, and sarcolemma. The disruption of the sarcolemma induces an increase in the concentration of intracellular calcium, enabling the myosin to attach to the actin and form the cross-bridge. The thin filaments slide over the thick filaments when the myosin heads pull the actin, which causes muscle contracture and leads to an increase in muscle stiffness[9,85-89]. The movement of the calcium ions, on the other hand, activates the pathway of myofibrillar repair. The remodeling of the protective proteins and the formation of the sarcoplasmic reticulum progressively preclude the osmosis of the calcium ions[75,90,91]. The modulus peak occurs when the sarcolemma is completely repaired, followed by the accelerated recovery of myofibril and the relief of the symptoms of delayed onset muscle soreness.

The inflammation response following the ultrastructural damage of muscle is accepted as another important mechanism for the interpretation of the delayed soreness perception[75]. The symptom caused the subject to feel mild fatigue after one day and an intensive soreness two to three days after exercise, as it took time for inflammatory cytokines to accumulate and abruptly release[75]. The accumulation of leukocytes (primarily neutrophils) is observed in the muscle in 3 to 24 hours after exercise[79]. Mast cells, playing an essential role in the inflammation response, are also infiltrated into the muscle in the same period[92]. Increased monocytes/macrophages are observed 48 hours after eccentric exercise, lasting for five days or even longer[92].

Moreover, the proposed two treatments have the capability to not only alleviate the muscle pain, but also facilitate the recovery of the muscle damage and force production capability. It has been observed that massotherapy is able to decrease the serum level of some muscle damage and inflammatory markers, such as creatine kinase (CK), lactate dehydrogenase (LDH), interleukin-4, interleukin-6, and interleukin-10 (IL-4, IL-6, IL-10)[93-95]. Additionally, with the specific application, massotherapy improves the outcomes of muscle performance during delayed-onset muscle soreness regarding muscle maximal isometric force and peak torque[93]. The current explanation for this effect is that massotherapy increases blood and lymph flow, which facilitates the clearance of the biomarkers from the damaged tissue and blood, thus reducing the inflammatory response and promoting muscle recovery[91,94].

Also, it has been indicated that immediate low-level heat therapy significantly improves the physical functions of muscles, including plasma myoglobin level, muscle strength, range of motion, and pain scales[96,97]. One underlying mechanism of heat therapy is that it may contribute to pain relief via interacting with transient receptor potential vanilloid-1 (TRPV1) while transducing heat through neurons[98]. Meanwhile, a heat-induced increase in tissue blood flow promotes the clearance of inflammatory mediators and facilitates the supply of nutrients and oxygen to the injured sites, which accelerates muscle healing[96,98].

Note S18. Evaluation of repeated bout effect

The repeated bout effect could have an influence on the following exercise results after the first bout. But this effect is highly dependent on the intensity of the exercise and the time elapsed from the initial exercise bout. If the muscle damage caused by the first bout of exercise is not sufficient, it will not generate a protective effect in the second bout, and vice versa[99].

To further verify the influence of repeated bout effects and the efficacy of different physical treatments, we designed extra experiments to figure out if our experiment settings would suffer from the repeated bout effect on subjects 1 and 2. Results and analysis are shown in the following paragraphs and figures. These two subjects have firstly exercised and performed natural recovery, and then repeated the exact same procedure one month later. Note that both subjects did not feel obvious fatigue or pain before repeating the exercise. The normalized modulus contrasts for each subject are shown in Extended Data Fig. 3a and b. For both subjects, there is no significant difference between the results of the two experiments. Specifically, for subject 1, the normalized modulus contrast was ~1.0 before exercising, increased right after the exercise, continued gradually rising to ~3.0 until the second day, and then started to decrease since the third day to almost the original value on the fifth day. Subject 2 shows the trend alike. From the results above, we can tell that the experiments of exercise with a natural recovery procedure will not be influenced by the repeated bout effect after one full month of rest, which is consistent with the previous studies[75].

To further demonstrate the effectiveness of both treatments for muscle recovery, we then had another four subjects randomly divided into two groups, one for the massotherapy and the other for the hyperthermia (Extended Data Fig. 3c to f). In the initial bout, all of them had the same procedure of the eccentric exercise followed by natural recovery. After one month's rest, one group had the eccentric exercise with massotherapy and the other had the exercise with hyperthermia for treatment. For the first group of subjects

3 and 4, the modulus contrast before exercise was 1.0. During the natural recovery, the value reached the peak on the first day after exercise, and gradually decreased to the original state within the subsequent four days. In contrast, we applied massotherapy to the subjects in their second round of experiments. It’s noticeable that the peak value was at the sixth hour right after their exercise, when the modulus contrast began to decrease on the first day instead of the second day with natural recovery. The overall values at each time stamp are averagely smaller than the first round of experiments, showing that the massotherapy indeed helped the muscle recovery, and predictably it took less time for a full recovery. Like the first group, the second group of subjects 5 and 6 had gone through all the same procedures only with hyperthermia instead of massotherapy. Without hyperthermia, the modulus contrast reached the peak on the first day after exercise, followed by a continuous decline. With hyperthermia, the overall modulus contrast was comparably smaller and there was no dramatic change during recovery. Those two groups with randomly assigned four subjects showed a similar trend to that in the original manuscript.

The healing process may also be influenced by the consequences of repeated bout effects: the second and the third bouts likely caused less damage than the first bout, depending on the intensity of the exercise and the time elapsed from the initial exercise.

In this work, the results showed no occurrence of the repeated bout effect in subjects, probably because the sample size in this work was small. According to some other studies on a large sample size[100,101], the repeated bout effect still persists even after resting for several months.

With that being said, this does not influence the conclusion of this study. The contribution of this work is to demonstrate the feasibility of the stretchable ultrasonic array for serial monitoring of tissue stiffness. Applying massotherapy and hyperthermia could create different muscle conditions for the device to monitor, even if there are repeated bout effects involved to accelerate the muscle recovery. In future work, we could potentially use this technology to perform more mechanistic studies on the effects of muscle damage and healing on a large population.

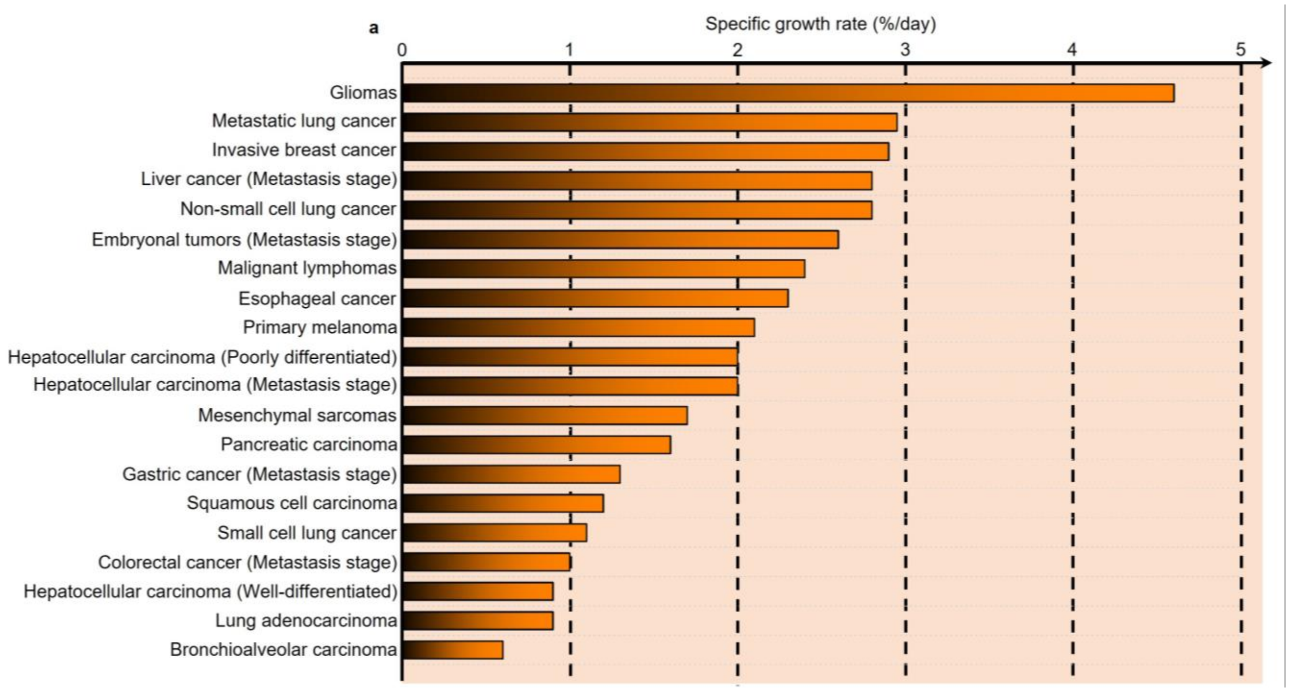

b

Diseases	**Muscles**	**Functions of the stretchable ultrasonic patch**	**Citations**
Myositis	Thigh/arm muscles	Rehabilitation	4
Cerebral palsy	Lateral gastrocnemius	Rehabilitation	5
Stroke	Biceps brachii muscle	Diagnosis/Rehabilitation	6
Amyotrophic lateral sclerosis	Quadriceps muscle	Diagnosis/Rehabilitation	7
Muscle damage	Posterior thigh muscles	Diagnosis/Rehabilitation	8
Delayed onset muscle soreness	Biceps brachii muscle	Diagnosis/Rehabilitation	9
Tendinopathy	Achilles tendon	Diagnosis/Rehabilitation	10
Parkinson's disease	Biceps brachii muscle	Diagnosis/Rehabilitation	12

Supplementary Figure 1. Significance of the stretchable ultrasonic array for serial tissue modulus monitoring. (**a**) Statistics of over 20 types of cancers with a high specific growth rate. The lack of serial, long-term monitoring prevents quick and effective tracking of tumor growth, which represents a critical unmet need in clinics. (**b**) Summary of some common muscle diseases relevant to the muscle modulus. The diagnosis and rehabilitation processes of multiple musculoskeletal diseases and injuries also require frequent examinations and long-time monitoring of the muscle modulus. A stretchable ultrasonic array can meet those needs that cannot be addressed by any existing approaches.

Measurement modalities	Wearability	Testing targets	Testing depths	Spatial resolutions	Mapping	Citations
Suction	Too bulky	Skin	<1 mm	>6 mm	0D	13
Compression	Too bulky	Shallow tissue	<1 cm	>5 mm	0D	14
Extension	Too bulky	Skin	<2 mm	>30 mm	0D	15
Small-scale indentation	Too bulky	Skin	<20 µm	>5 µm	2D	16
Rigid ultrasonic array	Too bulky	Deep tissue	>4 cm	>0.1 mm	3D	102, 67, 103, 104
MRE	Too bulky	Deep tissue	>4 cm	>0.9 mm	3D	105, 106
Optical coherence elastography	Too bulky	Skin	<0.6 mm	>6.1 µm	3D	107,108
Flexible piezoresistive cantilevers	Yes	Skin	<20 µm	>40 µm	0D	30
Conformal piezoelectric thin film	Yes	Skin	<2 mm	>0.3 mm	2D	31
Tactile sensor	Yes	Shallow tissue	<5 mm	>2 mm	2D	32
Needle-shaped piezoelectrics	Invasive	Shallow tissue	<4.5 mm	>0.5 mm	0D	33
Stretchable ultrasonic array	Yes	Deep tissue	>4 cm	>0.56 mm	3D	This work

Supplementary Figure 2. Comparison among all existing methods for tissue modulus mapping. Different comparison metrics and relevant citations are listed in different columns. The major advantage of the stretchable ultrasonic array in comparison with the conventional methods is the combined merits of being wearable for serial, noninvasive, and 3D monitoring of deep tissues.

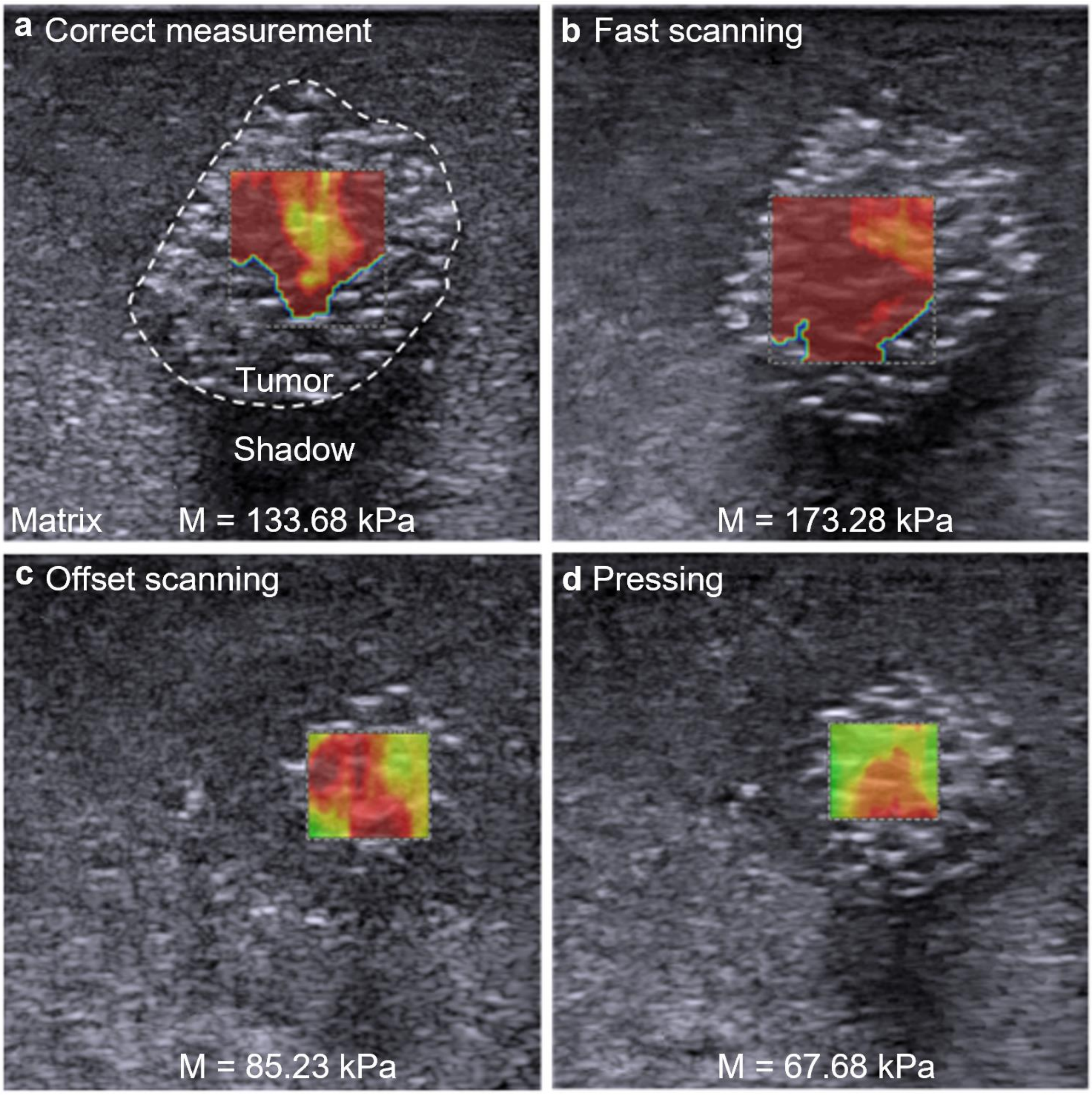

Supplementary Figure 3. Common pitfalls in commercial ultrasonic shear-wave elastography operations. Images of a breast tumour phantom (**a**) with standard scanning, showing the correct size and stiffness of a tumour, with (**b**) fast scanning, (**c**) offset scanning angle (by ~10 degrees), and (**d**) moderate pressing (~50 Newtons), causing blurry images, size deformation, and inaccurate stiffness measurements of the tumour. M: Young's modulus.

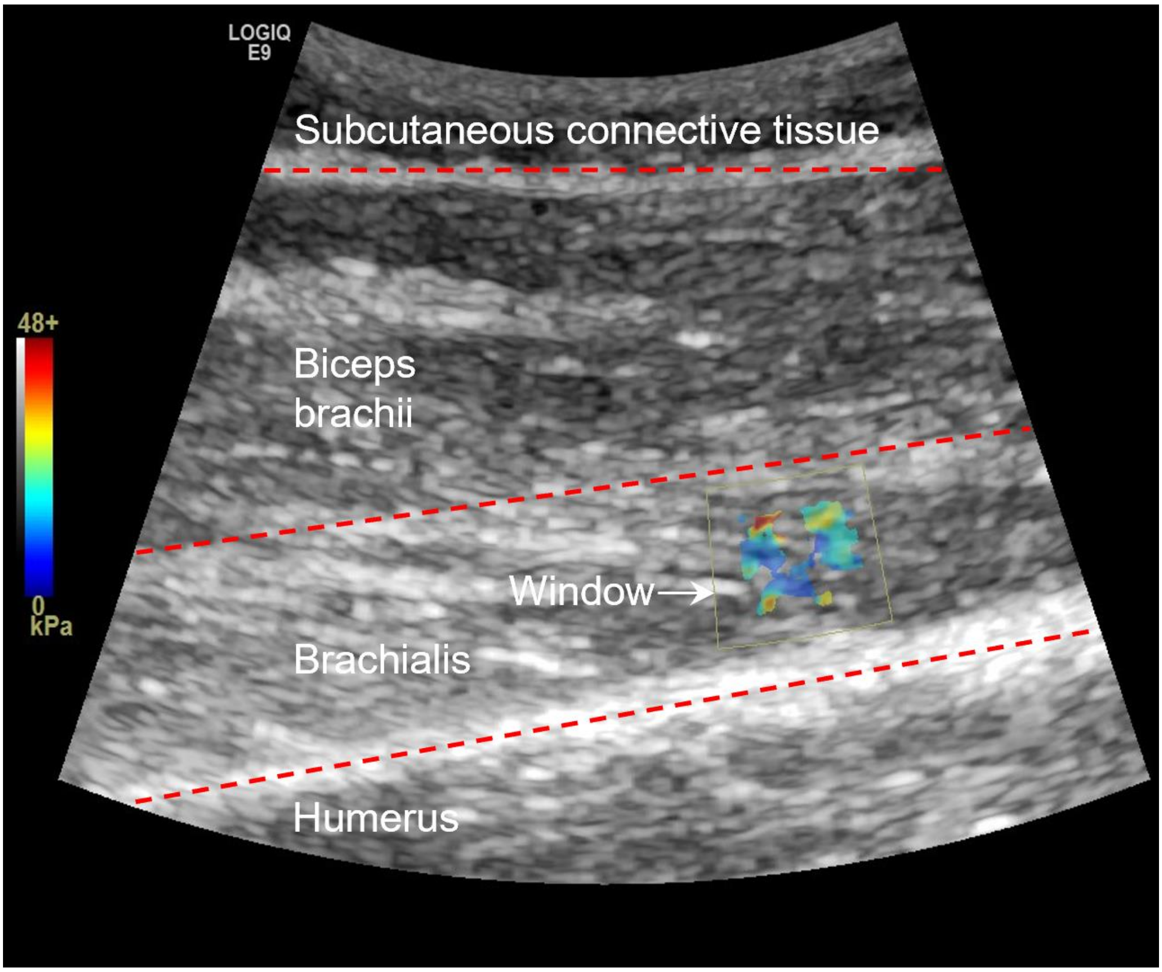

Supplementary Figure 4. Modulus imaging by a commercial ultrasonic shear-wave elastography machine. The window to select the region of interest is too limited to map all components and tissues simultaneously.

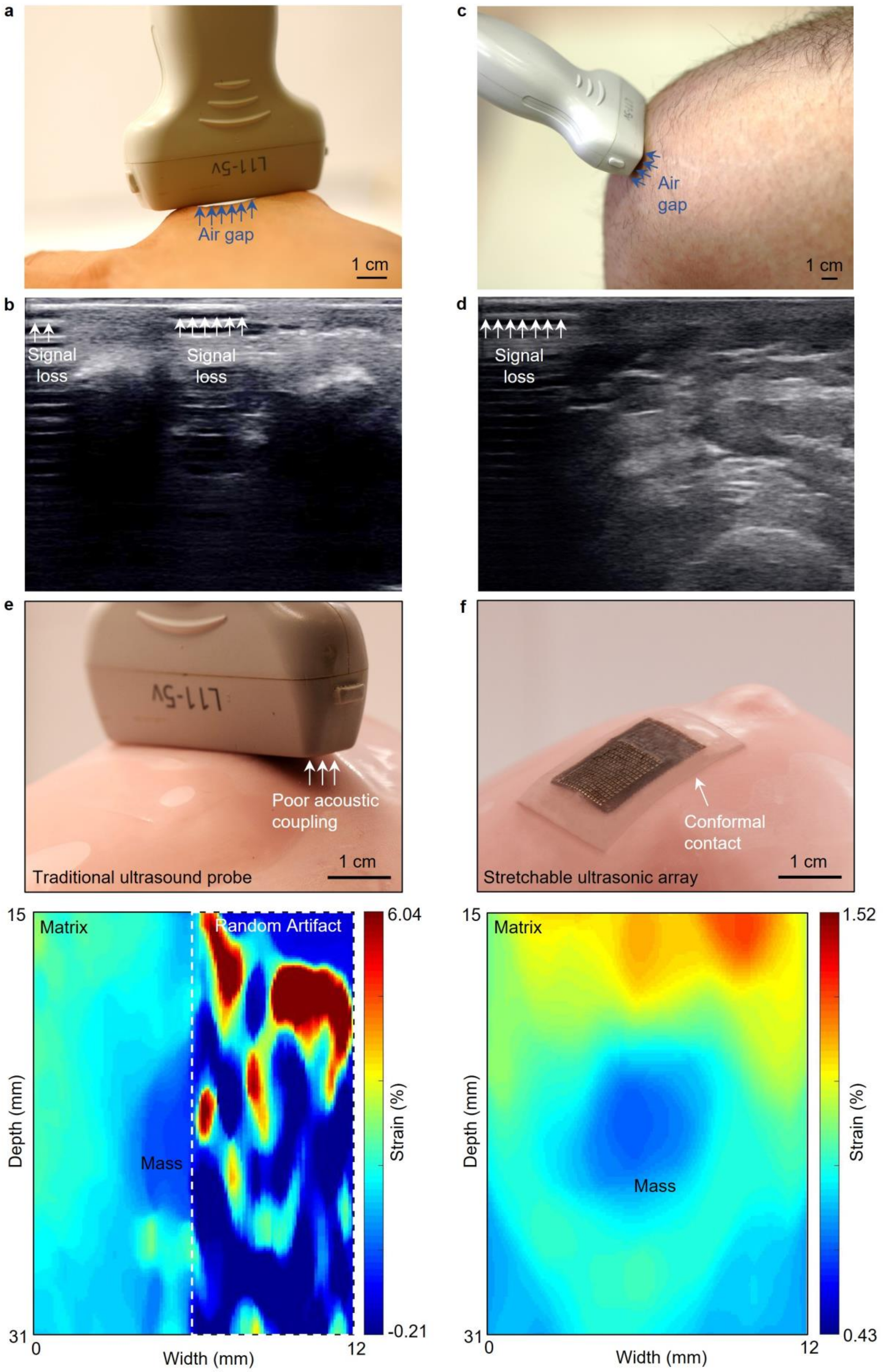

Supplementary Figure 5. Testing performance of the traditional rigid ultrasound probe and the stretchable ultrasonic array on curved surfaces. (**a**) Optical image showing the testing of a commercial rigid probe on joints of the hand and (**b**) its corresponding B-mode image. (**c**) Optical image showing the testing of a commercial rigid probe on the knee and (**d**) its corresponding B-mode image. Poor acoustic coupling caused by curved surfaces leads to signal loss in B-mode images. In addition, a breast phantom was tested by (**e**) a traditional rigid ultrasound probe and (**f**) a stretchable ultrasonic array. The corresponding strain images are displayed at the bottom. The traditional rigid ultrasound probe cannot conform to the curved surface. The air gaps between the rigid base and the phantom surface cause poor acoustic coupling and thus information loss and artifacts inside the white dashed box. The resulting red and yellow patterns are random artifacts with abnormal strain values. In contrast, the intimate and seamless contact between the stretchable ultrasonic array and the phantom surface enables ideal acoustic coupling, leading to high-quality imaging with a comprehensive reconstruction of the internal structure.

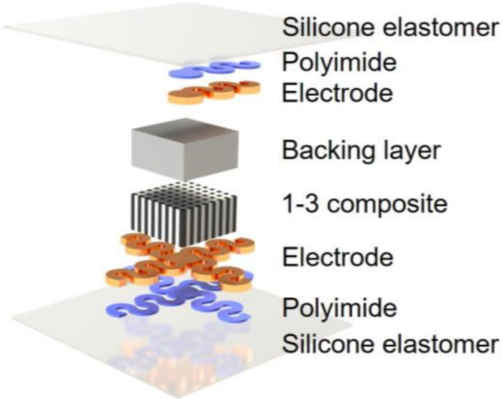

Supplementary Figure 6. Schematics of the exploded view of one element. All components have been labelled to illustrate the structure of an element.

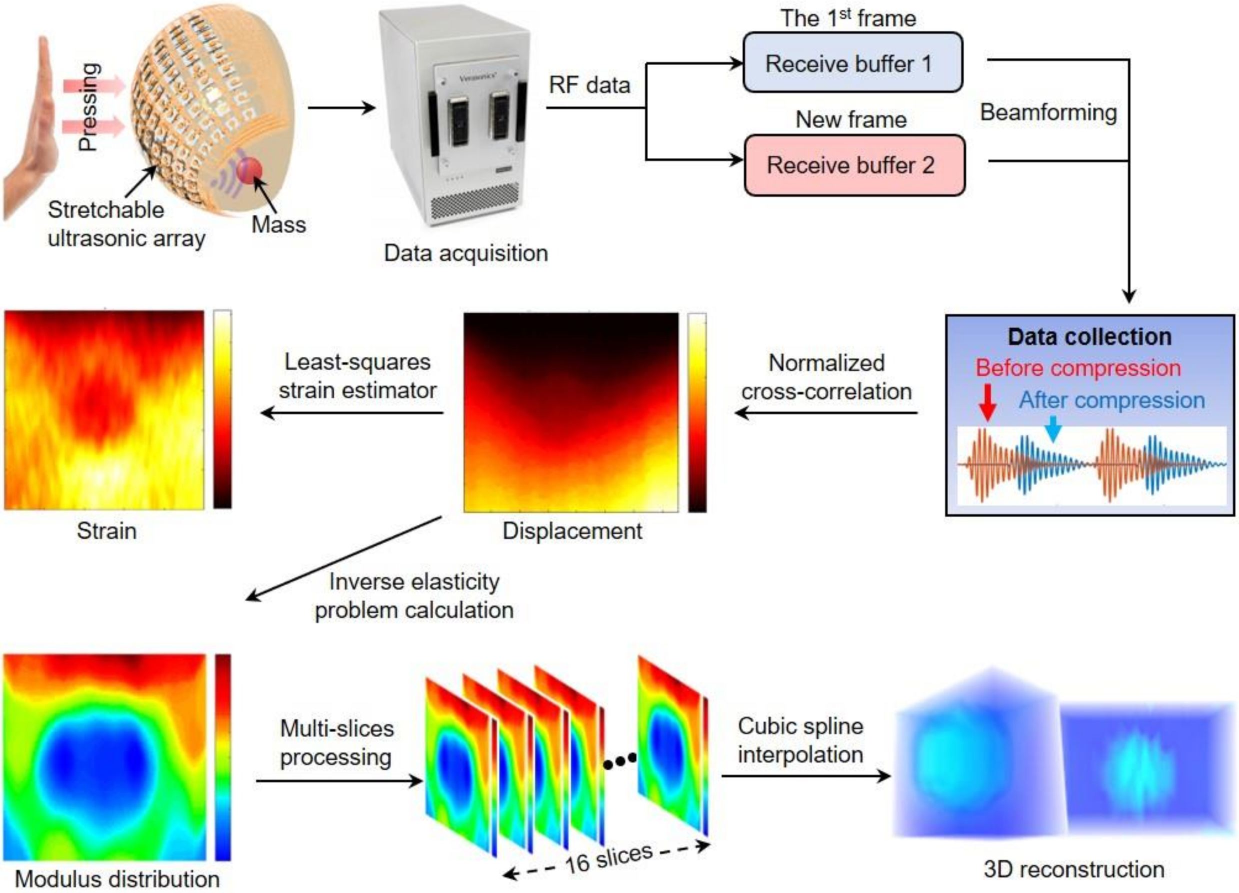

Supplementary Figure 7. The workflow of reconstructing elastographic images by the stretchable ultrasonic array. A multichannel Verasonics system is used to acquire the radiofrequency signals from the transducers. The pre-compression frame will be stored at the receive buffer 1 and the after-compression frame will be stored at the receive buffer 2. Then, receive beamforming will enhance the sonographic signal-to-noise ratio of these two frames. The beamformed radiofrequency data will generate the displacement field by using the normalized cross-correlation algorithm. The least-squares strain estimator is then applied to derive the strain field from the displacement field. The inverse elasticity problem calculation will reconstruct the modulus mapping based on the displacement field. The Amira software reconstructs the 3D image by integrating all slices of 2D images.

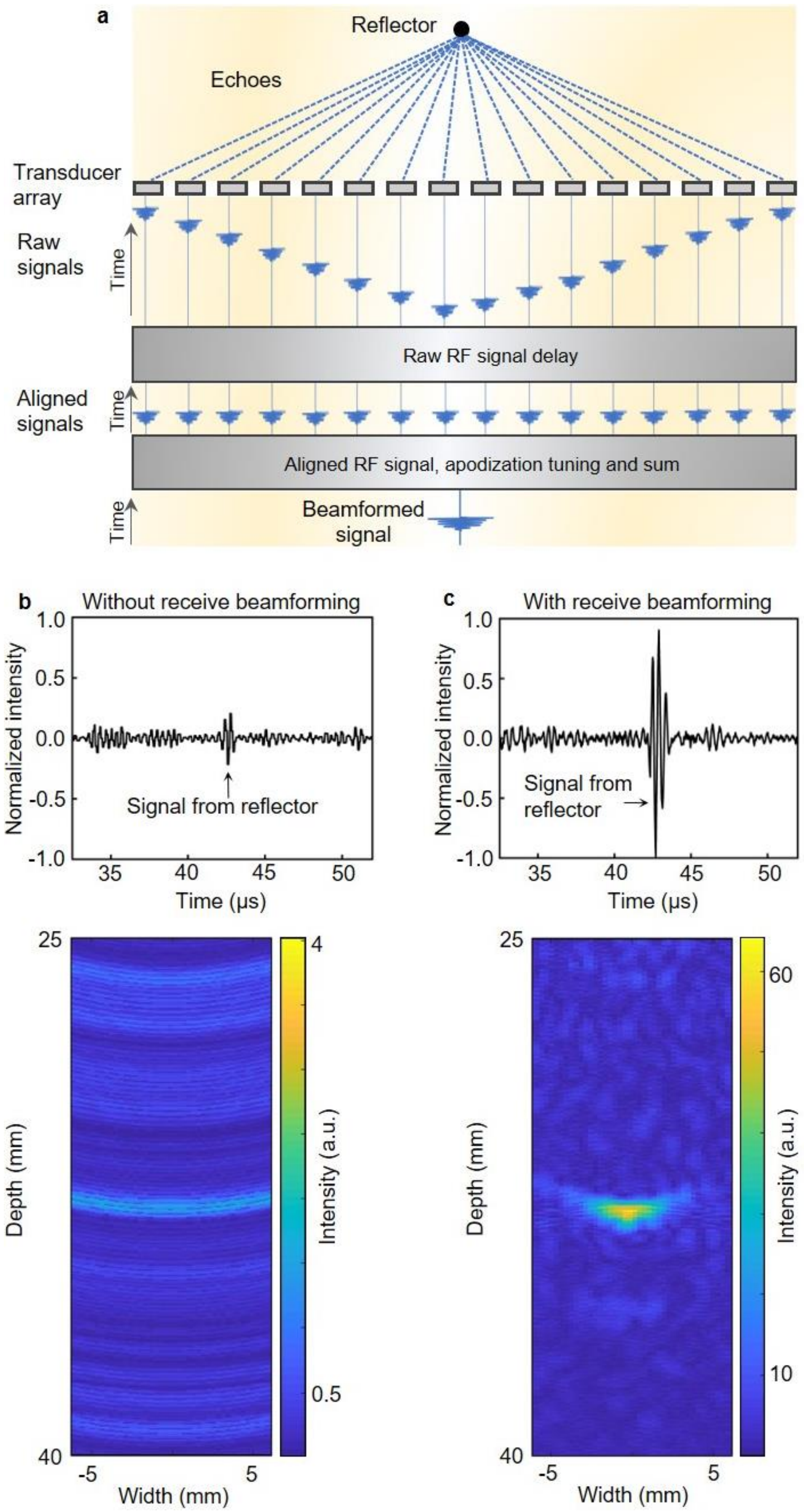

Supplementary Figure 8. Effects of the receive beamforming. (**a**) A schematic plot showing the process of the receive beamforming. A phantom with a reflector inside is tested by a 1×16 linear array. The raw signals are captured by the transducer array showing a certain profile based on the element locations. These raw signals are then aligned by adding different time-delays and summed to obtain a beamformed radiofrequency signal. The reflected signals (**b**) without and (**c**) with receive beamforming are plotted. From the radiofrequency signals (top), it is obvious that the receive beamforming enhances the sonographic signal-to-noise ratio. The data intensity was normalized by the maximum intensity of the signal. Besides, from the 2D plot (bottom), the receive beamforming improves the lateral resolution.

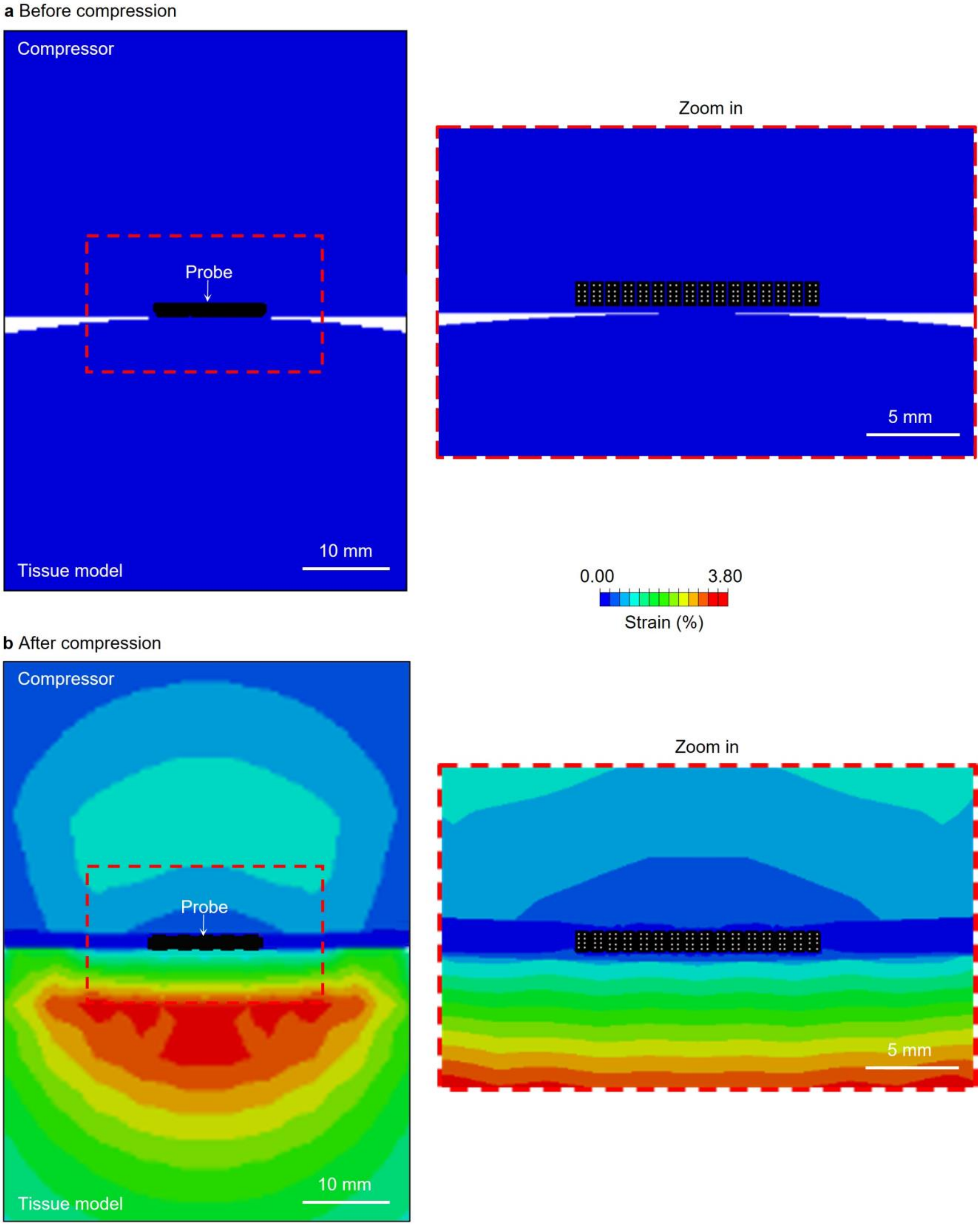

Supplementary Figure 9. Simulation of the change of transducers' locations by finite element analysis. After laminated with the device on the top, the tissue is deformed by a mildly applied force, so the strain is within the dynamic range. The strain distribution and locations of the transducer (**a**) before and (**b**) after compression are compared. The left column shows the entire strain field, and the right column illustrates details of the transducer array's locations. There is only ~0.02% change in the array's pitch after the compression, indicating minimal impact on the elastographic image quality after the compression. All images share the same color bar.

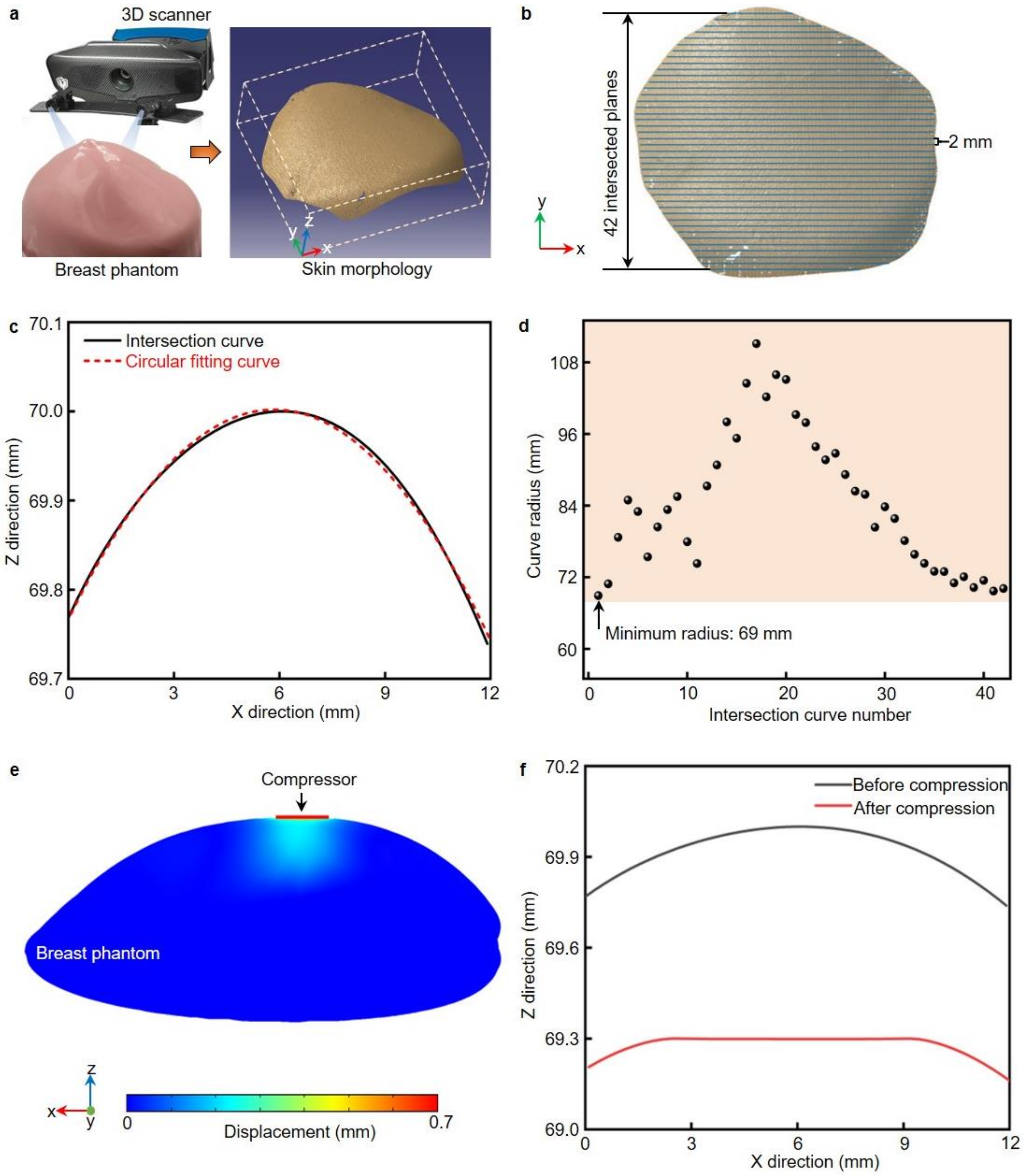

Supplementary Figure 10. Characterizing the skin curvature of a breast phantom. (**a**) A schematic plot of the setup for scanning the surface curvature by a 3D scanner. The small defects at the lower-left corner are due to the light reflection. These defects can be compensated by interpolation and thus do not frustrate the curvature calculation of the entire intersected interfaces. (**b**) The raw digital model, in the top view, of the skin profile reconstructed by the 3D scanner. 42 datum planes with a 2 mm interval are applied to intersect the digital model. (**c**) The curvature of each intersection interface is extracted using circular curve-fitting. (**d**) Distribution of the skin curvature of the 42 datum planes. The minimum curvature radius (i.e., the maximum curvature) across the entire surface is 69 mm in this project. The corresponding curve has been extracted to study the maximum deformation tolerance of the stretchable ultrasonic array and to determine the time-delay profile before and after compression. (**e**) COMSOL simulation of a 3D breast phantom model with the maximum skin curvature (radius: 69 mm, before compression). The compressor executes the 0.7 mm uniaxial displacement (1% strain in the z direction) to the breast phantom model and the post-compressive surface morphology has therefore been obtained. (**f**) The surface profile of the phantom before and after compression.

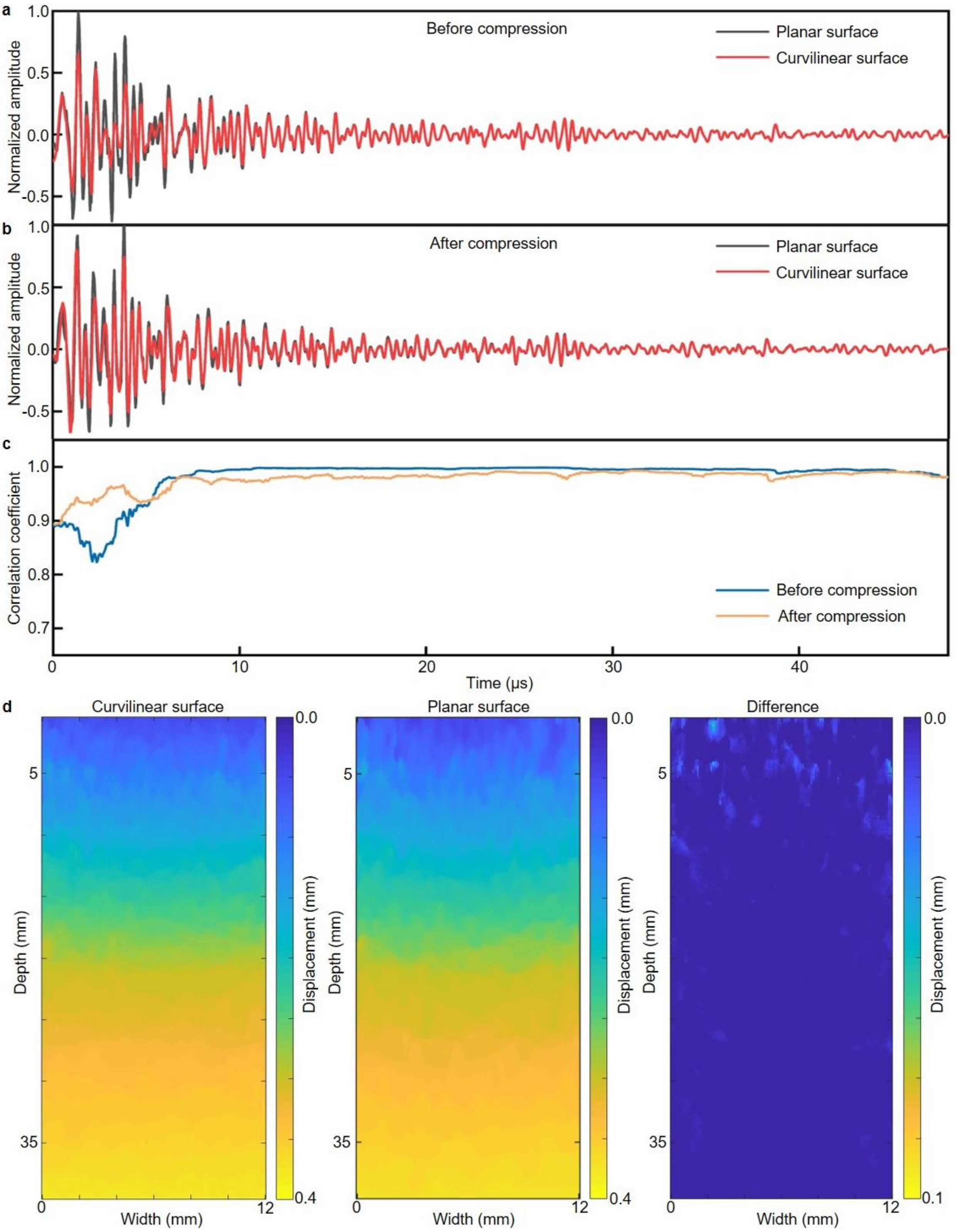

Supplementary Figure 11. Determination of the time-delay profile. (**a**) and (**b**) are simulated beamformed signals on planar and curvilinear surfaces before and after compression, respectively, and (**c**) their correlation coefficients. In (**a**) and (**b**), the data intensity was normalized by the maximum intensity of the signal. The high correlation coefficient of the signals from planar and curved surfaces means the time-delay profile on the planar surface is suitable for the curved surface. Using the same time-delay profile for both surfaces does not cause big distortions of the radiofrequency signals from the curved surface. (**d**) Simulated displacement fields on the curvilinear surface (left panel) and on a planar surface (middle panel). Both fields are derived by using the time-delay profile on the planar surface. The right panel shows the discrepancy in the distribution of the two fields.

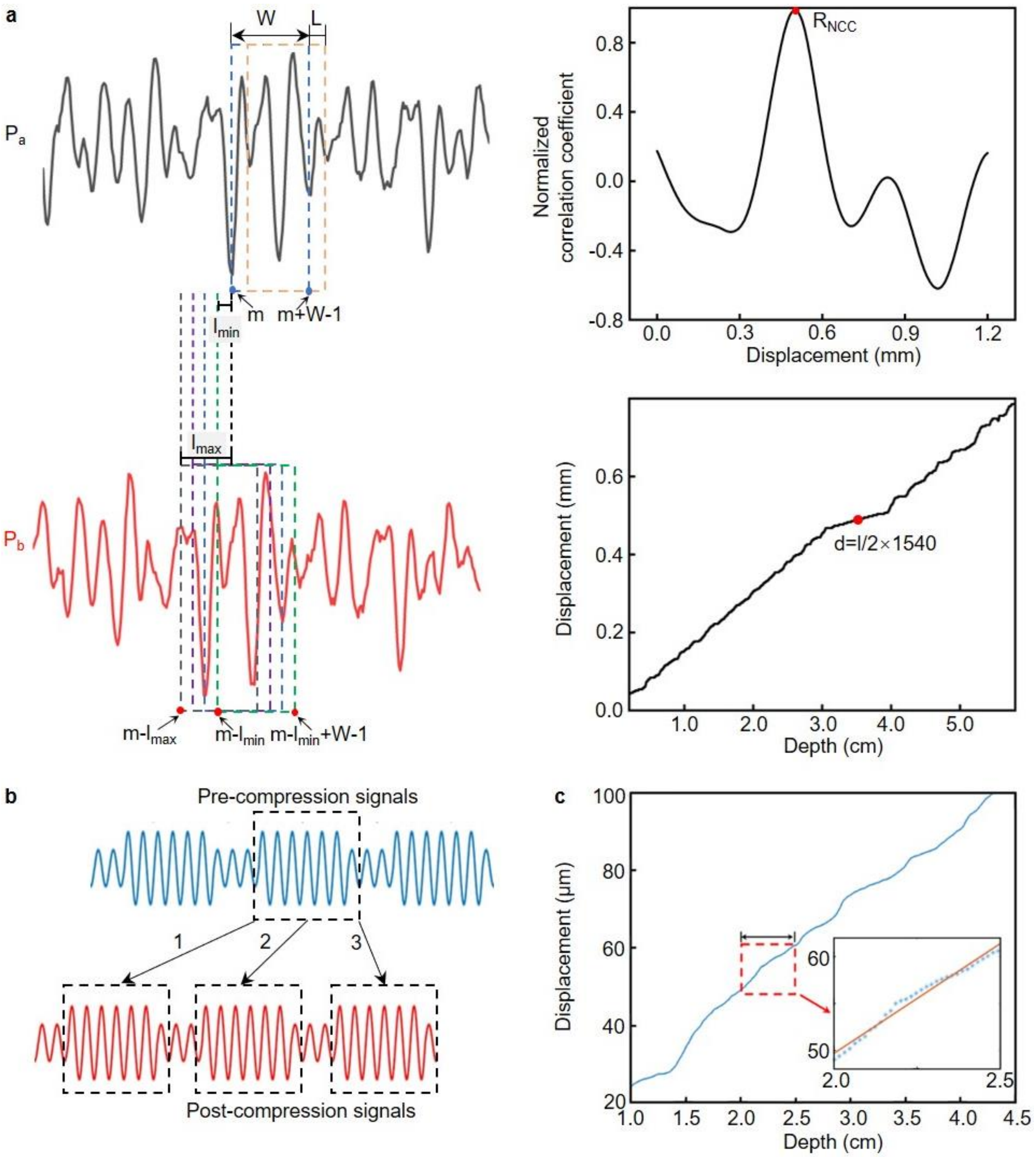

Supplementary Figure 12. Illustration of the normalized cross-correlation and least-squares strain estimator algorithms. (**a**) The process of displacement calculation. Sliding windows are applied to correlate the beamformed radiofrequency signals before and after compression. The displacement at a certain depth is defined as the one with the highest normalized correlation coefficient among all compared windows (top right panel). The displacement curve is derived by combing all displacement values along the depths (lower right panel). The details are in the Note S7. (**b**) A schematic figure showing the source of fluctuations in the displacement curve. Signals in windows 1, 2, and 3 are adjacent to each other. After compression, the pre-compression signals may correlate from window 1, or 2, or 3 since they are very similar and the corresponding correlation coefficients are almost the same. It causes some confusion to the normalized cross-correlation algorithm and thus leads to tiny fluctuations in the displacement curve. (**c**) The displacement along the axial direction and a window used to estimate the local strain. The inset image illustrates the raw (blue dots) and the fitted displacements by a least-squares strain estimator (red line), which can smooth out the fluctuations in the displacement. The calculated strain is the slope of the fitted displacement curve. The details are in the Note S8.

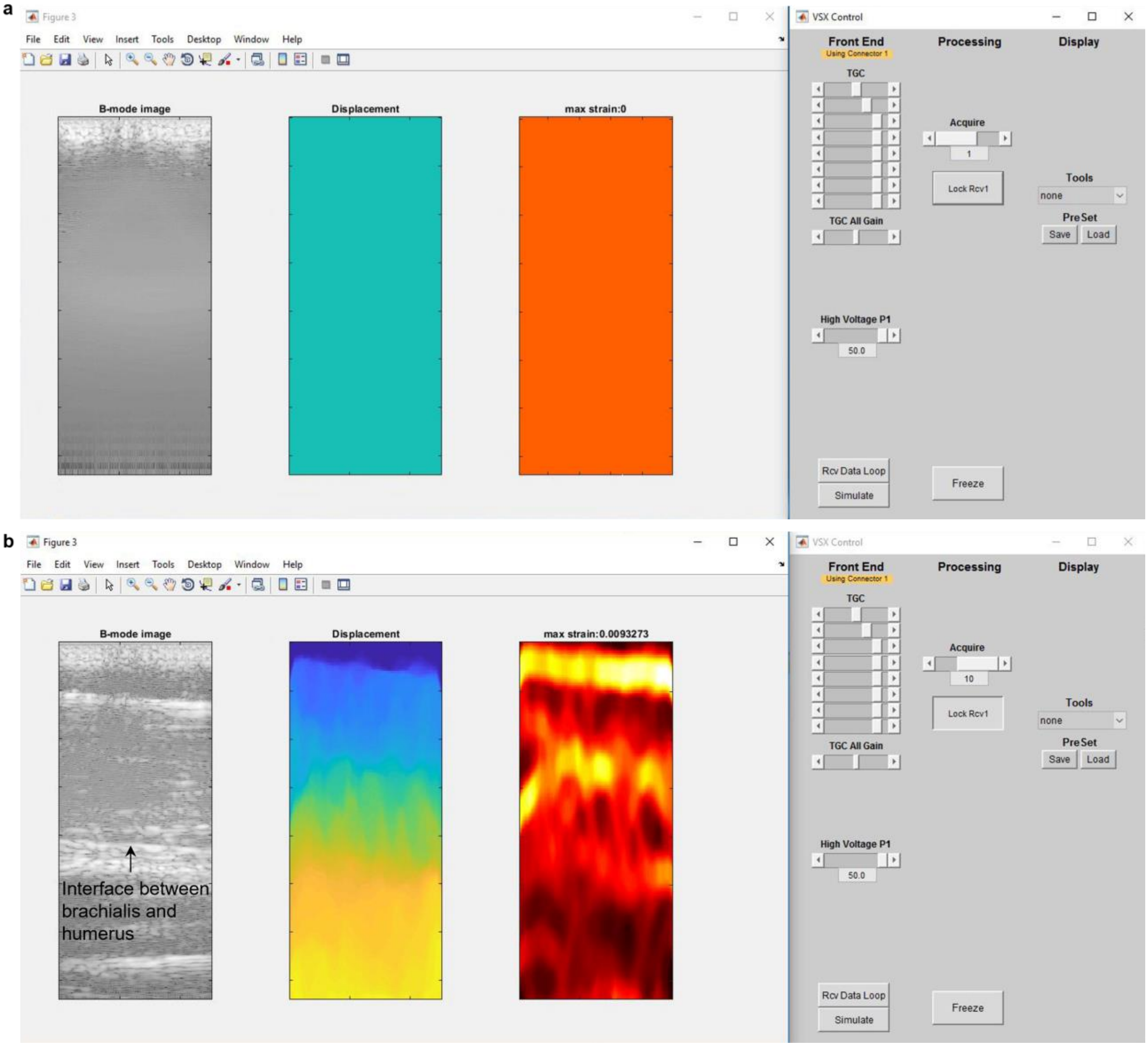

Supplementary Figure 13. The layout of the graphical user interface. B-mode, displacement, and strain distributions (**a**) before and (**b**) after compression are shown on the left. The control panel is on the right.

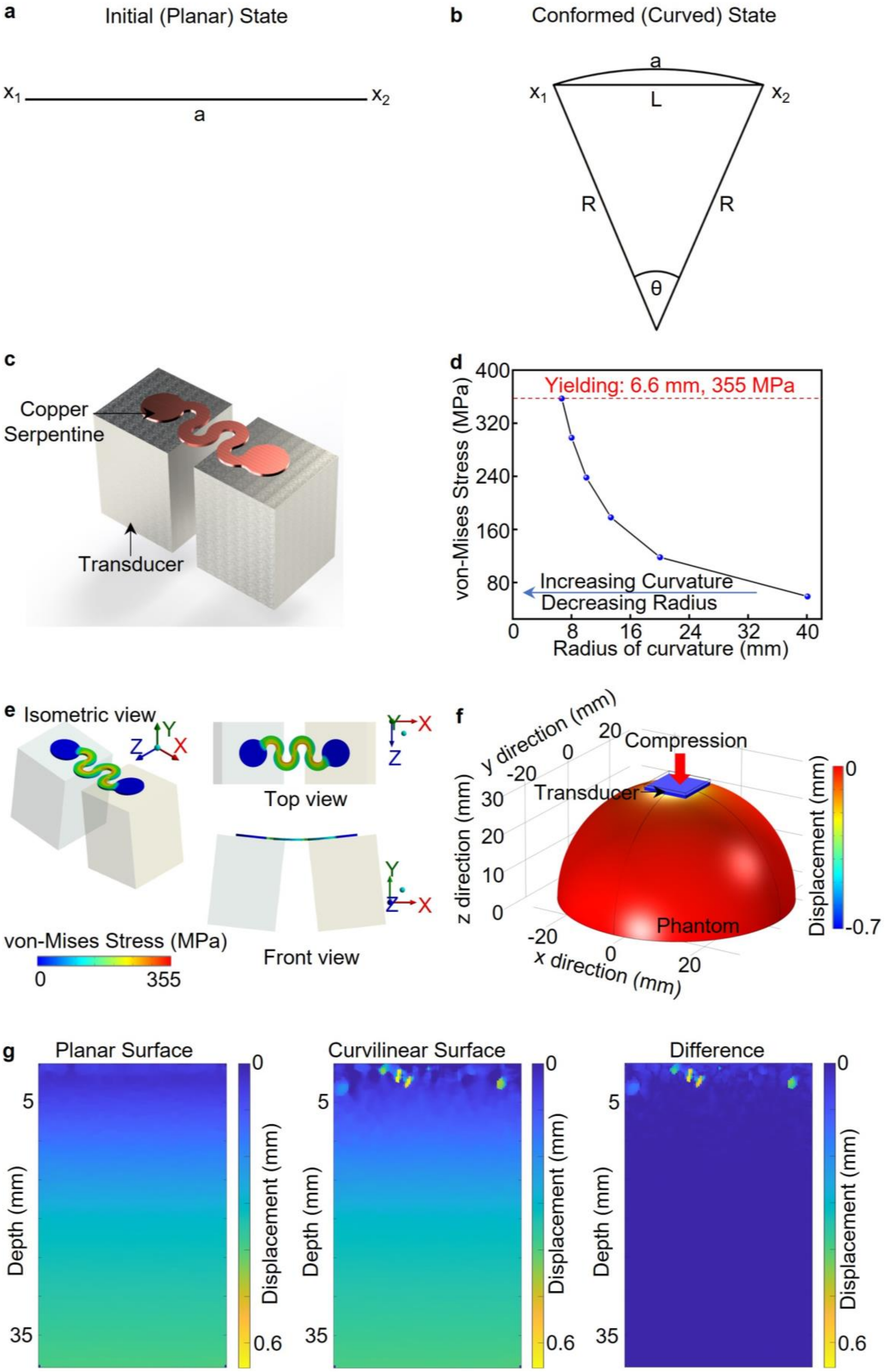

Supplementary Figure 14. Determination of the curvature range of the stretchable array. Schematics showing the pitch of transducer elements in different configurations, when they are (**a**) on a planer surface and (**b**) on a curved surface. (**c**) The schematics showing one unit of the array. (**d**) The relationship between the von-Mises stress and curvature radius. (**e**) Mechanical simulations showing the maximum curvature that the stretchable electrodes can conform to and the stress distribution in the electrodes. (**f**) COMSOL simulation of a 3D breast phantom model with different skin curvature. The compressor executes 0.7 mm uniaxial displacement to the breast phantom model. The post-compressive surface morphology has therefore been obtained. (**g**) Simulated displacement fields on a planar surface (left panel) and on a curvilinear surface (middle panel). Both fields are derived by using the time-delay profile on the planar surface. The right panel shows the discrepancy in the distribution of the two fields.

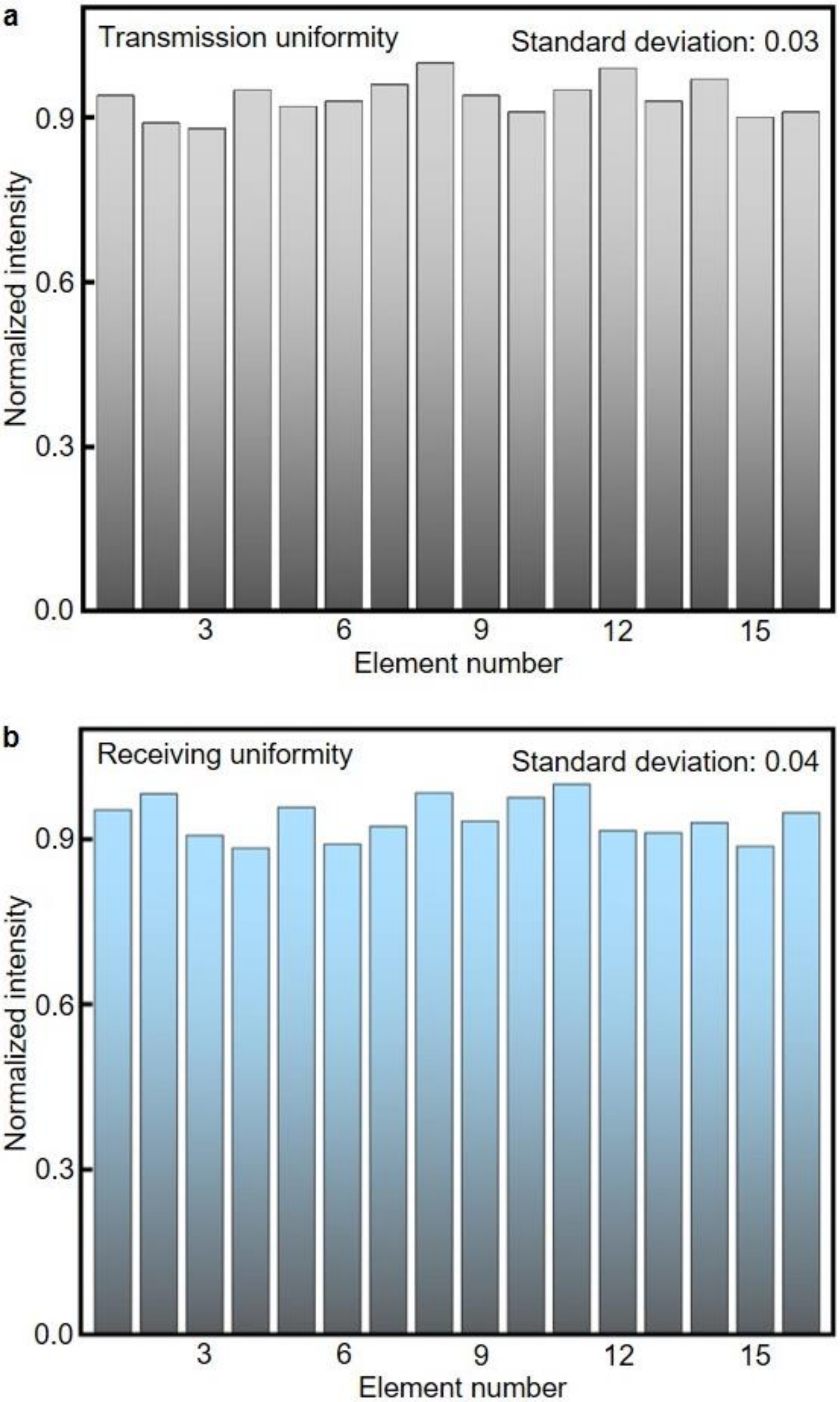

Supplementary Figure 15. Transmission and receiving uniformity. (**a**) Transmission uniformity with little standard deviation owns to the new device fabrication process (e.g., the transducer dicing). (**b**) Apodization tuning[109] greatly improves the receiving uniformity of the transducer array. The outstanding transmission and receiving uniformity significantly improve the beamforming quality to generate beamformed radiofrequency signals with high sonographic signal-to-noise ratios. The data intensity was normalized by the maximum intensity of the signal. Since the 3D testing is based on the integration of the 2D images from 16 linear arrays, one linear array is used as a representative example. The results of the other linear arrays are similar to this one.

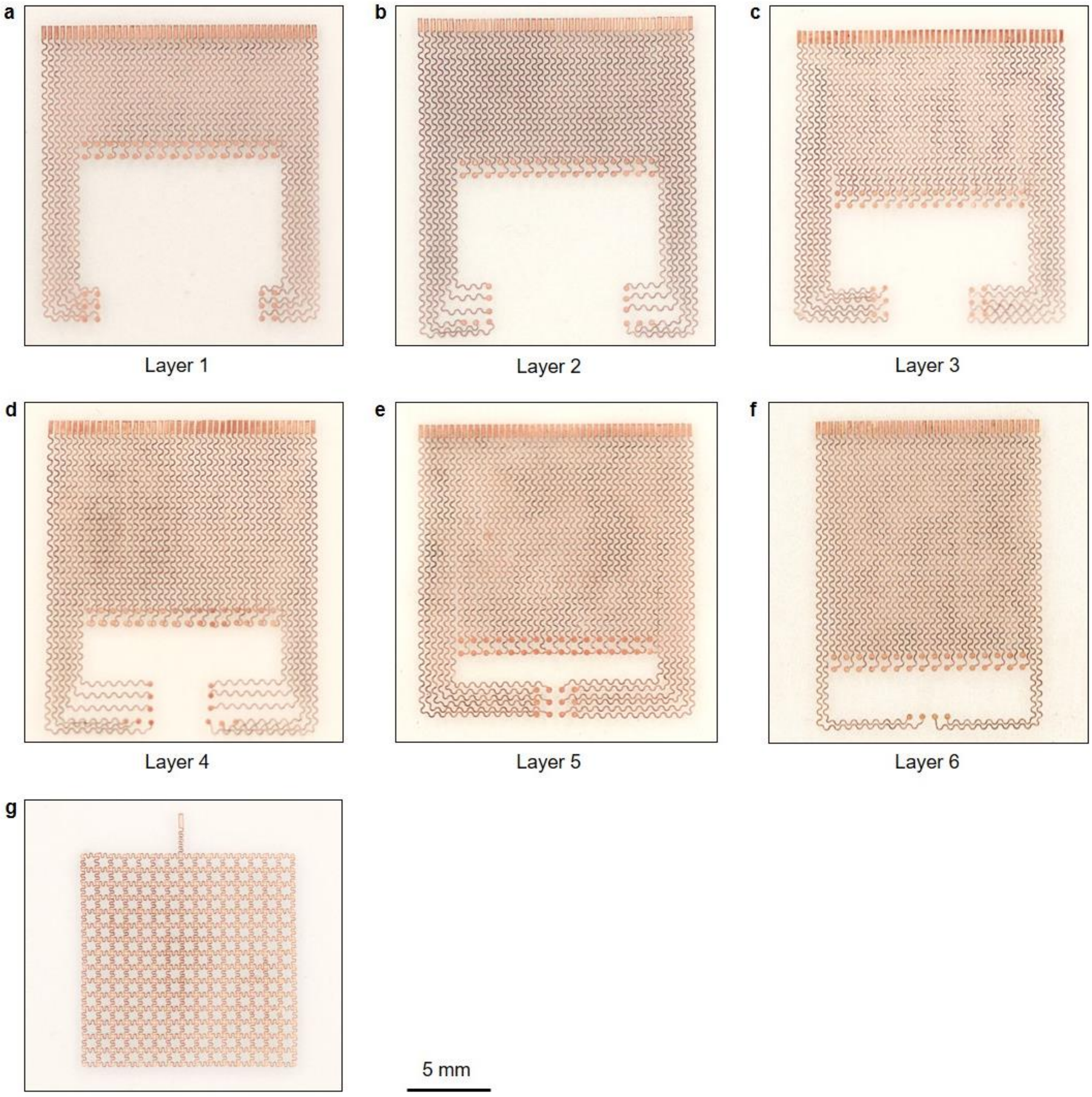

Layer 1 Layer 2 Layer 3

Layer 4 Layer 5 Layer 6

Bottom electrode

Supplementary Figure 16. Design and fabrication of the seven-layered electrodes. Optical images of (**a**)-(**f**) six layers of the activation electrodes, and (**g**) the bottom electrode as a common ground. This design permits individual activation with a particular time-delay profile for each element in the array while keeping the overall footprint small.

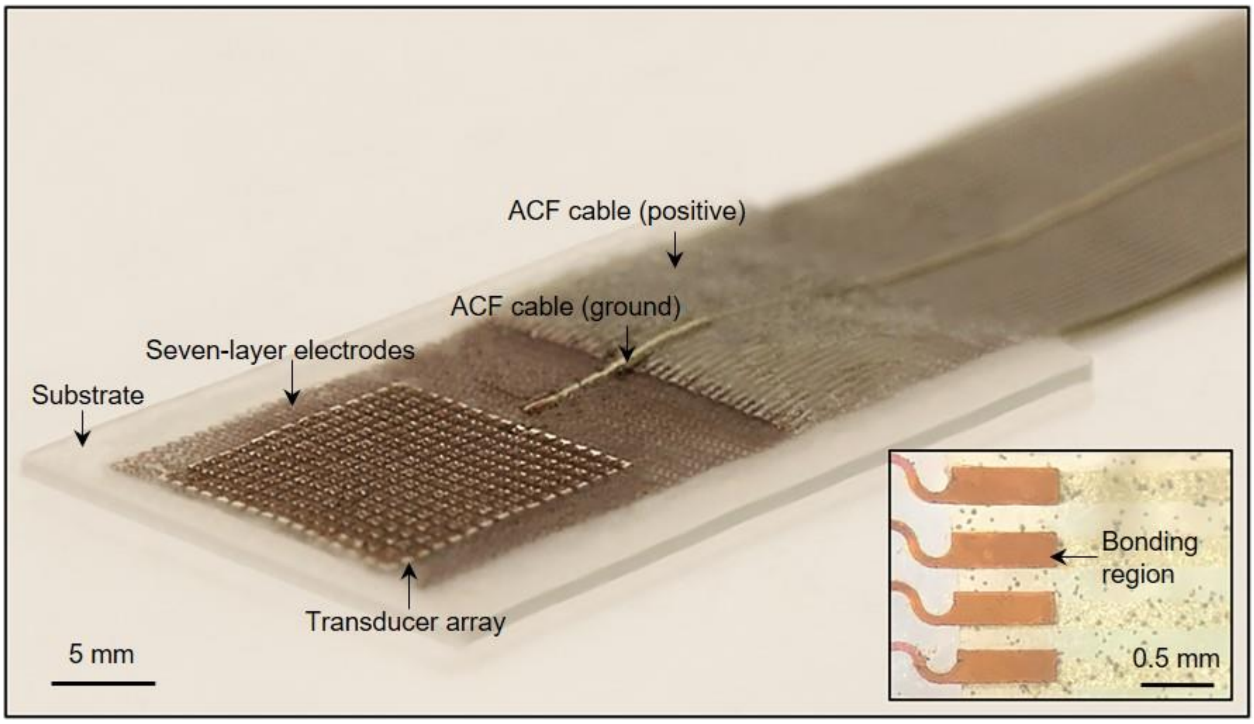

Supplementary Figure 17. Optical images of the stretchable ultrasonic array bonded with anisotropic conductive films. The anisotropic conductive film (ACF) can bond to the Cu interconnects as a flexible interface between the stretchable ultrasonic array and the external power supply and data acquisition system. The inset image is the bonding interface.

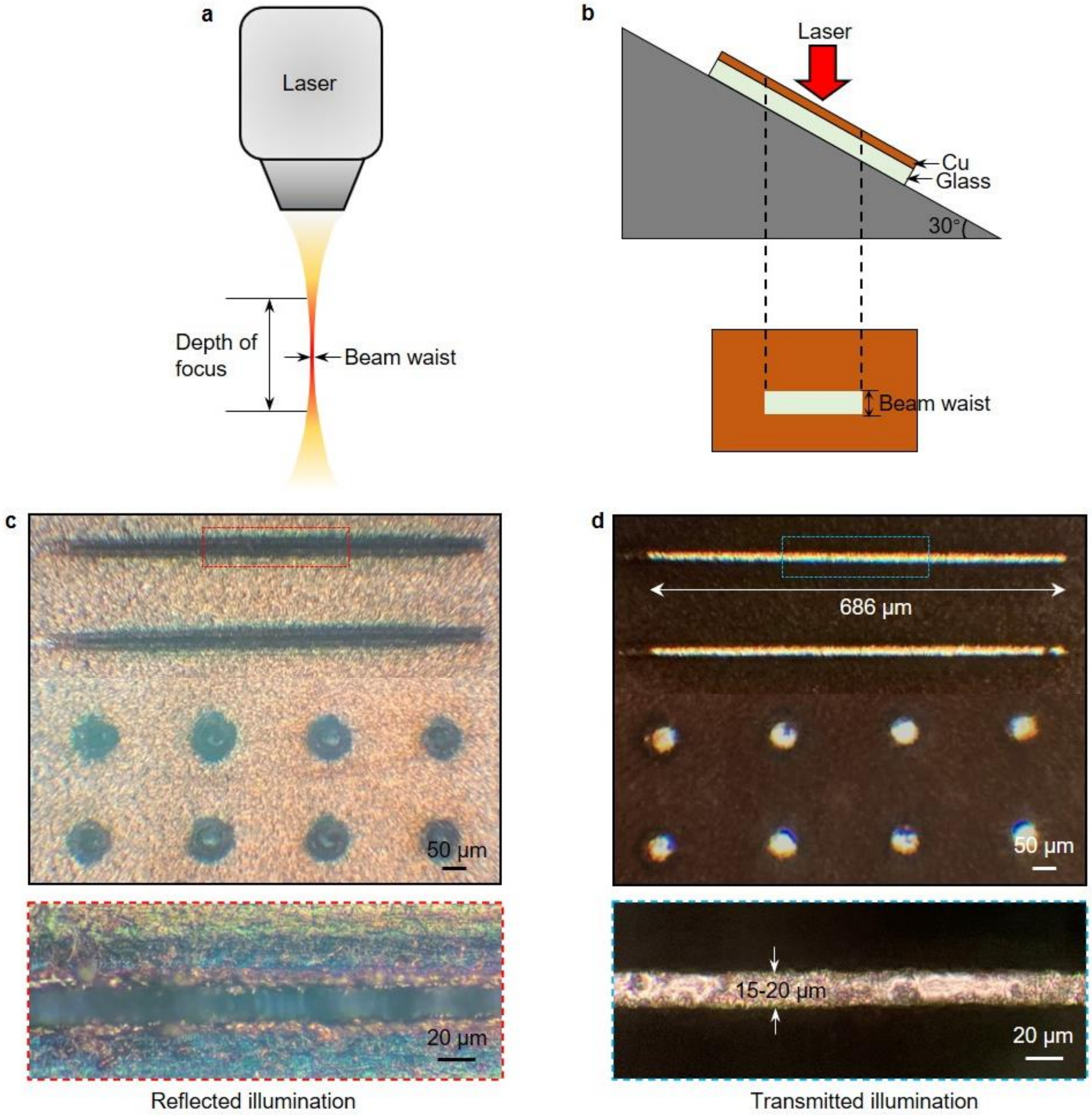

Supplementary Figure 18. Evaluation of the effective laser beam size and depth of focus. (**a**) A schematic figure of the laser beam, showing that the depth of focus and beam waist are two critical parameters for making the vertical interconnect accesses. (**b**) Schematics of the experiment setup. A Cu foil is put on a wedge with a 30° tilting angle and ablated by the laser to determine the depth of focus and the beam waist. (**c**) Reflected and (**d**) transmitted illumination of the ablation results. The 50 μm dot patterns are viewed as the reference to evaluate the beam waist and the depth of focus. The results show the beam waist is ~20 μm, providing accurate ablation with high spatial resolution. The depth of focus is ~686 μm that is long enough to make the vertical interconnect accesses of the top six-layered electrodes, whose total thickness is ~120 μm.

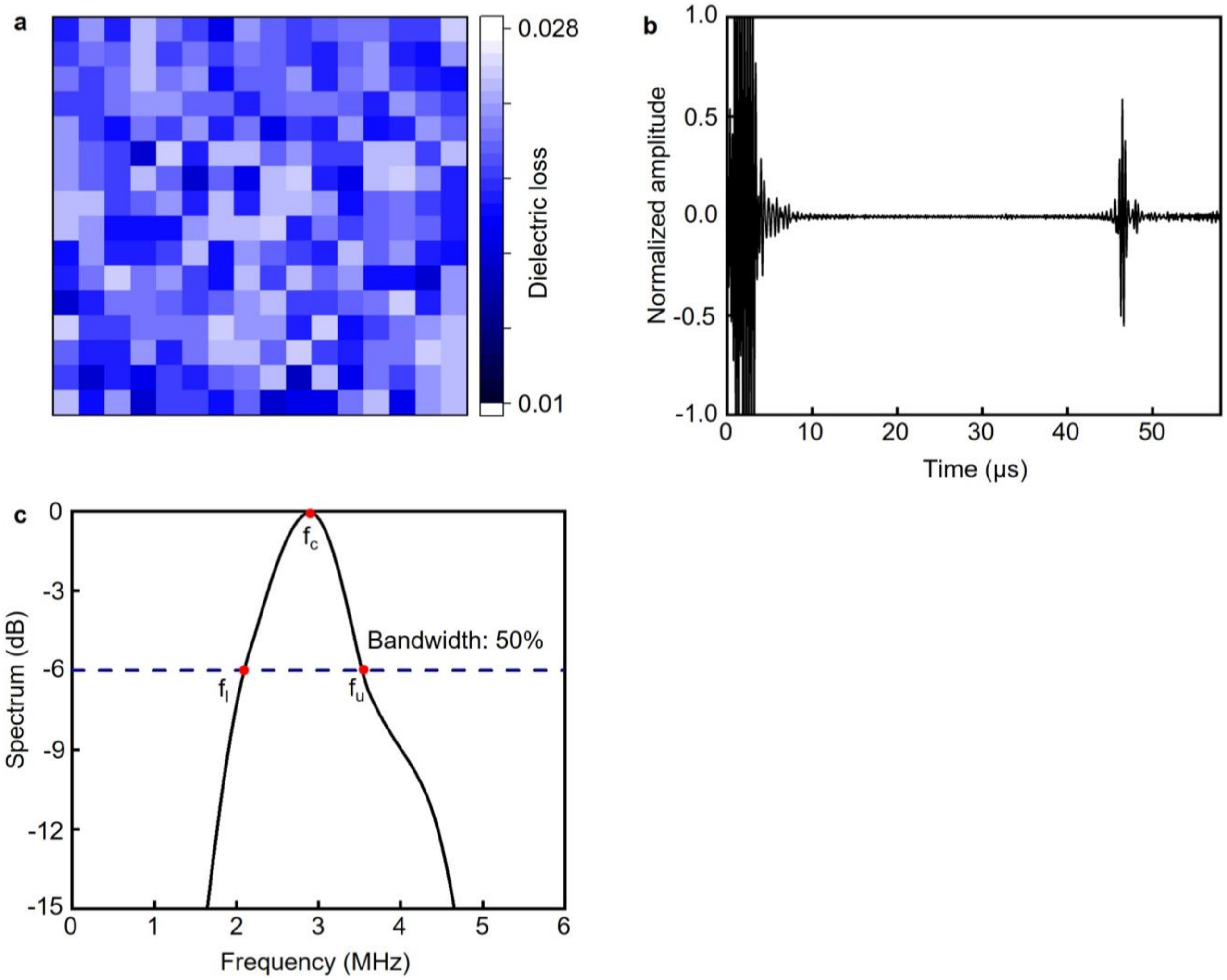

Supplementary Figure 19. Electromechanical characterizations of transducer array. (**a**) Dielectric loss of 16 × 16 array. The average of the dielectric loss is 0.022 and the standard deviation is 0.002. (**b**) Time- and (**c**) frequency-domain characterizations of the echo signals, showing the sensitivity and bandwidth of the transducer element. The data intensity was normalized by the maximum intensity of the initial pulse.

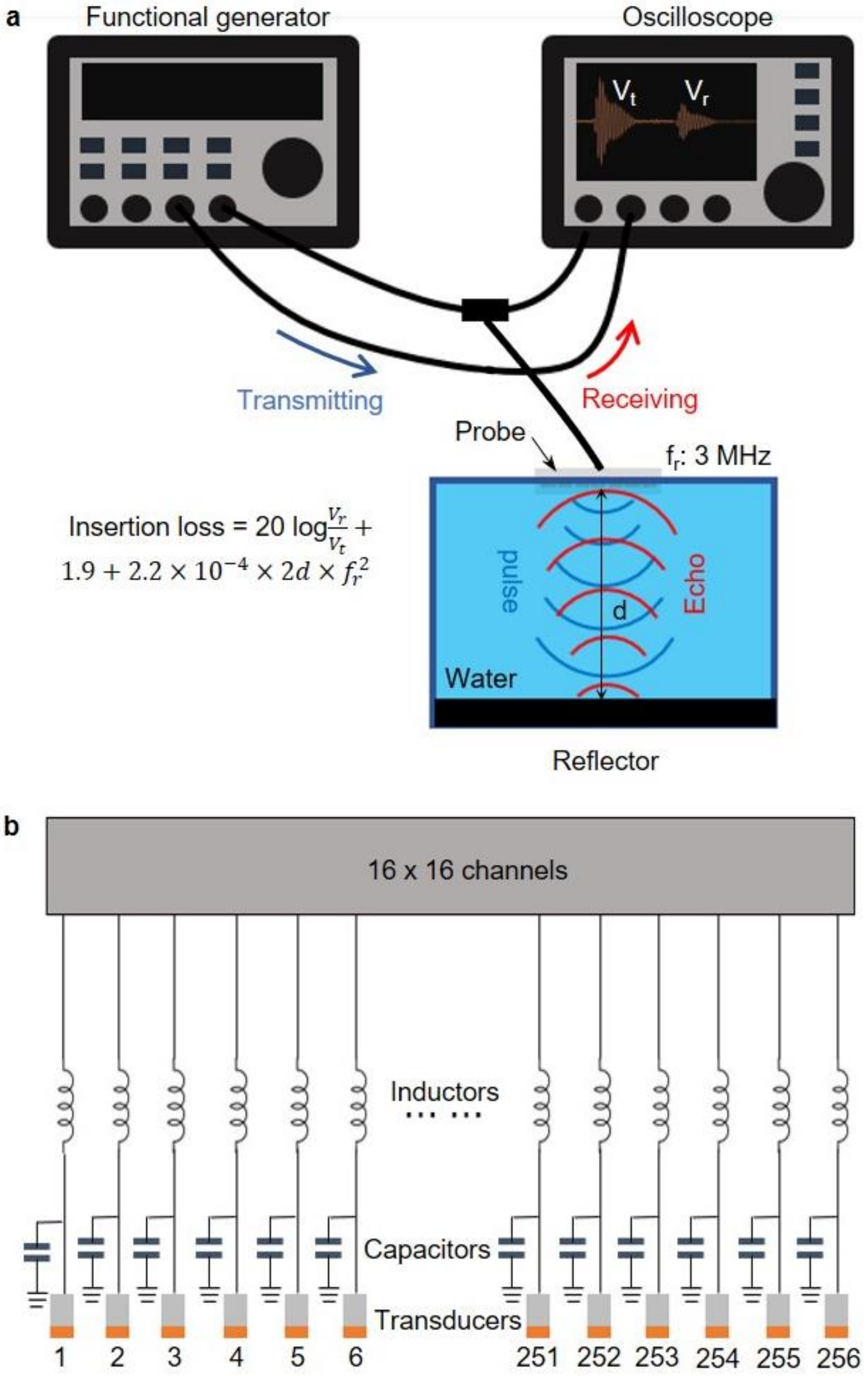

Supplementary Figure 20. The setup for characterizing the transducers' sonographic sensitivity and the corresponding design of the electrical matching circuit. (**a**) Insertion loss is used to quantify the sonographic sensitivity of the transducers and these two variables are inversely proportional to each other. (**b**) A schematic figure of the electrical matching circuit design. The matching circuit enhances the transmission efficiency of the electrical signals, resulting in a reduction of the power dissipation and an increase of the echoic intensity. The matching circuit reduces the insertion loss from 29.67 dB to 16.98 dB, significantly improving the sonographic sensitivity of the transducers.

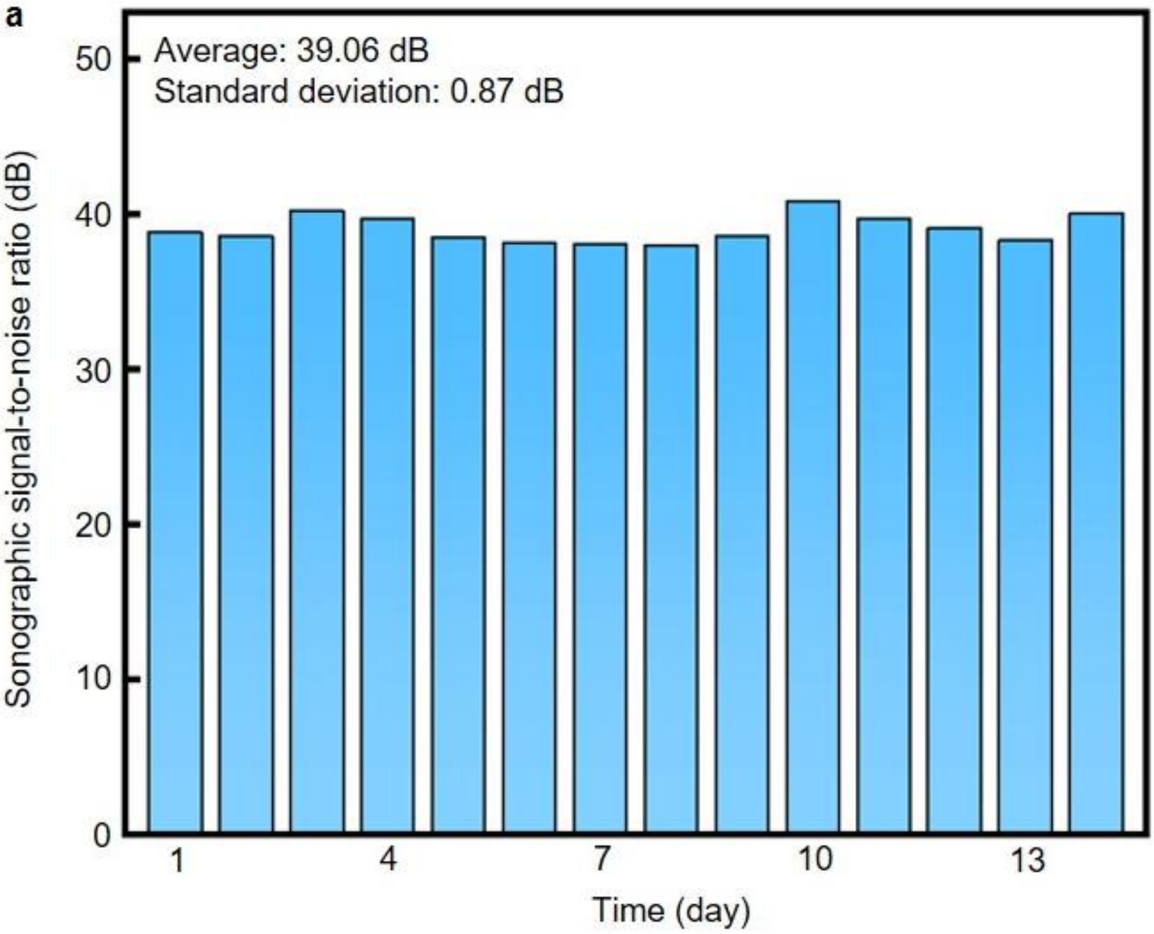

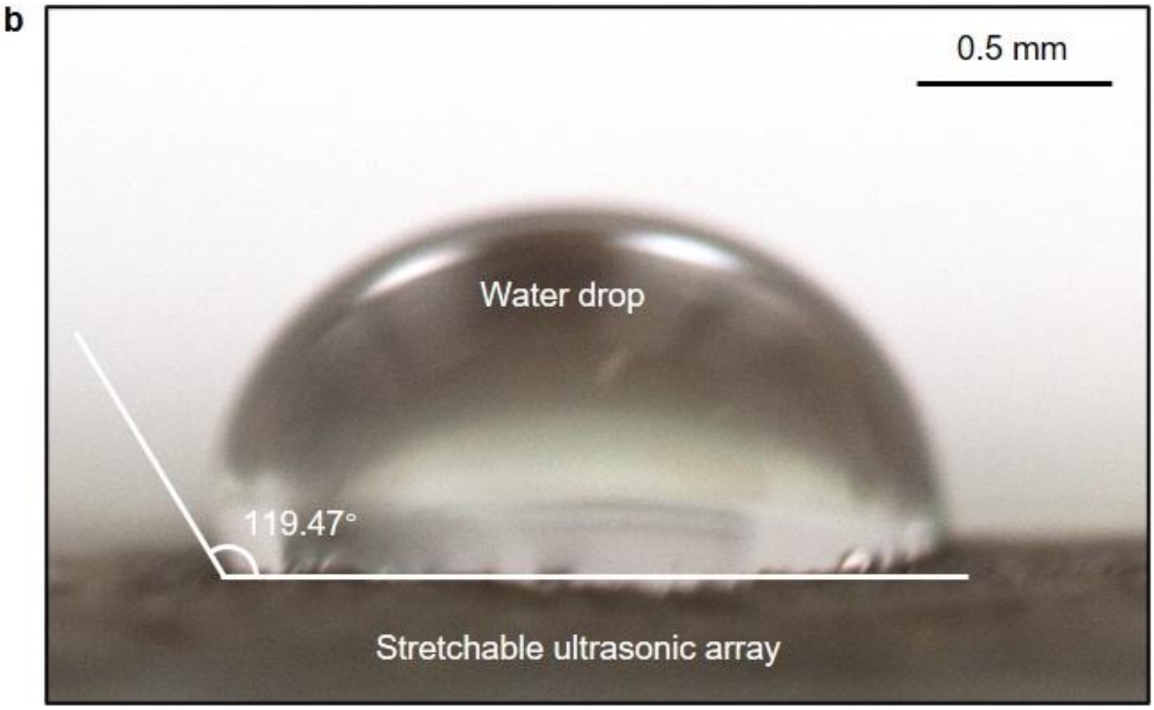

Supplementary Figure 21. Hydrophobicity characterization. (**a**) Sonographic signal-to-noise ratios of the stretchable ultrasonic array measured underwater for two weeks. (**b**) An optical image showing the contact angle of 119.47° of a water droplet on the stretchable ultrasonic array. The hydrophobicity of the encapsulating silicone elastomer makes the stretchable ultrasonic array sweat-proof.

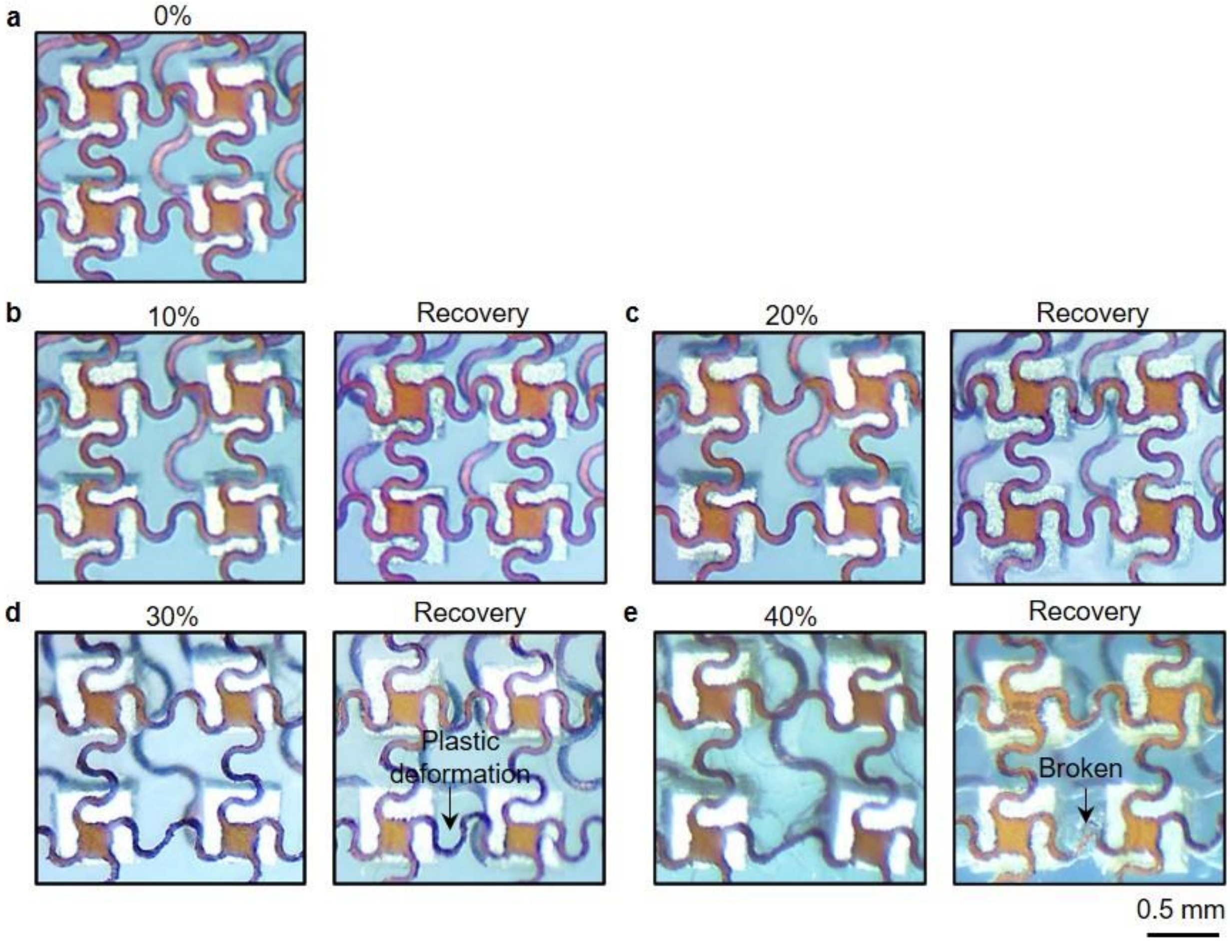

Supplementary Figure 22. Optical images of the stretchable ultrasonic array under stretchability tests. (**a**) The device in its original state under 0% strain. (**b**) The device under 10% biaxial tensile strain (left) and after releasing the strain (right). (**c**) The device under 20% biaxial tensile strain (left) and after releasing the strain (right). (**d**) The device under 30% biaxial tensile strain (left) and after releasing the strain (right). Plastic deformation of the interconnects starts to show up. The results reveal that the device can withstand biaxial strain up to 30% without irreversible deformations. (**e**) The device under 40% biaxial tensile strain (left) and after releasing the strain (right), where the fracture is identified (right). All panels share the same scale bar of 0.5 mm. The 800 μm pitch balances the elastographic image quality and the stretchability: finer pitch ensures a higher lateral resolution and fewer image artifacts caused by grating-lobes; a larger pitch allows larger stretchability and better conformability to the human body.

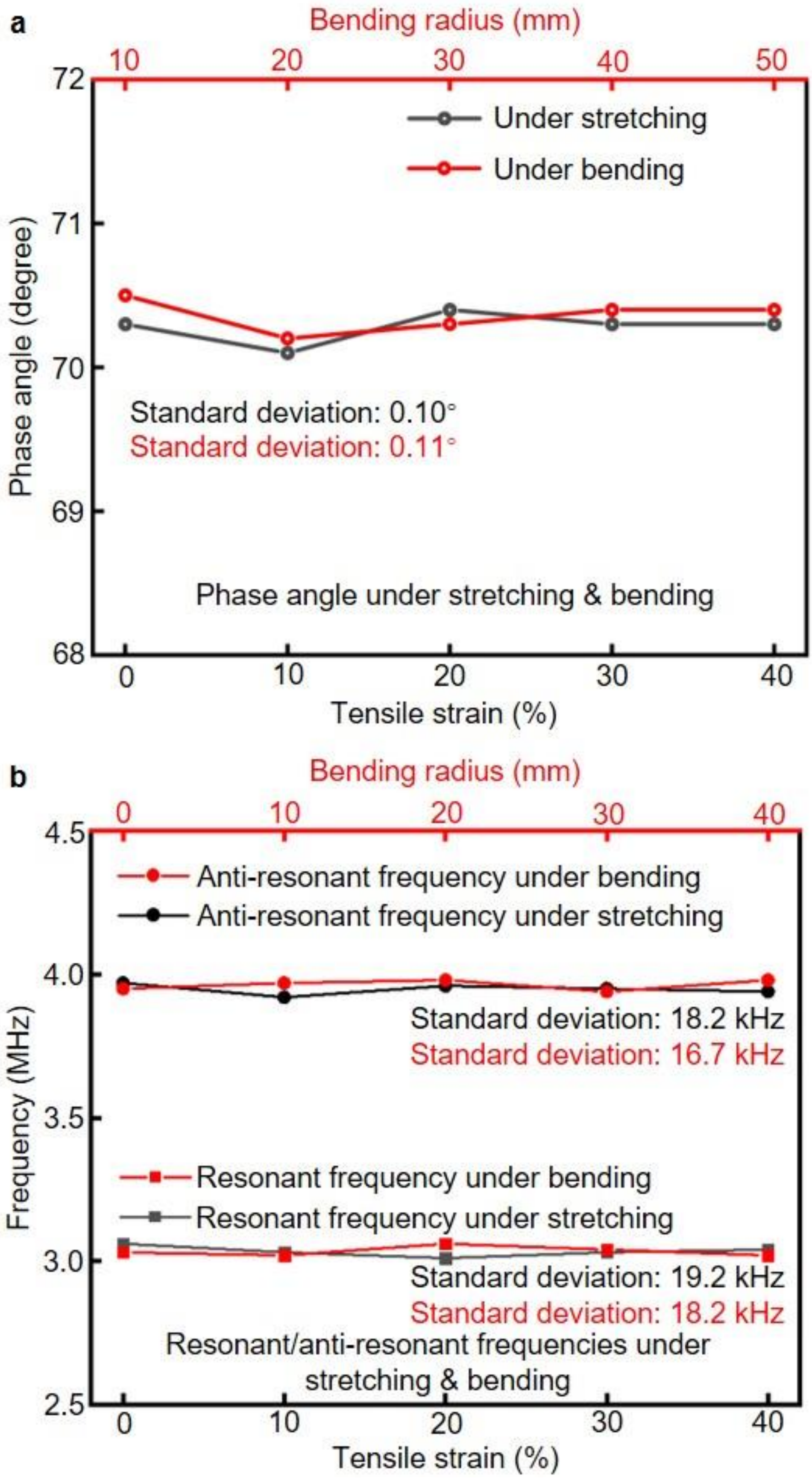

Supplementary Figure 23. Performance characterization of the transducers under deformation. (**a**) Phase angle and (**b**) resonant and anti-resonant frequencies of the transducers under stretching and bending. The small standard deviations (0.10°, 0.11° for phase angles; 19.2 kHz, 18.2 kHz for resonant frequencies; and 18.2 kHz, 16.7 kHz for anti-resonant frequencies) show the stable electromechanical coupling performance of the transducers under various modes of mechanical deformation.

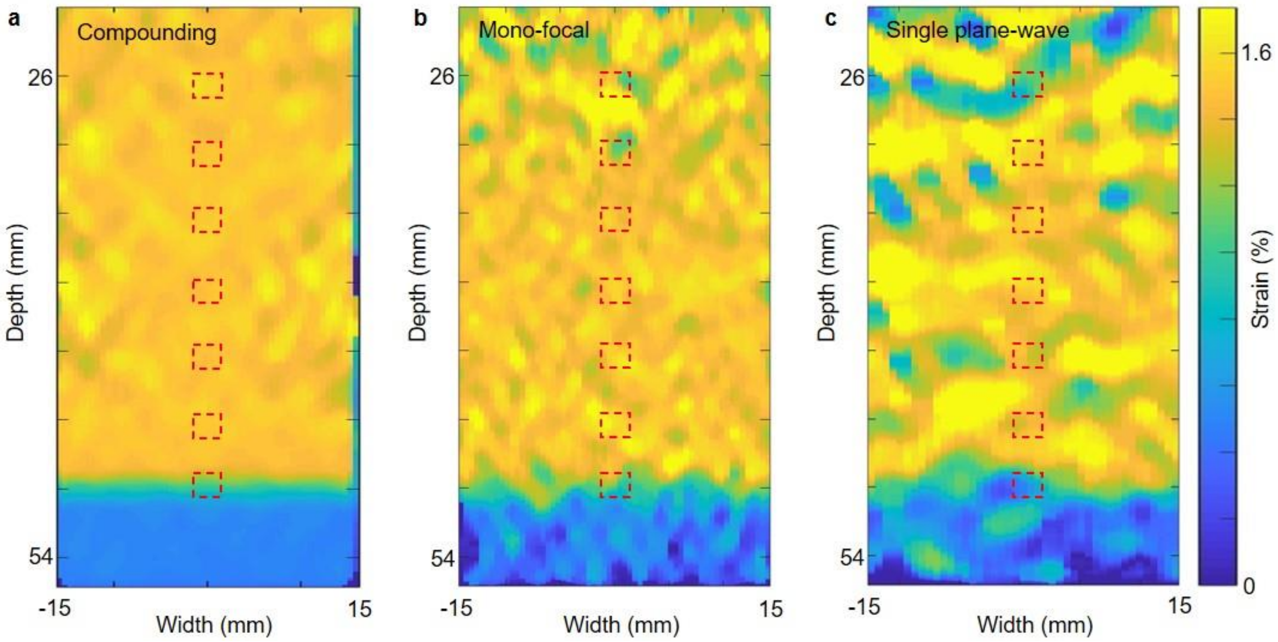

Supplementary Figure 24. Comparison of three different transmission modes. Strain distribution simulations using (**a**) coherent plane wave compounding, (**b**) mono-focus, (**c**) single plane-wave transmission modes. Red dashed boxes are the locations of choice for comparison. The single plane wave mode has a high frame rate and a short image reconstruction time since it does not need to steer multiple angles. The mono-focal mode can achieve a high image quality at the focal depth. The coherent plane-wave compounding mode provides images with the best SNR_e and CNR_e than the other two modes so it is used as the transmission mode for elastography imaging in this work.

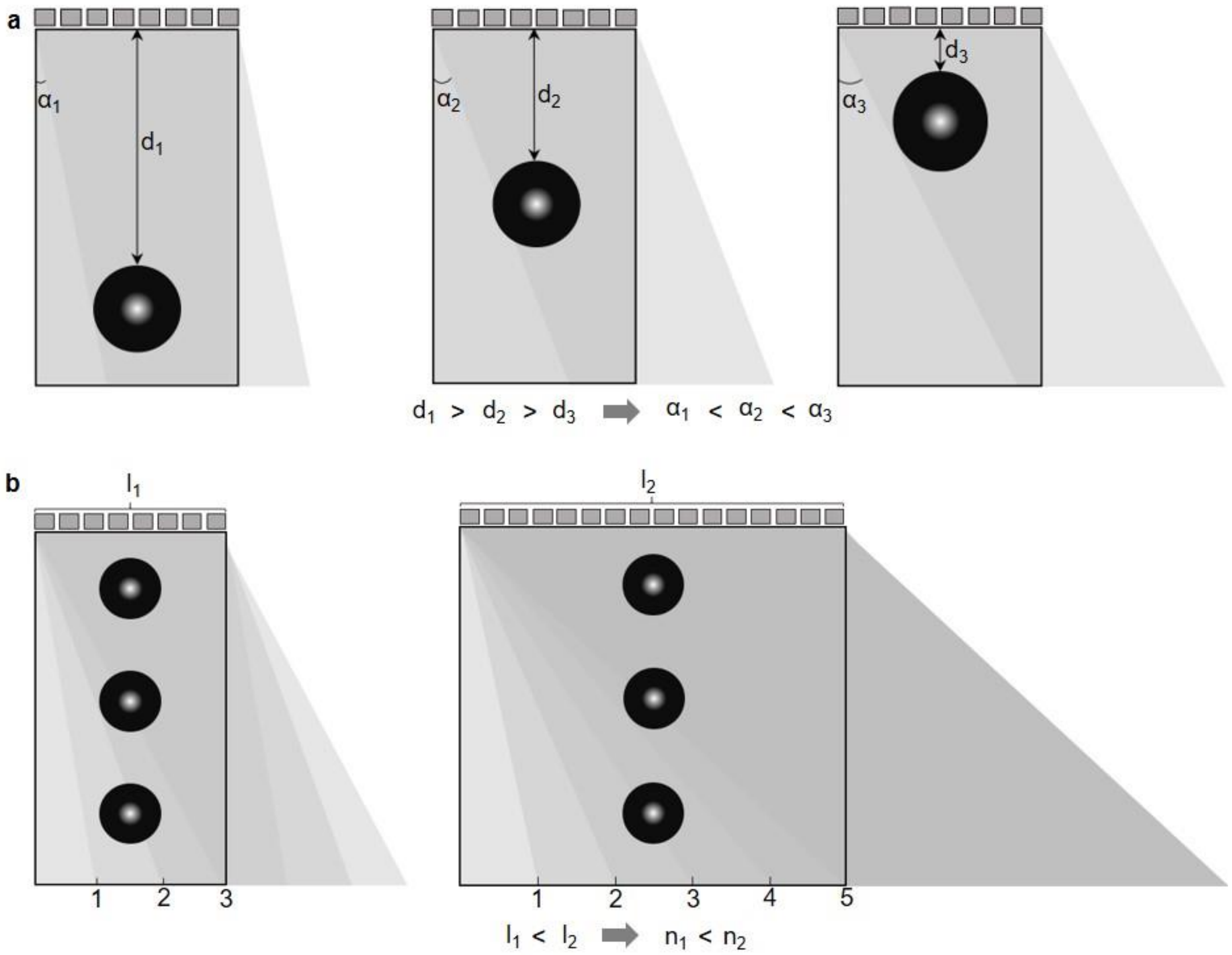

Supplementary Figure 25. Factors affecting the step size and the number of the compounding angle. (**a**) The step size mainly relies on the position of the target region. The deeper region needs a smaller step size, so the majority of scanned frames coherently overlap in this region. d: depth, α: step size. (**b**) The number of angles mainly relies on the aperture size of the transducer array. A larger aperture requires more angles, providing sufficient insonification by the plane waves at target regions to obtain effective synthetic focusing quality. In this work, the compounding mode with 19 steering angles in total significantly improves the SNR_e of the image. Without the steered angles, adding 19 slides of identical plane wave images together will increase the intensity of both useful signals and noises caused by the grating-lobes, even though random noises will cancel with each other. With different steering angles, these noises caused by grating-lobes are out of the overlapping area and will not add up. Therefore, the SNR_e of the final image will be enhanced. Since the compounding mode has the synthetic focusing effect at the entire region, the lateral and axial resolutions of the elastography images keep constant at different locations in the target region. l: aperture length; n: angle number.

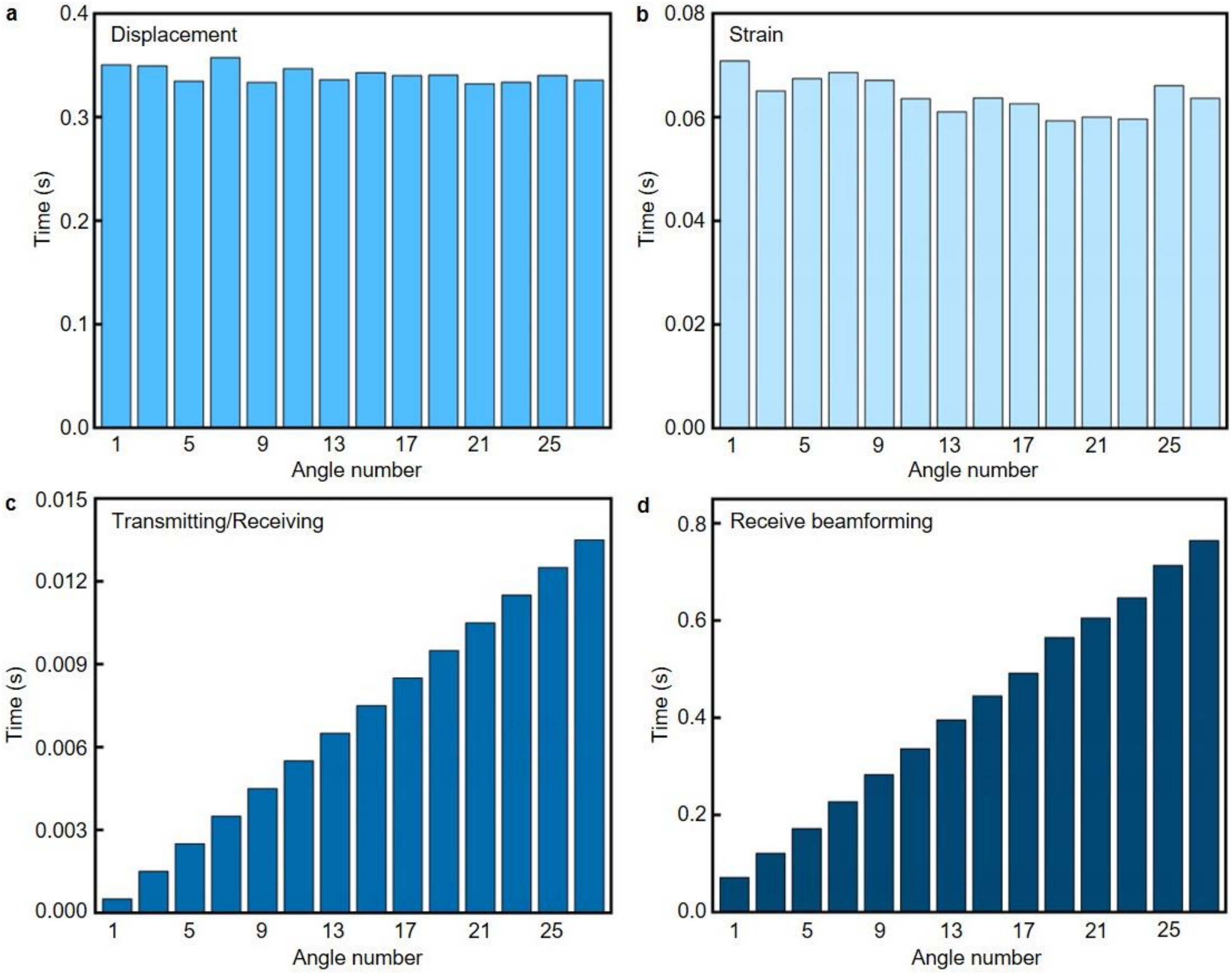

Supplementary Figure 26. Processing time for reconstructing images at different angle numbers. Time for (**a**) displacement calculation, (**b**) strain calculation, (**c**) transmitting/receiving, and (**d**) receive beamforming with different angle numbers. Time for calculating the displacement and strain keeps constant at different angle numbers but for the transmitting/receiving processes and receive beamforming is increasing linearly with the angle number. Specifically, time for receive beamforming dominates. Balancing the overall time budget and the gain in SNR_e at different numbers of steering angles, we use 19 angles for the compounding imaging in this work.

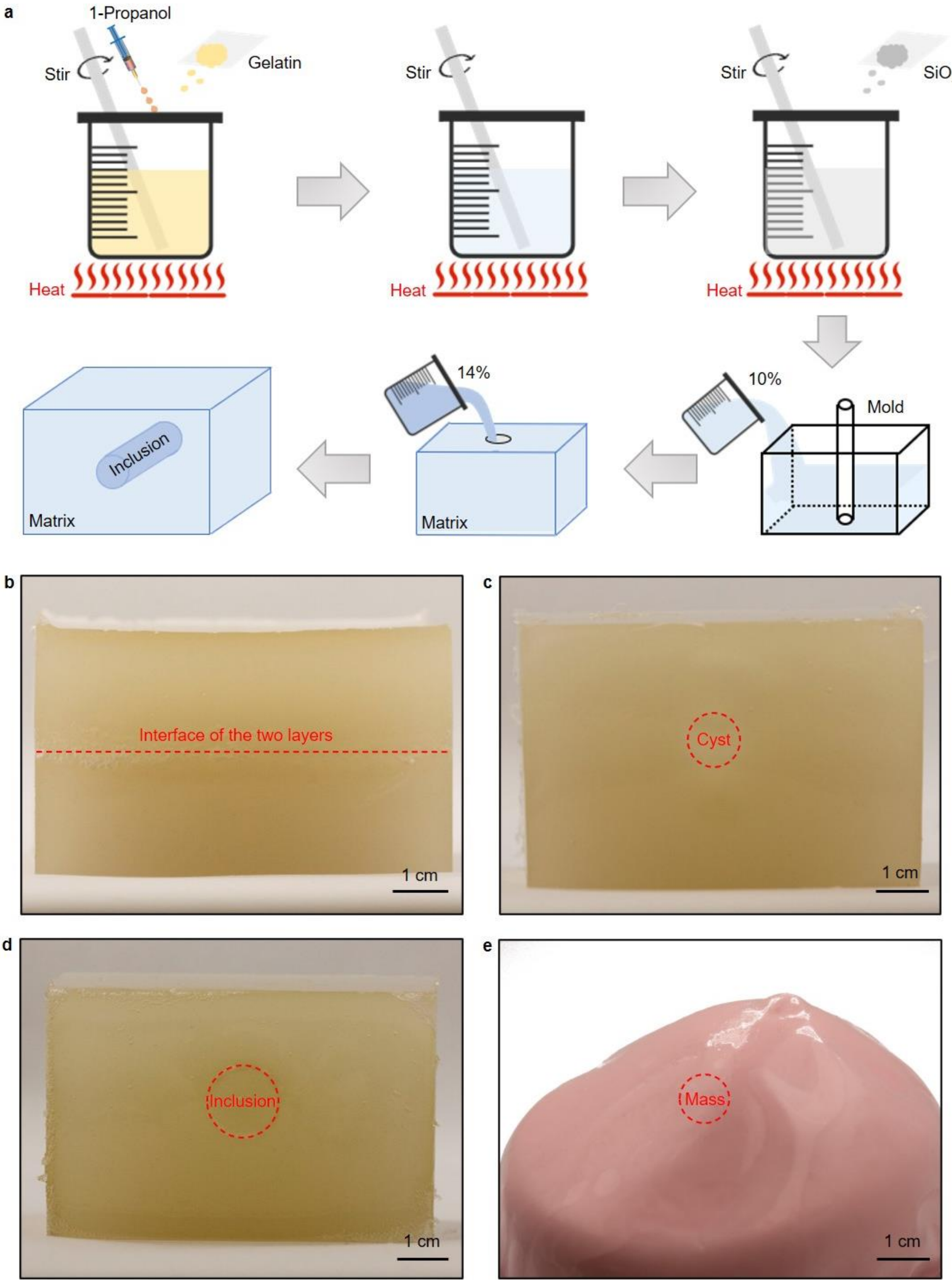

Supplementary Figure 27. Fabrication processes and optical images of tissue-mimic phantoms. (**a**) The tissue-mimic phantoms are made of gelatin and silicon dioxide particles. Optical images of (**b**) a bilayer phantom, (**c**) a phantom with cyst (fluid inside), (**d**) a phantom with inclusion (solid inside), (**e**) a commercial breast phantom with a mass inside (CIRS Model 059), corresponding to 1D, 2D, 2D, and 3D biological tissue elasticity models, respectively.

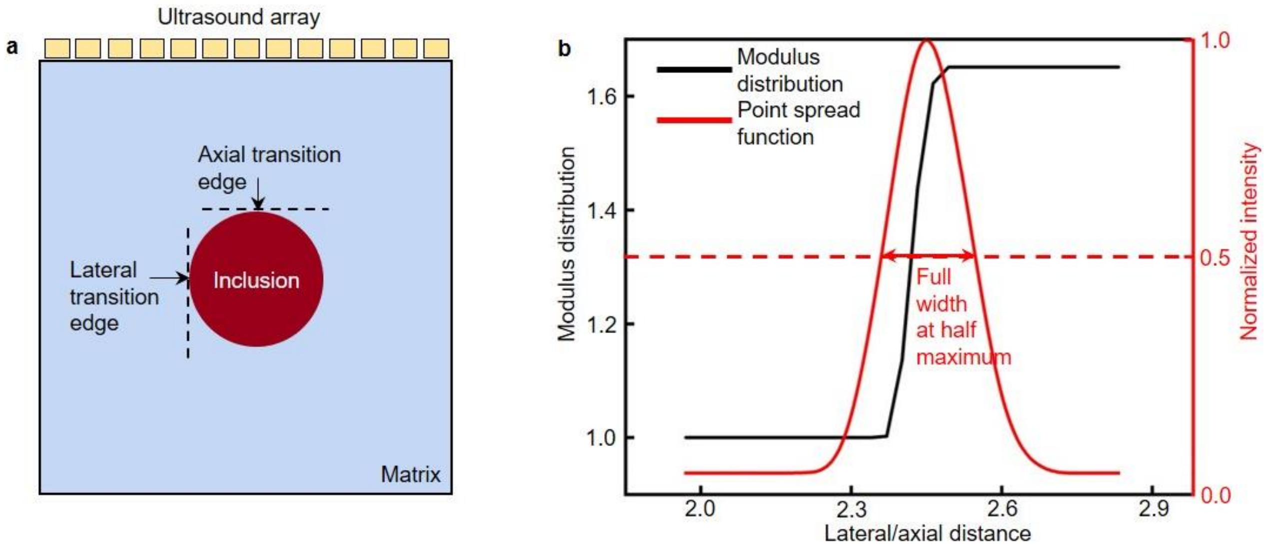

Supplementary Figure 28. Characterizing the elastographic spatial resolutions. Schematic plots of (**a**) the experiment setup and (**b**) curves of modulus distribution and the corresponding point spread function. The intensity of the curve was normalized by its maximum intensity. The detailed calculation process is in Materials and Methods. The full widths at half maximum of the point spread functions are defined as the lateral and axial resolutions.

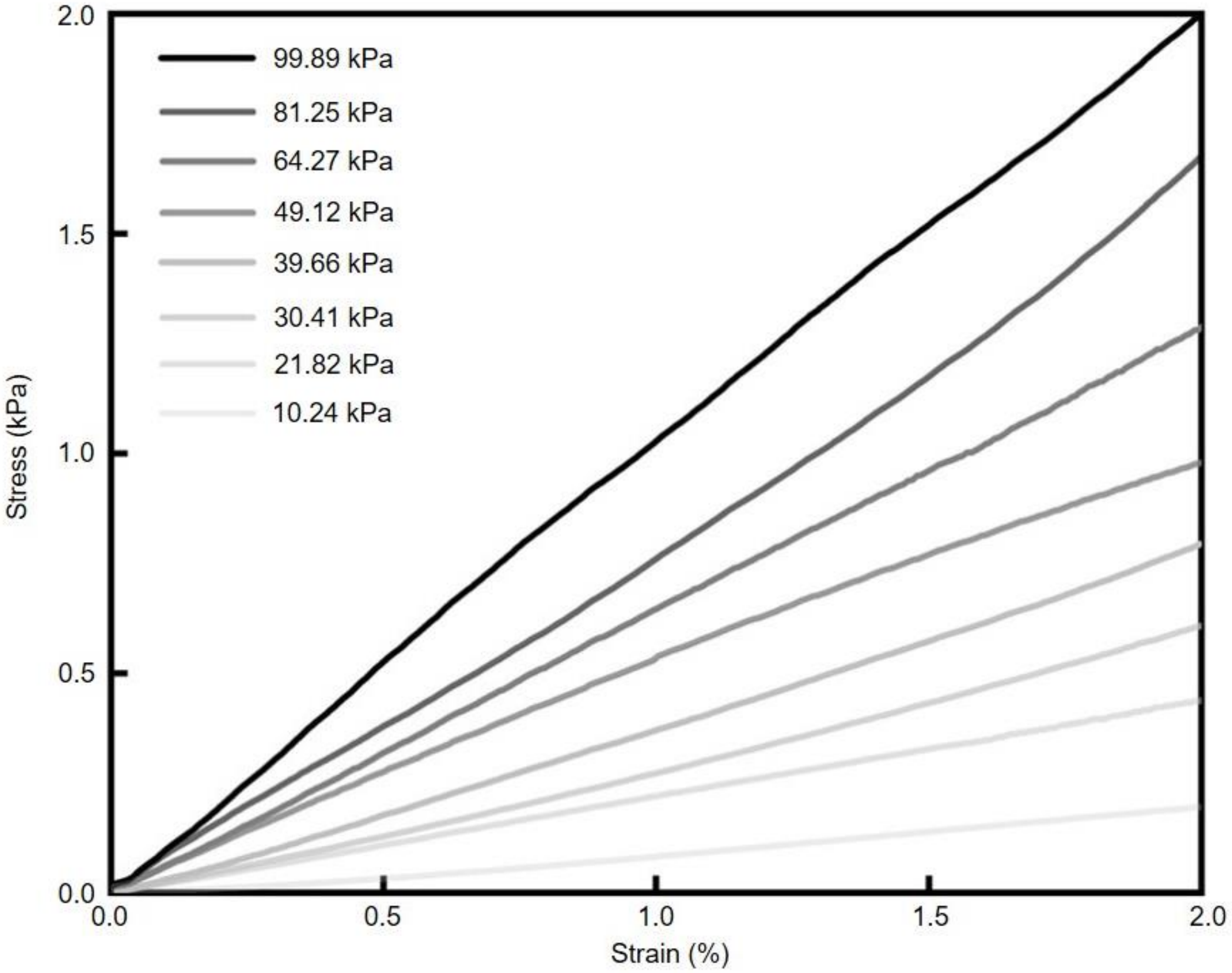

Supplementary Figure 29. Stress-strain plots of tissue-mimic gelatin phantoms in quasi-static strain rate regimes. We focus on the first 2% strain since within this range the phantom has a linear stress-strain behaviour. Young’s moduli are yielded by calculating the slope of the curves. Non-linear behaviour shows up when the strain is larger. That non-linear part in the stress-strain curve will not be used for Young’s modulus calculation.

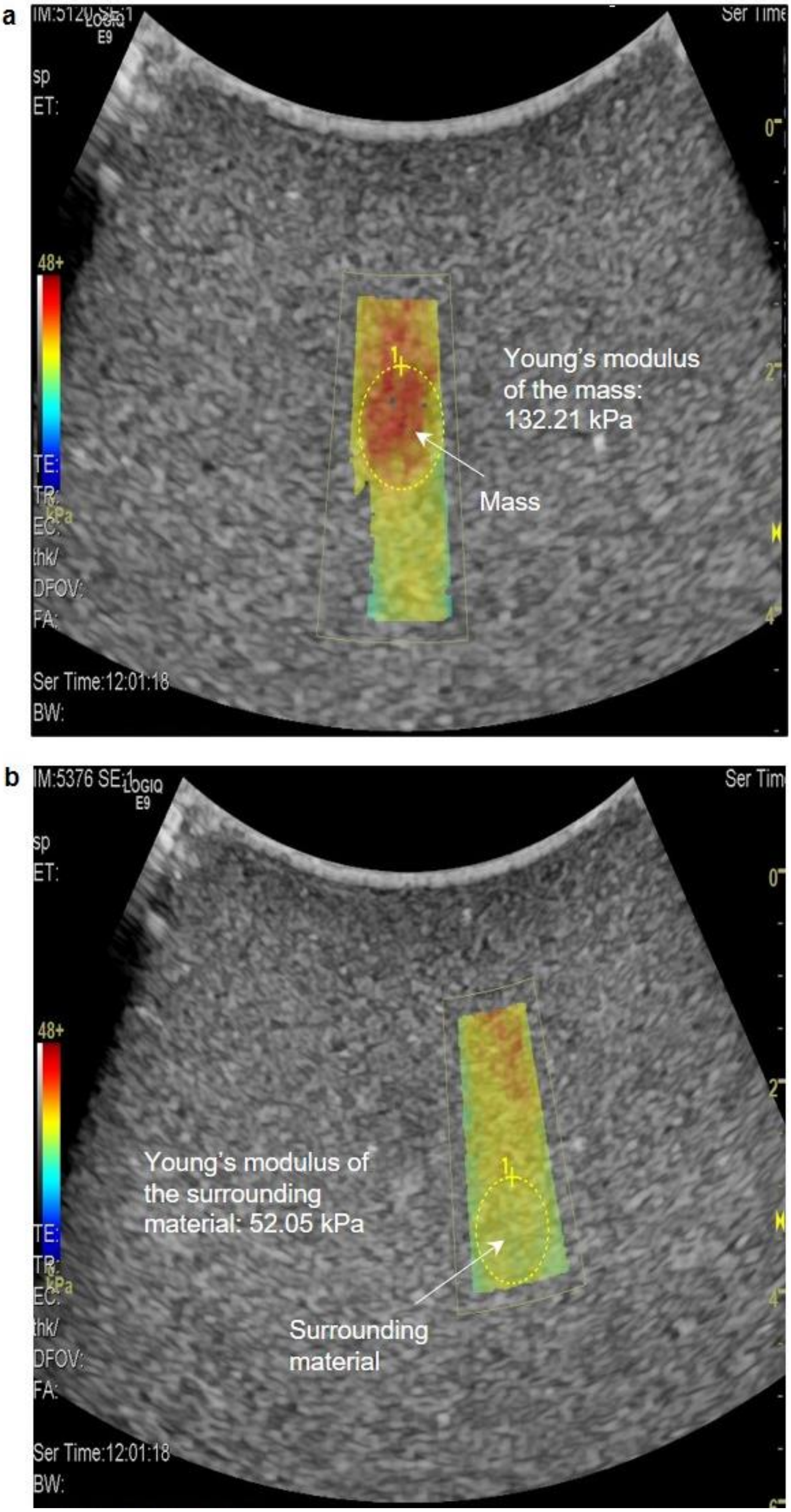

Supplementary Figure 30. Modulus validation of a commercial breast phantom. We validate the moduli of (**a**) the mass and (**b**) the surrounding material by a medical shear-wave ultrasound system (GE Logiq E9 Ultrasound Machine). The Young's modulus equals to three times the shear modulus in soft tissues, which yields 132.21 kPa and 52.05 kPa of Young's moduli of the mass and the surrounding material, respectively.

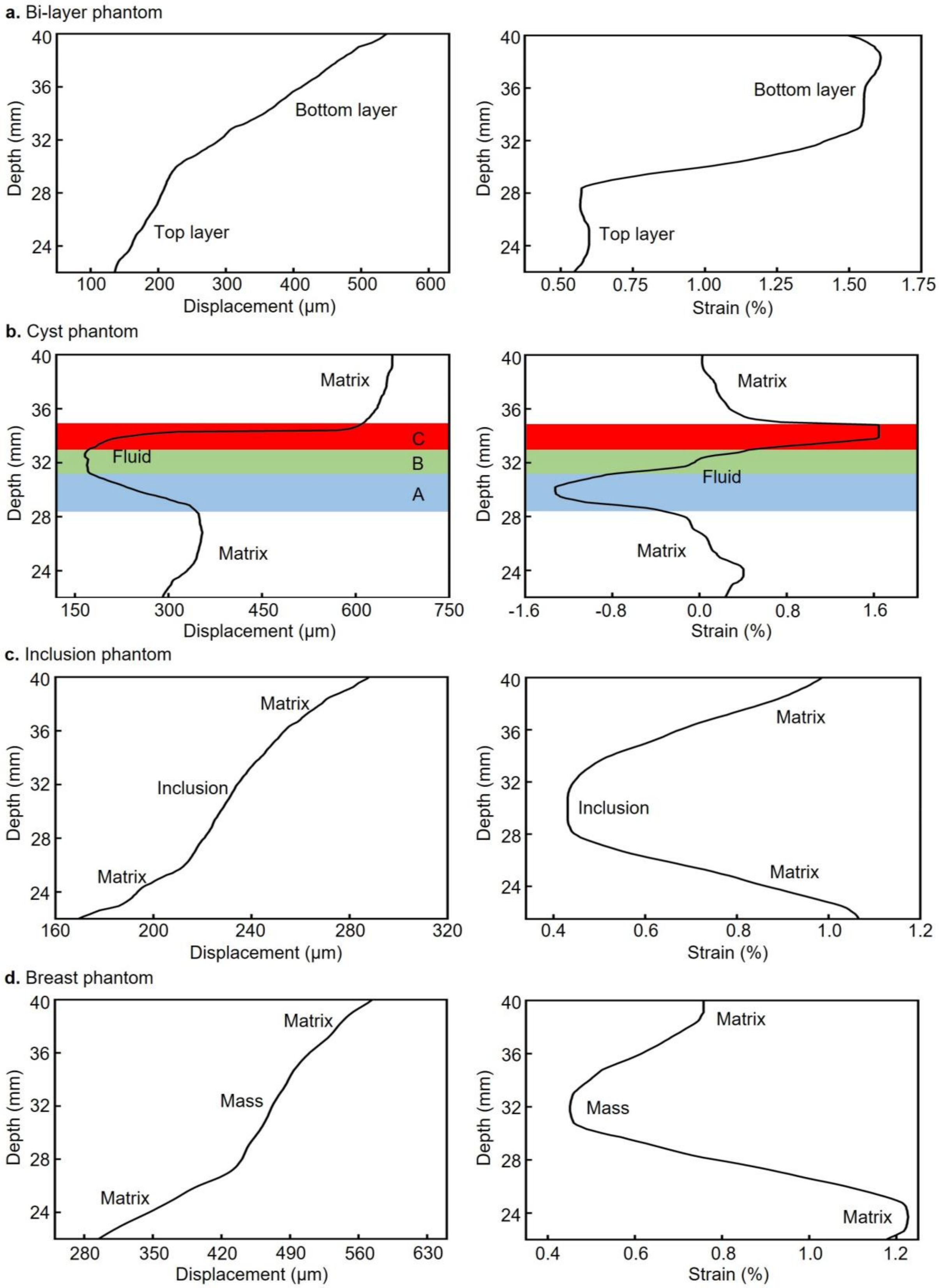

Supplementary Figure 31. Displacement and strain curves at the central lines of different phantoms. The displacement (left column) and strain curves (right column) of (**a**) a bi-layer phantom, (**b**) a cyst phantom, (**c**) an inclusion phantom, and (**d**) a breast phantom. The slope of the displacement curve of each component generally does not vary with the thickness, indicating the uniform Young's modulus of each component. The least-squares strain estimator with a piecewise linear curve fitting transforms the displacement to the strain. These curves at the central lines clearly show the difference in displacement and strain of each component in the phantoms. Particularly, the blue-green-red regions in the cyst phantom is a unique artifact in cysts. The cyst region is devoid of echoes and mere random noises are detected, causing the displacements to be very small. The section where the large displacement transits to the small displacement produces a large negative strain due to the slope change in the displacement curve (“A” region, blue artifacts). The small displacement generates close to zero strain (“B” region, green artifacts). And the transition section where the displacement rises from small to large yields large positive strain (“C” region, red artifacts). Analysis and discussions about regions “A” and “C” are in Supplementary Fig. 32.

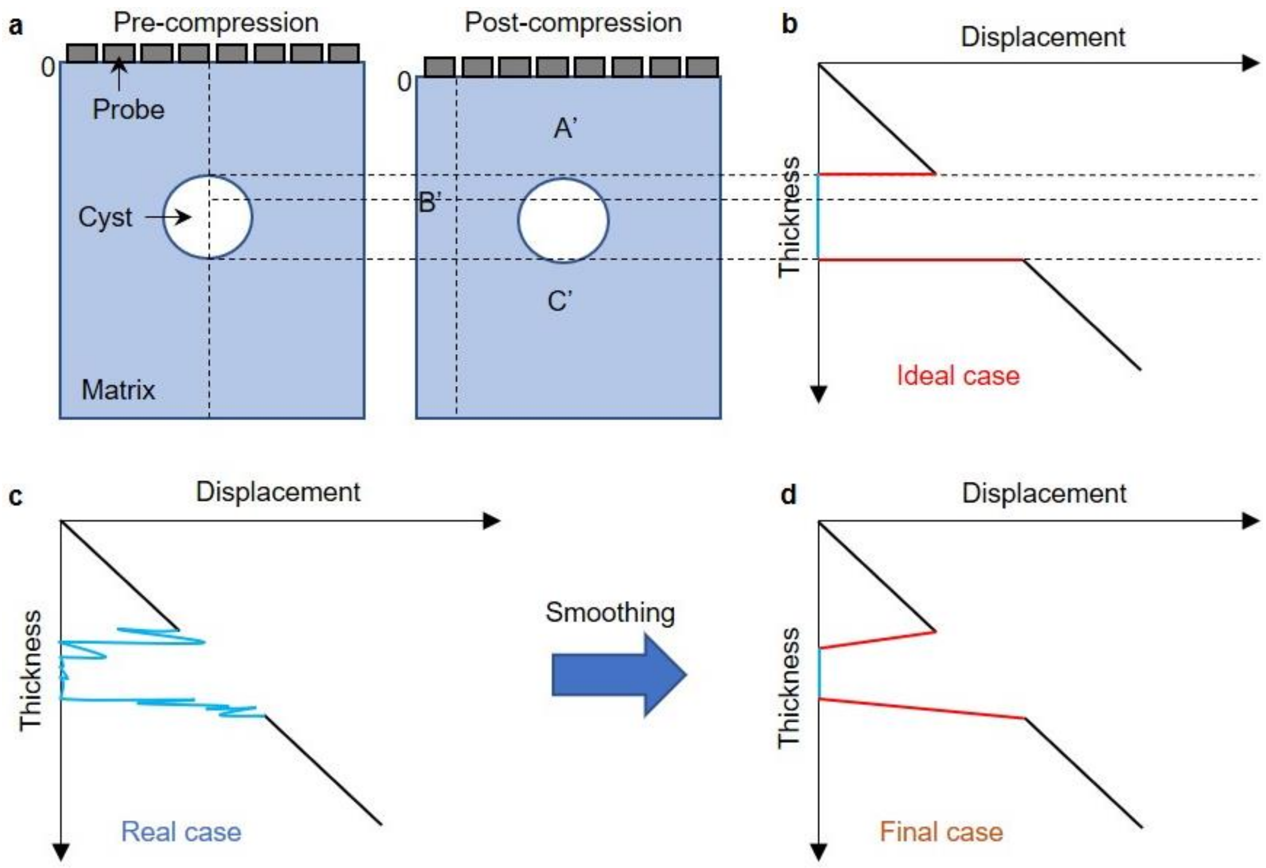

Supplementary Figure 32. Schematic plots showing the mechanism of generating the displacement curve in the cyst phantom. (**a**) When a cyst phantom undergoes a mild compression, (**b**) the displacements of the transition between the matrix and the cyst ideally should go straight down and up (two red lines). The cyan line in (**b**) represents the displacement of the cyst region. (**c**) In the real case, since there are no echoes in the cyst region, the electrical noises from radiofrequency lines cause the displacement curve in this region to be very noisy. (**d**) After smoothing, the curves with gradients (two red lines) have been yielded to connect the displacements between the matrix and the cyst.

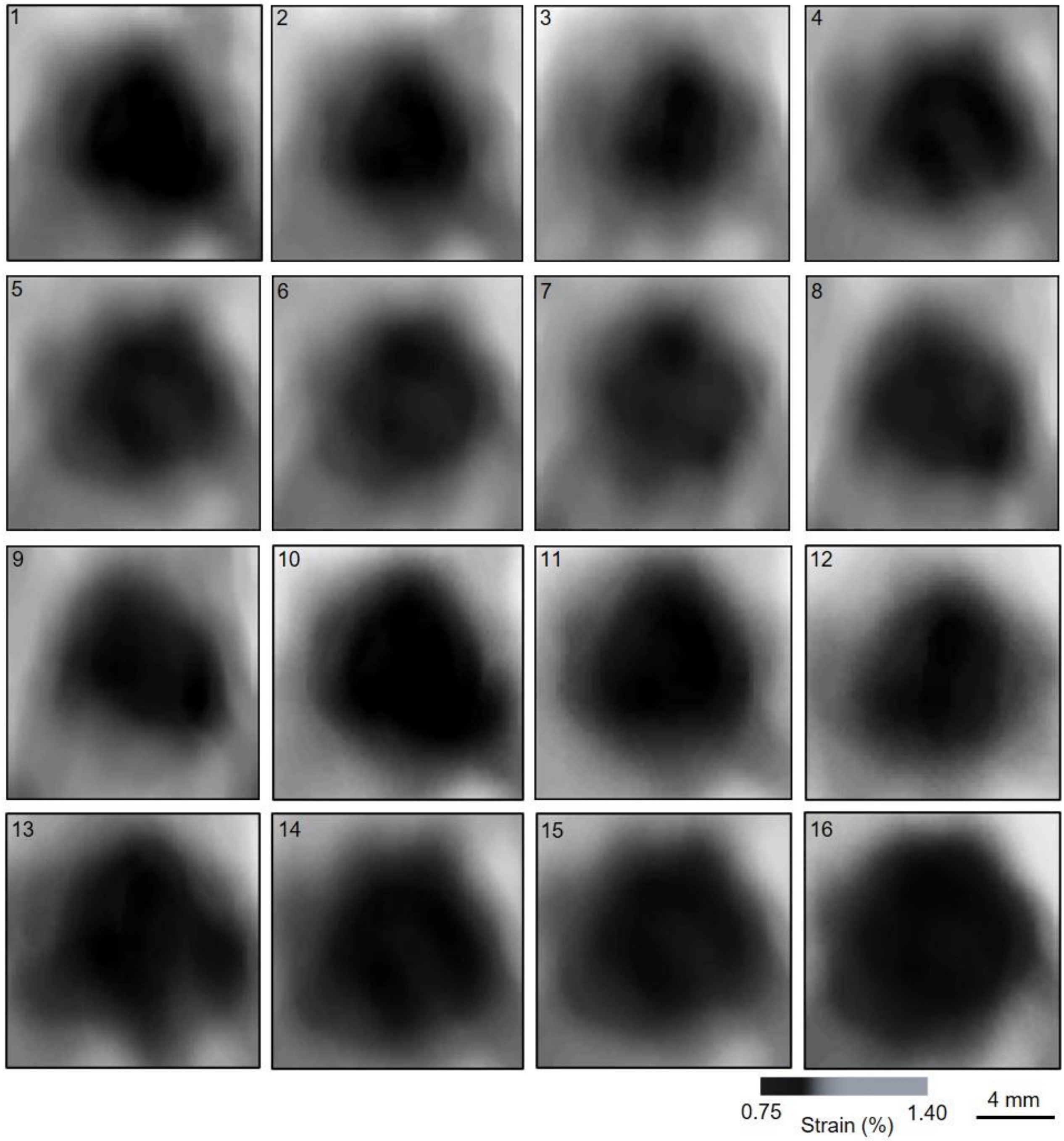

Supplementary Figure 33. 16 slices of 2D strain images of the inclusion phantom by the stretchable ultrasonic array. Each slice of 2D strain image is generated by one 1×16 linear array in the stretchable ultrasonic array. 16 strain images with similar strain values and distribution demonstrate the stable and reliable performance of the stretchable ultrasonic array. These 2D images are used to reconstruct the 3D image. These figures share the same color bar and scale bar.

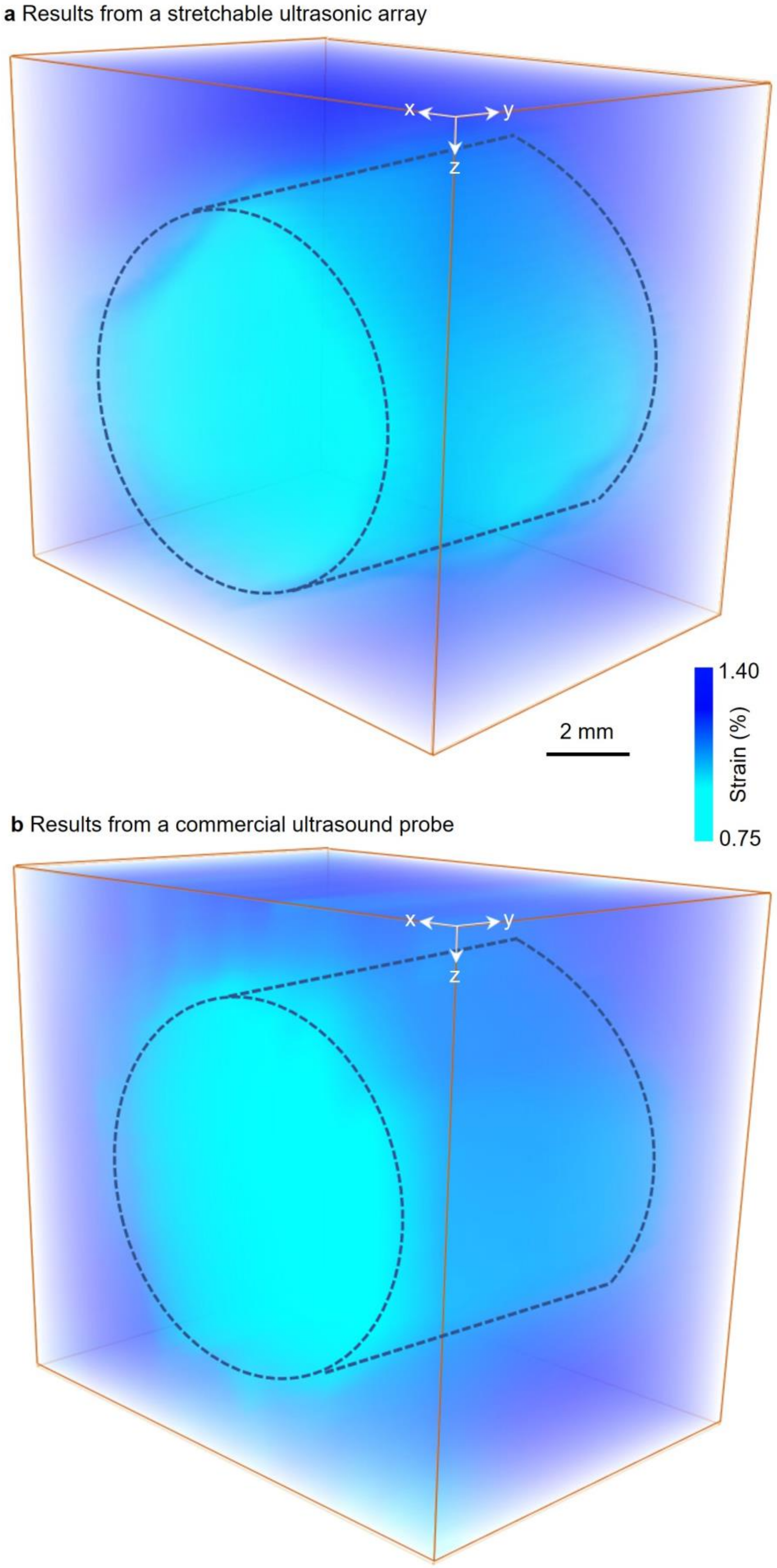

Supplementary Figure 34. 3D strain images of an inclusion phantom by the stretchable and commercial ultrasonic probes. The 3D strain images tested by (**a**) the stretchable ultrasonic array and (**b**) a commercial ultrasound probe show high correspondence to each other in size, geometry, and strain distribution of the inclusion phantom. Both figures share the same color bar and scale bar.

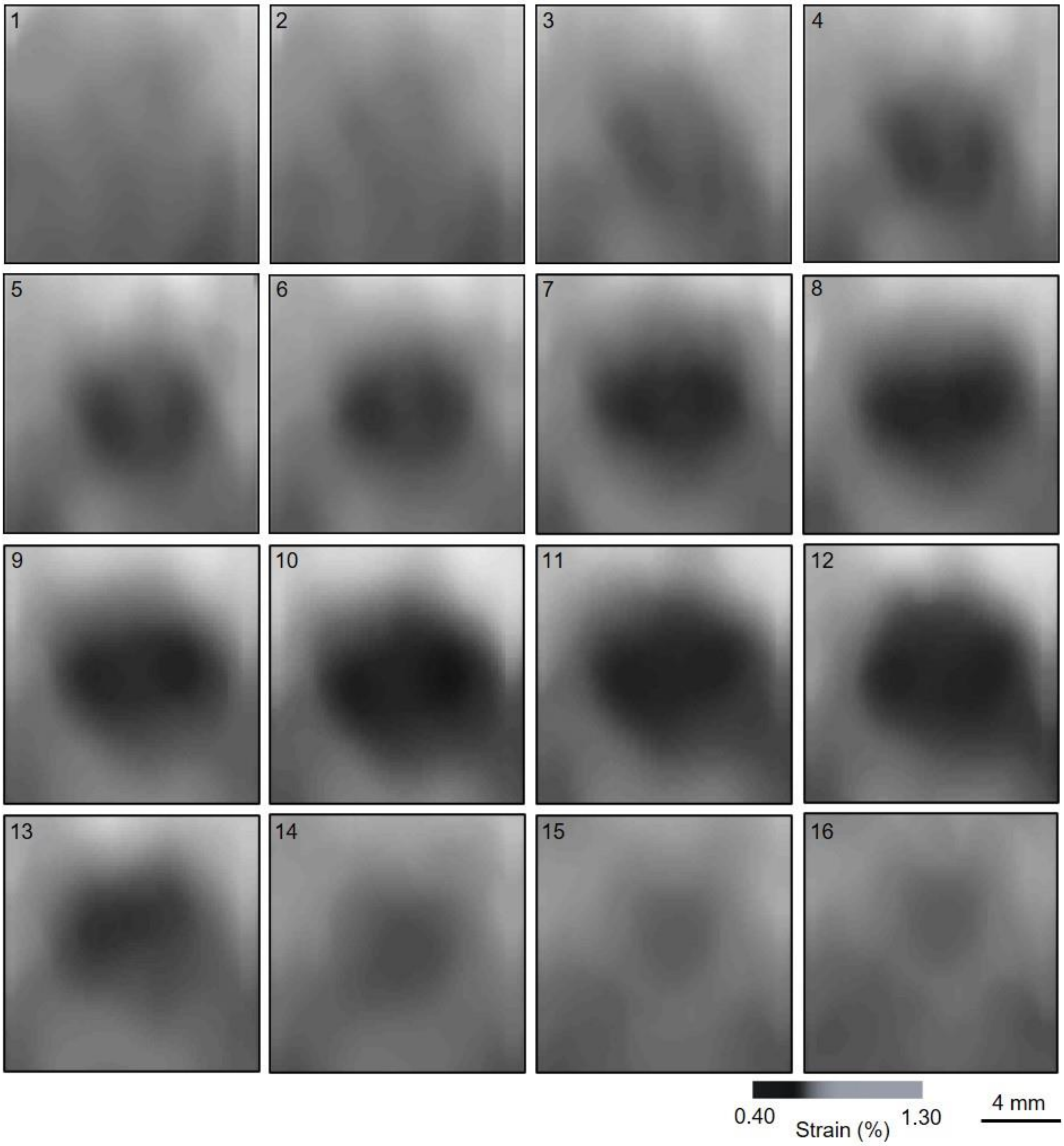

Supplementary Figure 35. 16 slices of 2D strain images of the commercial breast phantom by the stretchable ultrasonic array. Each slice of 2D strain image is generated by each 1×16 linear array in the stretchable ultrasonic array. These 2D images are used to reconstruct the 3D image. These figures share the same color bar and scale bar.

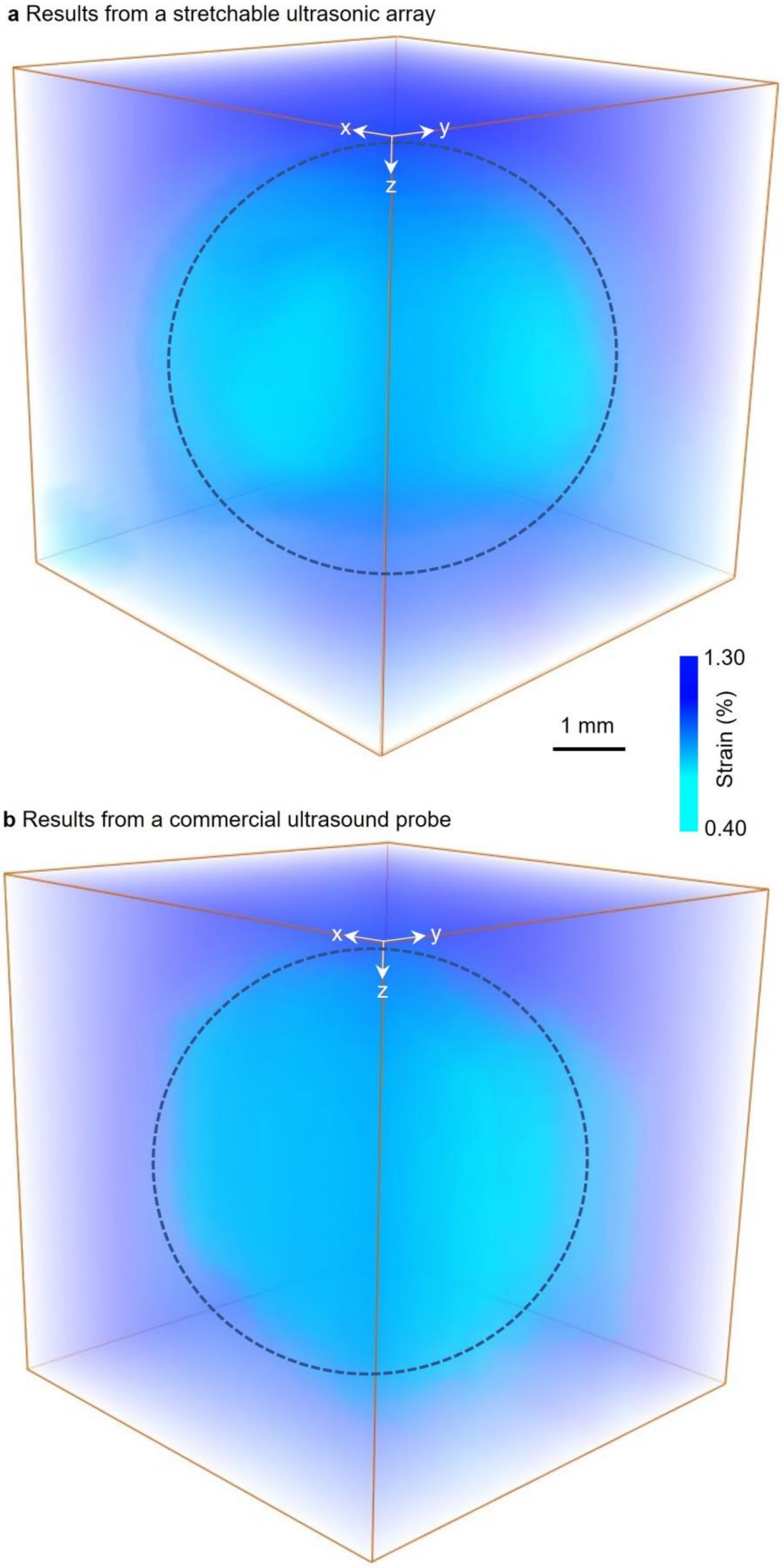

a Results from a stretchable ultrasonic array

b Results from a commercial ultrasound probe

Supplementary Figure 36. 3D strain images of the commercial breast phantom by the stretchable and commercial ultrasonic probes. The results by (**a**) the stretchable ultrasonic array and (**b**) the commercial ultrasound probe show high correspondence to each other in size, geometry, and strain distribution of the breast phantom. Both figures share the same colour bar and scale bar.

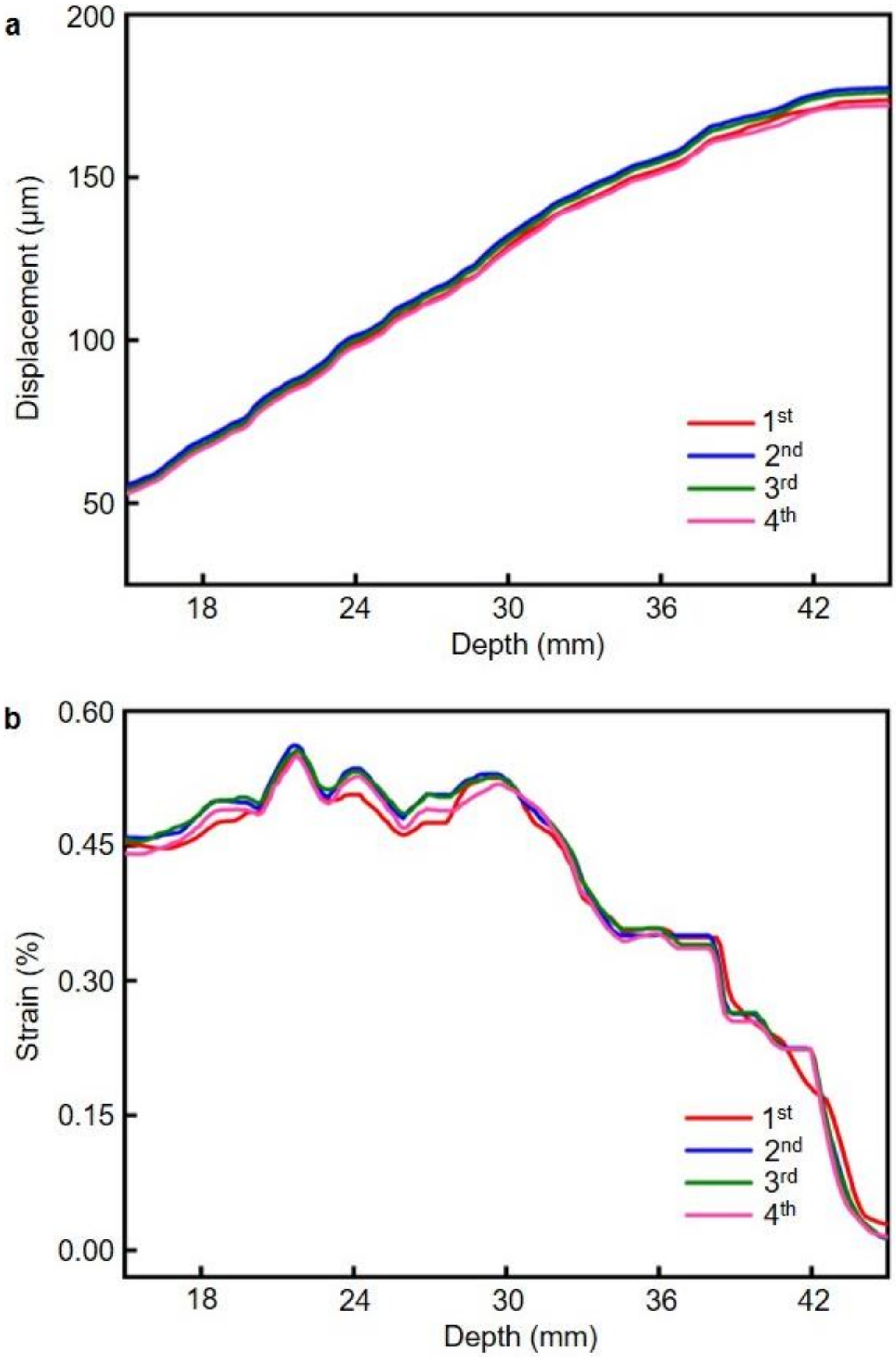

Supplementary Figure 37. Repetitive tests. Measurements of (**a**) the displacement and (**b**) the strain of a phantom four times. There is a three-minute interval between each measurement to allow the phantom to relax from the compressive to the original states. These measurements are highly reproducible.

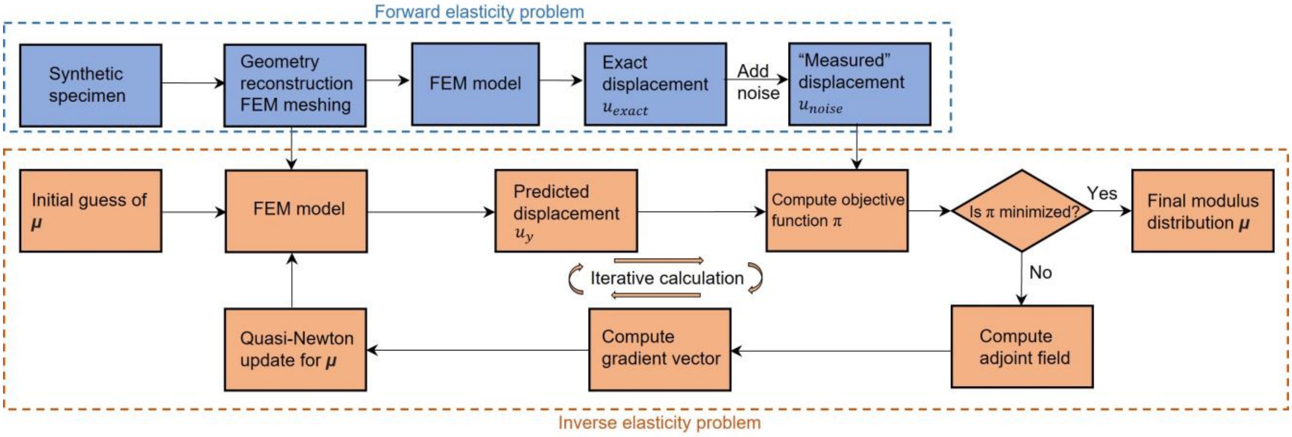

Supplementary Figure 38. Flow chart of the process for calculating the forward and inverse elasticity problem. Blue boxes demonstrate the workflow of developing synthetic specimens and solving the forward elasticity problems. Orange boxes demonstrate the workflow of calculating the inverse elasticity problem. Blue boxes demonstrate the interaction of the inverse elasticity problem with the experimental system. μ: modulus distribution; u_{exact}: exact displacement without adding noise; u_{noise}: the "measured" displacement field; u_y: the predicted displacement field; $\tilde{u}_y$: the measured displacement field; π: the objective function, as defined in equation (8).

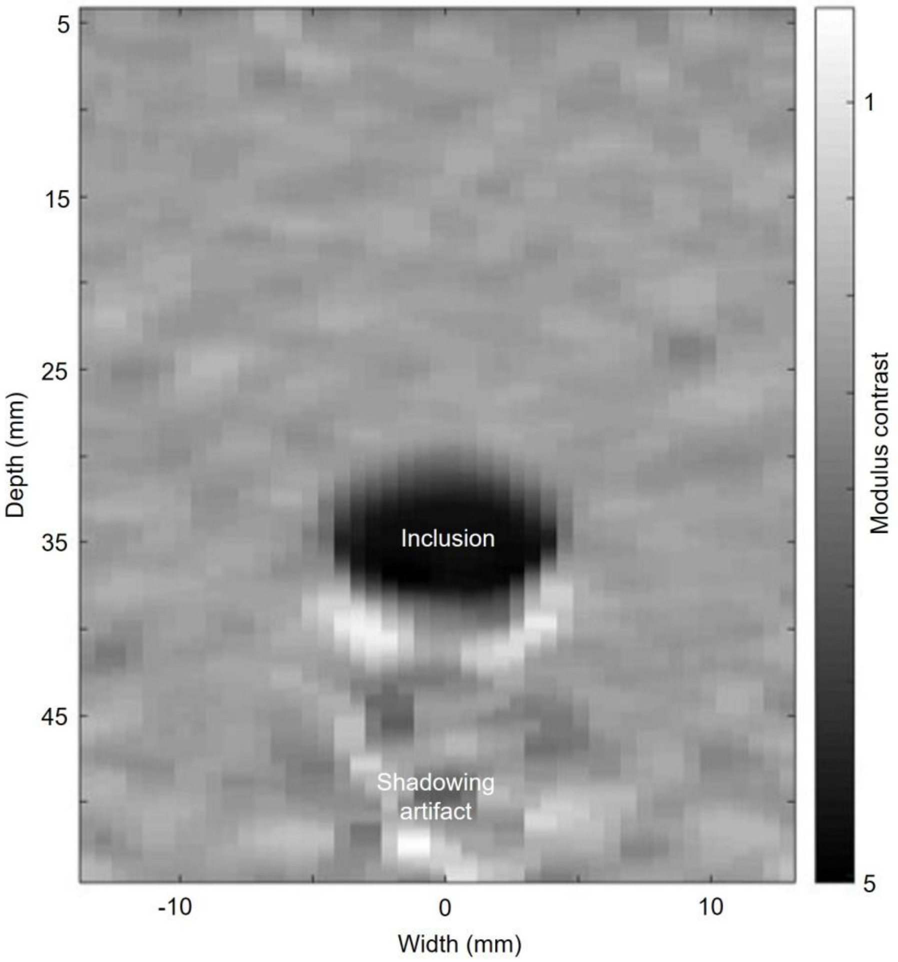

Supplementary Figure 39. Simulated shadowing artifacts. Shadowing artifacts in the elastogram are usually caused by the shielding of the inclusion[110]. Most of the ultrasound waves are bounced back by the inclusion. Only probes with high sonographic sensitivity can sense the weak signals below the inclusion and reconstruct the elastogram with minimal artifacts.

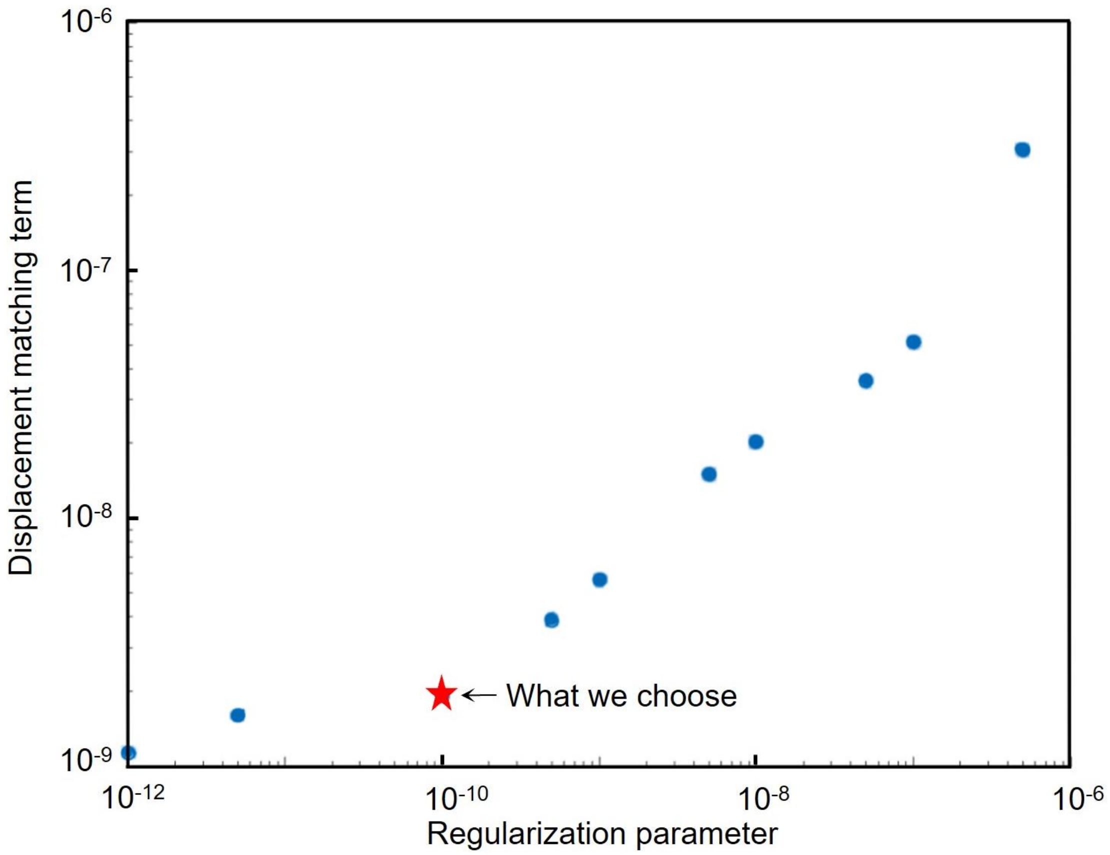

Supplementary Figure 40. The L-curve of calculating the inverse elasticity problem. An appropriate regularization parameter is required to reconstruct the displacement and modulus ratio fields. When selecting a large regularization parameter, the field will be very smooth but with small modulus contrast; and vice versa. In this work, we use 1×10^{-10} to optimally harmonize the levels of smoothness and contrast to get the best matching of the measured and predicted results.

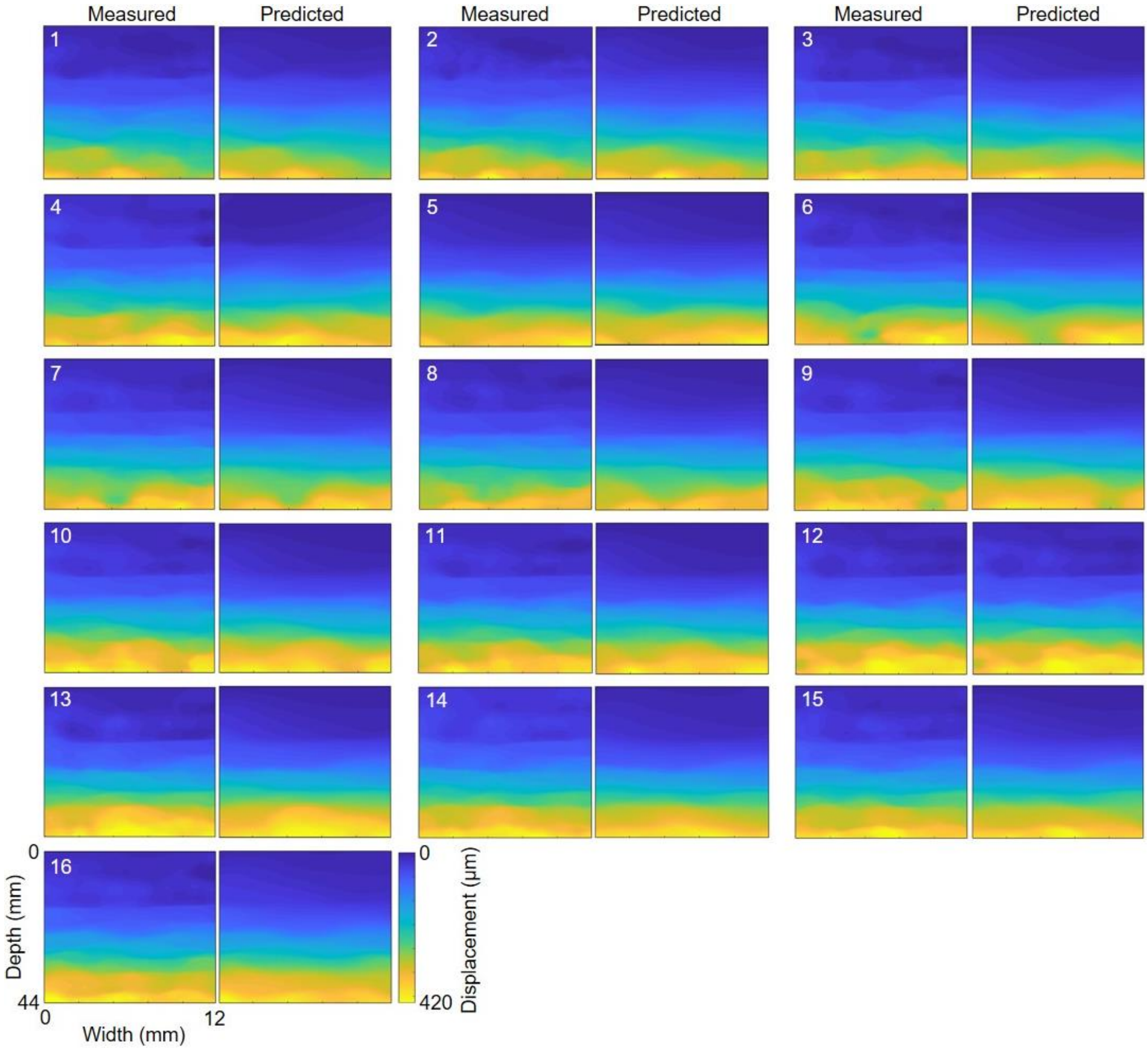

Supplementary Figure 41. Comparisons between the measured and predicted displacement fields of the porcine abdominal tissue. The prediction is made by calculating the inverse elasticity problem. Each 1×16 linear array in the stretchable ultrasonic array produces a 2D cross-sectional displacement field using the coherent compounding imaging strategy. The >97% matching shows the high correspondence between the measured and predicted fields, providing a solid foundation for generating a reliable and accurate 3D modulus distribution in this work.

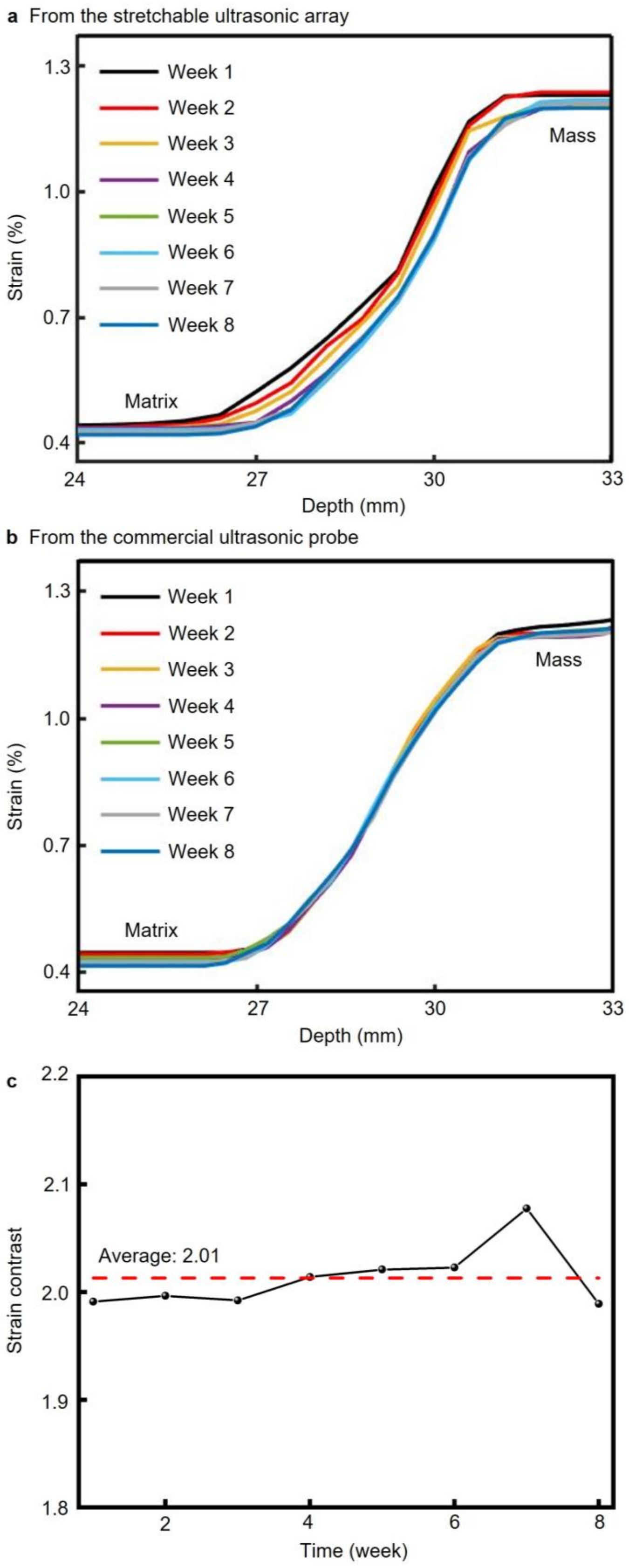

Supplementary Figure 42. Longitudinal studies of the strain curves of a commercial breast phantom. We use (**a**) the stretchable ultrasonic array and (**b**) a commercial ultrasonic probe to test the same commercial phantom over a duration of eight weeks, with one measurement per week. A linear motor was used for both devices to apply the same compressive strain to the target. Eight central lines of the strain fields, one per week, have been characterized, extracted, and plotted together. The results show the excellent accuracy and repeatability of the stretchable ultrasonic array for long-term monitoring. The little discrepancy of these curves from the stretchable ultrasonic array is probably due to the depolarization of the piezoelectric elements, which can potentially be fixed by re-poling with the strong electric field of 52.38 kV/cm for 15 minutes[111]. (**c**) The strain contrast monitored by the stretchable ultrasonic array, demonstrating the excellent repeatability of the device in longitudinal studies.

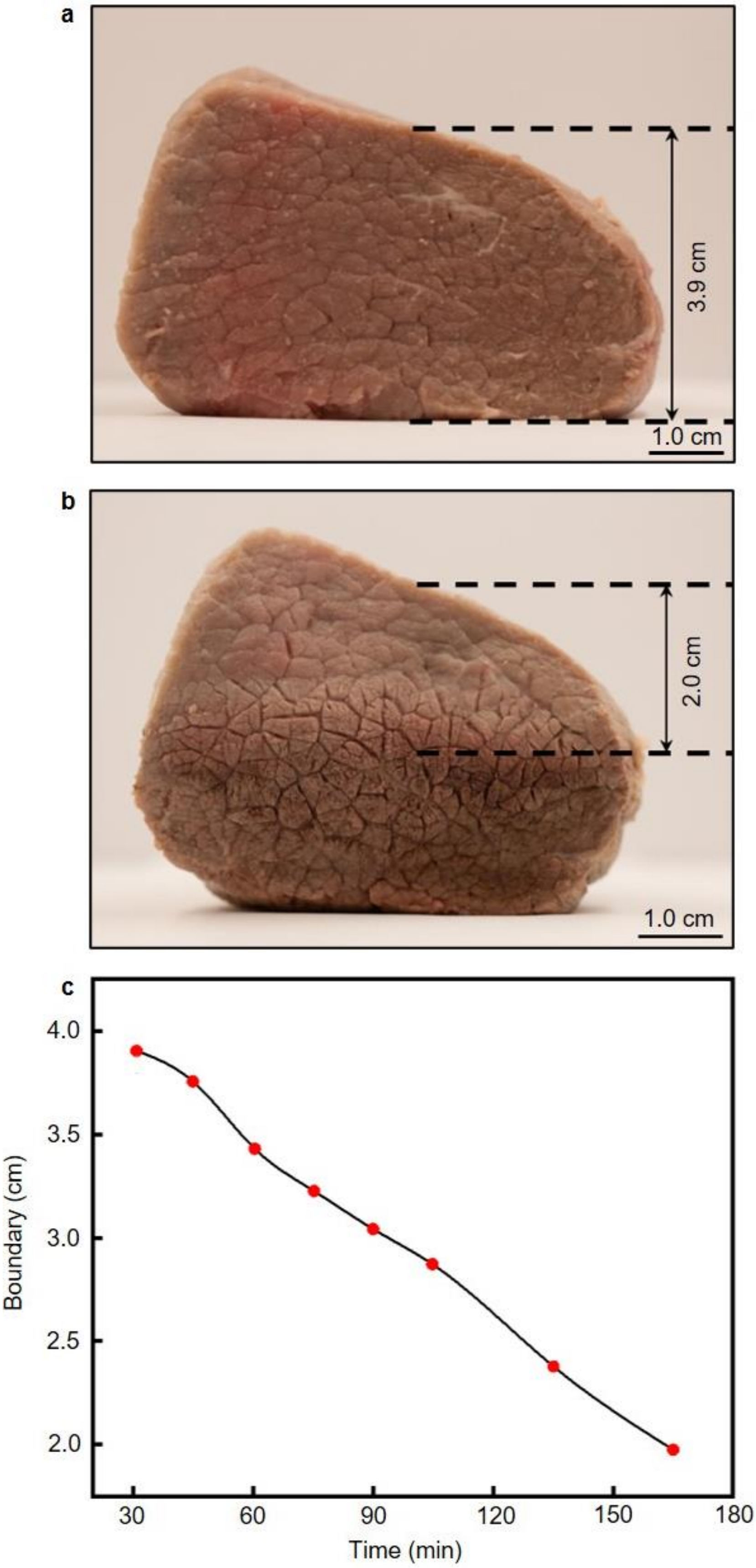

Supplementary Figure 43. Serial monitoring of the modulus evolution of a bovine gluteobiceps muscle. Optical images of the bovine gluteobiceps muscle (**a**) before and (**b**) after heating for 165 mins. The total thickness of the testing part is 3.9 cm. After heating, part of the specimen is stiffened, as evidenced by the boundary between stiff and soft tissues. (**c**) The boundary locations are plotted with the heating time. The probe position is defined as the origin.

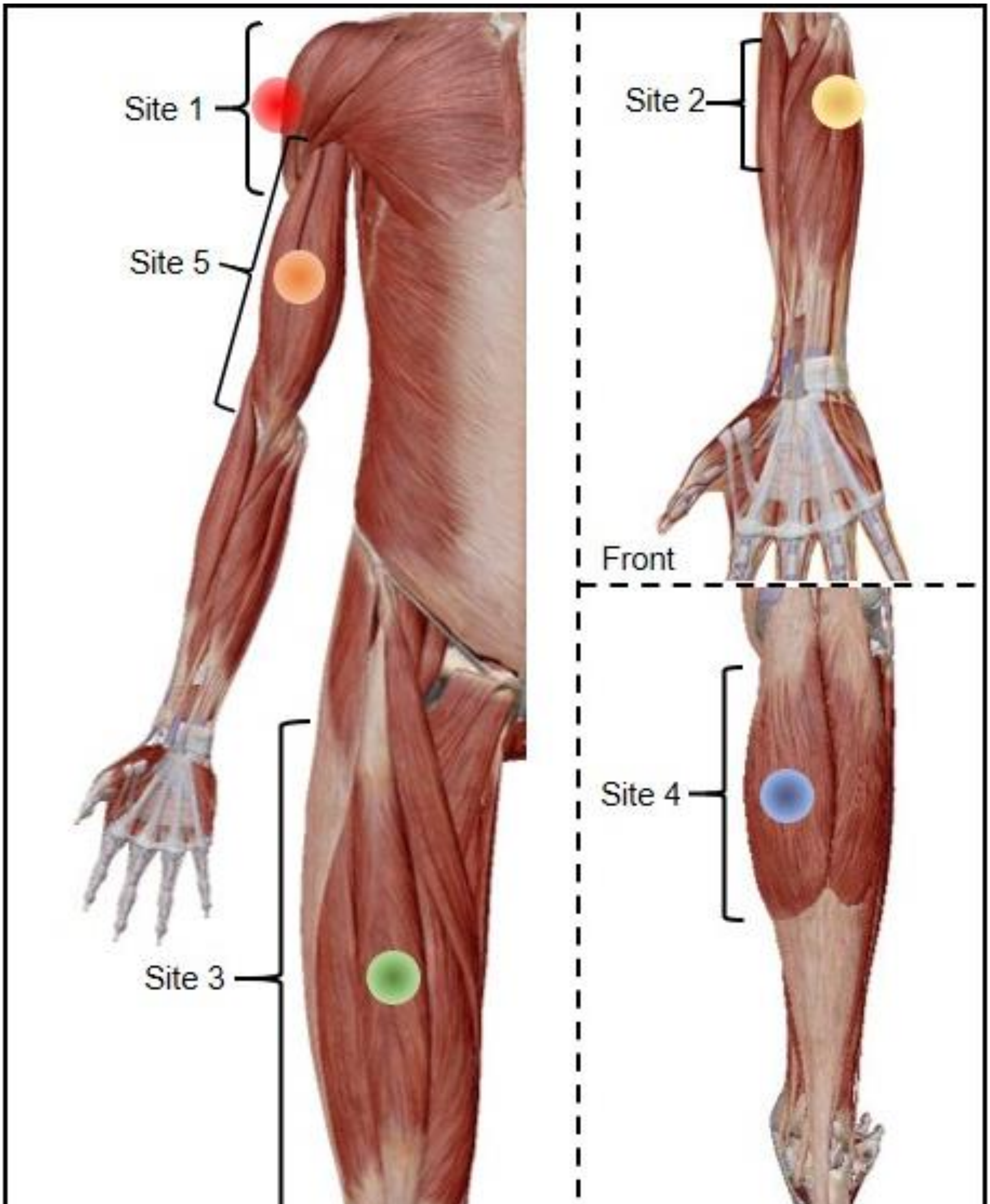

Supplementary Figure 44. A schematic plot demonstrating the anatomical structures and locations for in vivo measurements. Site 1: the later shoulder joint including the deltoid muscle belly. Site 2: the anterior arm including the palmaris longus muscle belly. Site 3: the anterior thigh from the upper pole of patella to the greater trochanter of femur. Site 4: the posterior calf including the medial head of the gastrocnemius. Site 5: the upper arm including the biceps brachii muscle belly.

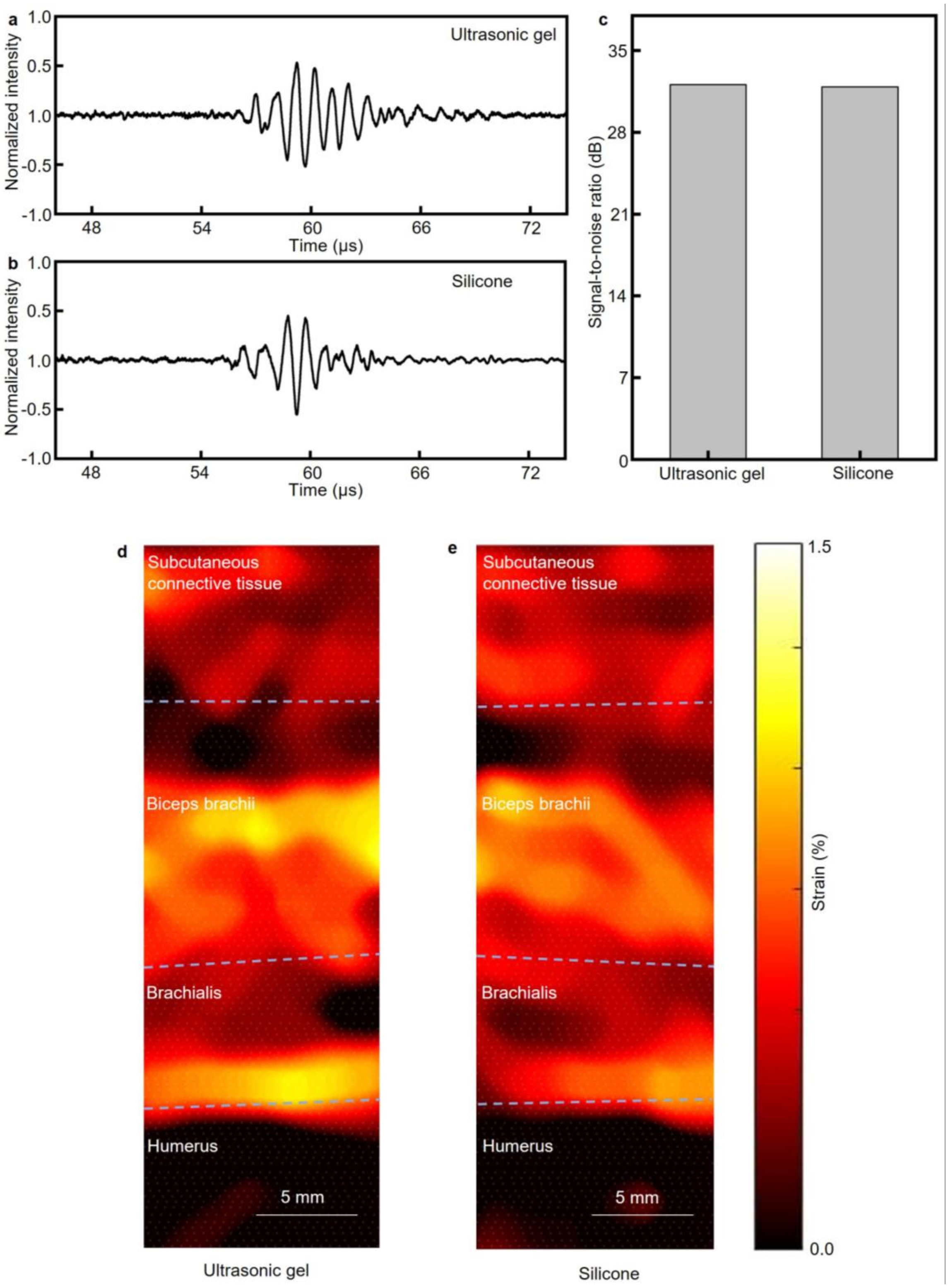

Supplementary Figure 45. Comparing the coupling performance between ultrasonic gel and Silicone. Received signals of the single transducer with (**a**) ultrasonic gel and (**b**) Silicone. The data intensity was normalized by the maximum intensity of the initial pulse. (**c**) Comparison of the corresponding signal-to-noise ratio of the received signals. Strain mapping of an upper arm by the stretchable ultrasonic array with different are labelled.

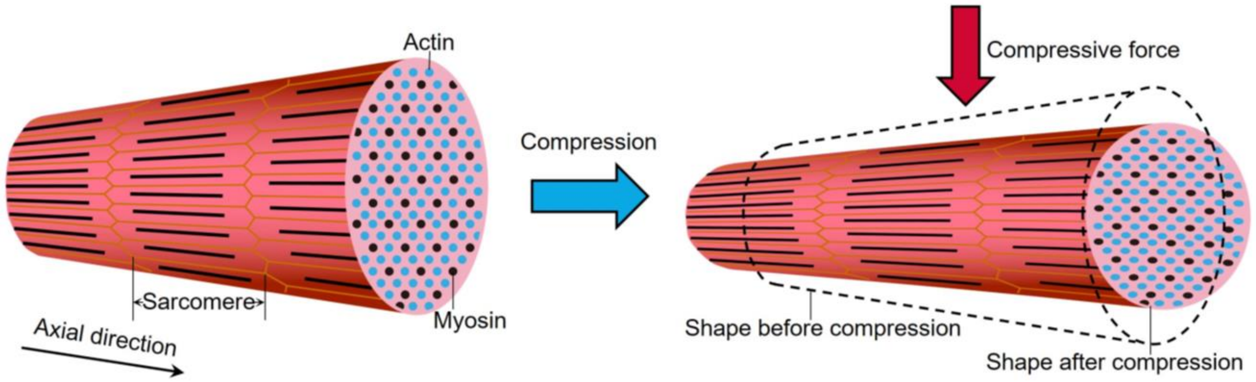

Supplementary Figure 46. The length of the muscle fiber before and after compression. Schematics showing the muscle fiber before (left) and after (right) compression. Muscle fibers will be extended along the axial direction after compression.

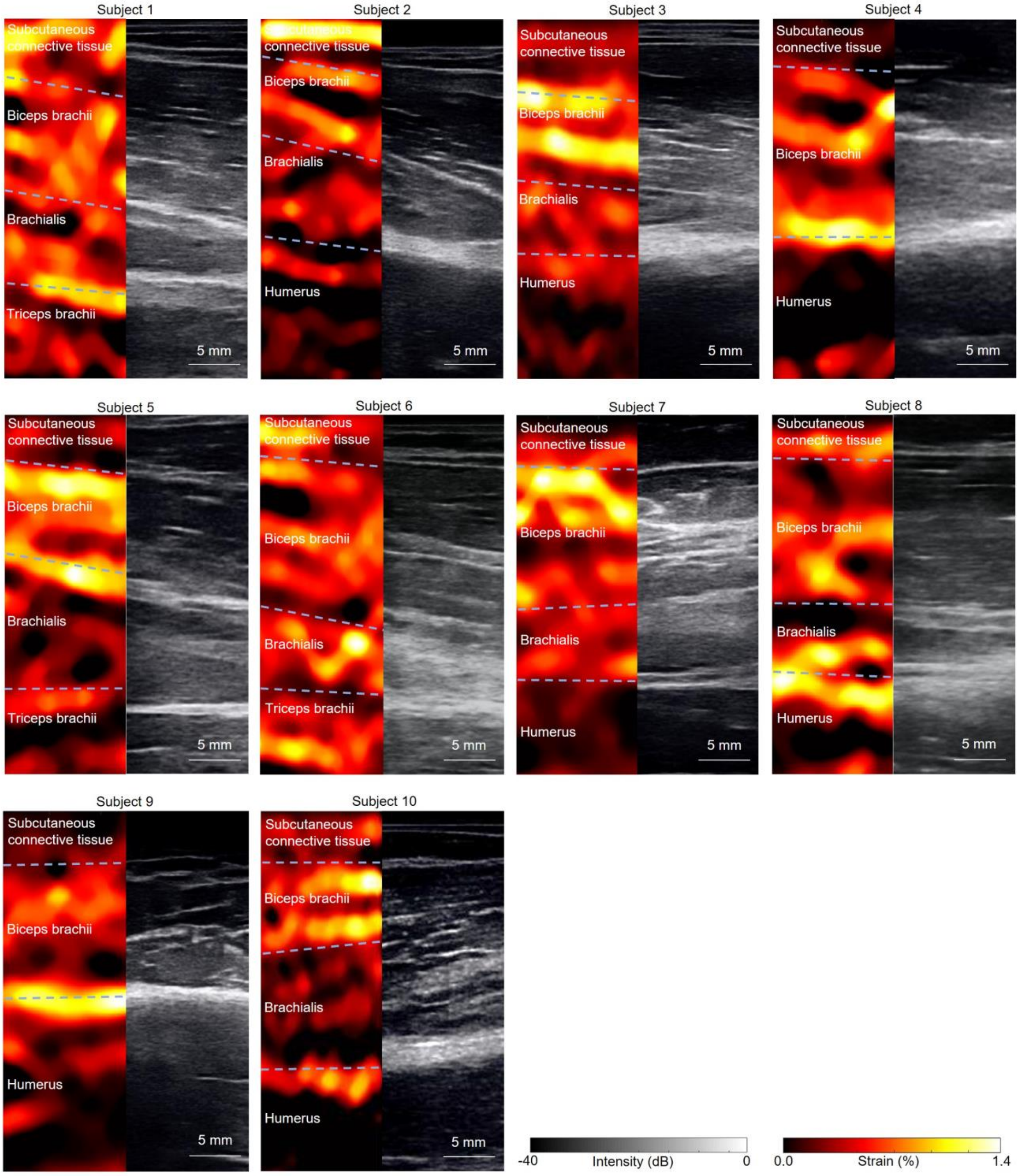

Supplementary Figure 47. Validating the device's feasibility on 10 subjects. Strain mapping results and the corresponding B-mode images of the upper arms of 10 subjects. Key anatomical structures are labelled in the strain images.

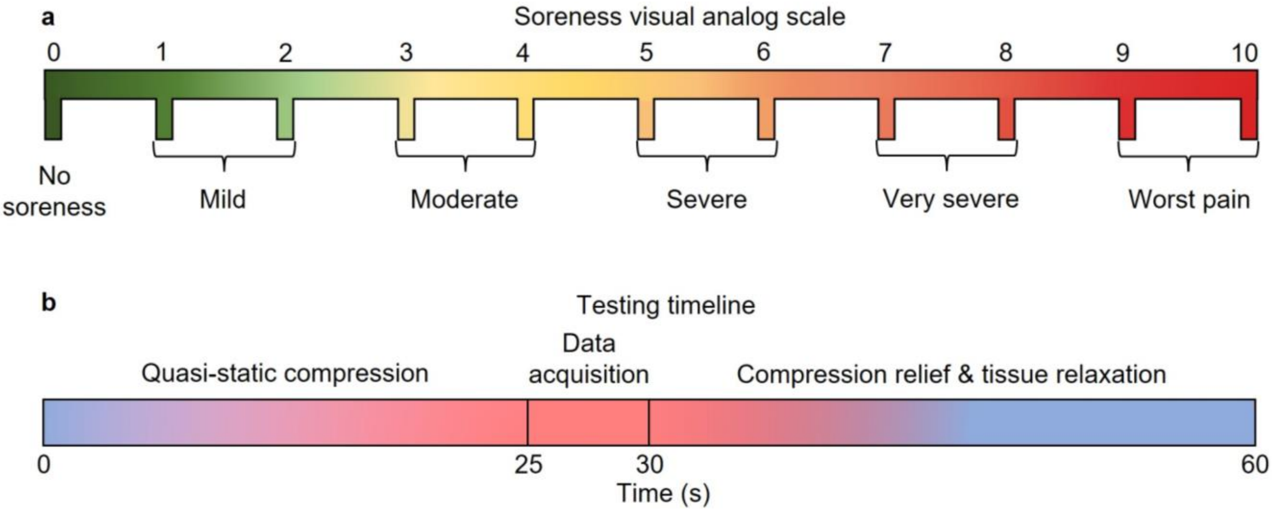

Supplementary Figure 48. Soreness visual analog scale and testing protocol. (**a**) Soreness visual analog scale interpreting the corresponding scores for different levels of soreness. (**b**) The testing protocol with all steps labelled. The test begins with quasi-static compression, which takes about 25 seconds. Then, multiple frames of data are acquired with a frame rate of 1 Hz. In the following ~30 s, the compression is relieved to make the tissue recover to the original state.

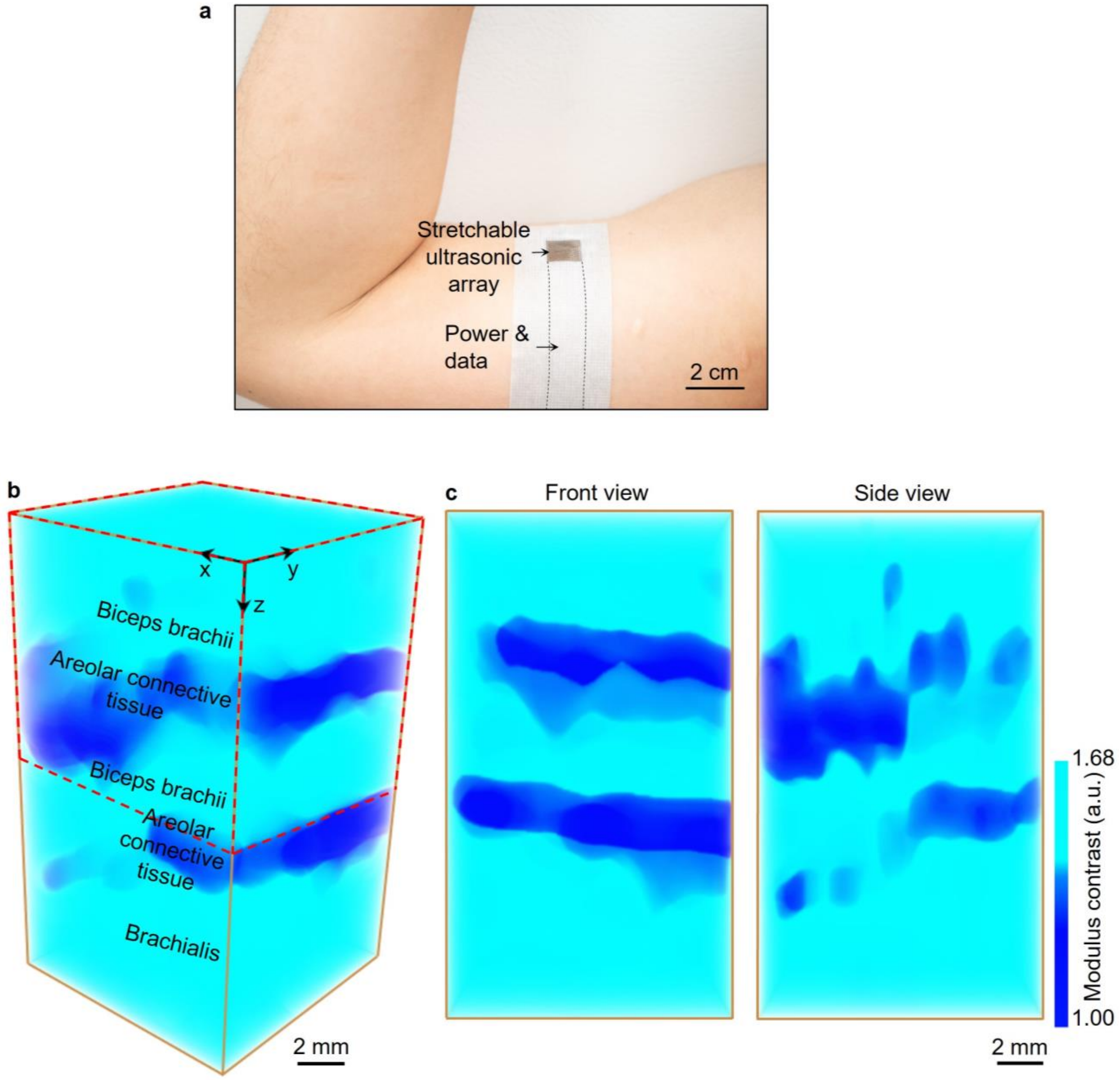

Supplementary Figure 49. A 3D elastographic reconstruction of the upper arm. (**a**) An optical image showing the device and the testing position. (**b**) 3D modulus distribution of the upper arm mapped by the stretchable ultrasonic array and (**c**) its front and side views. The areolar connective tissues contain sparsely arranged fibers and collagens. In addition, the arm was bent at 90 degrees when testing in this study, which left the areolar connective tissue in a relaxed state with fibers unstretched. Therefore, it has a lower stiffness of than muscles.

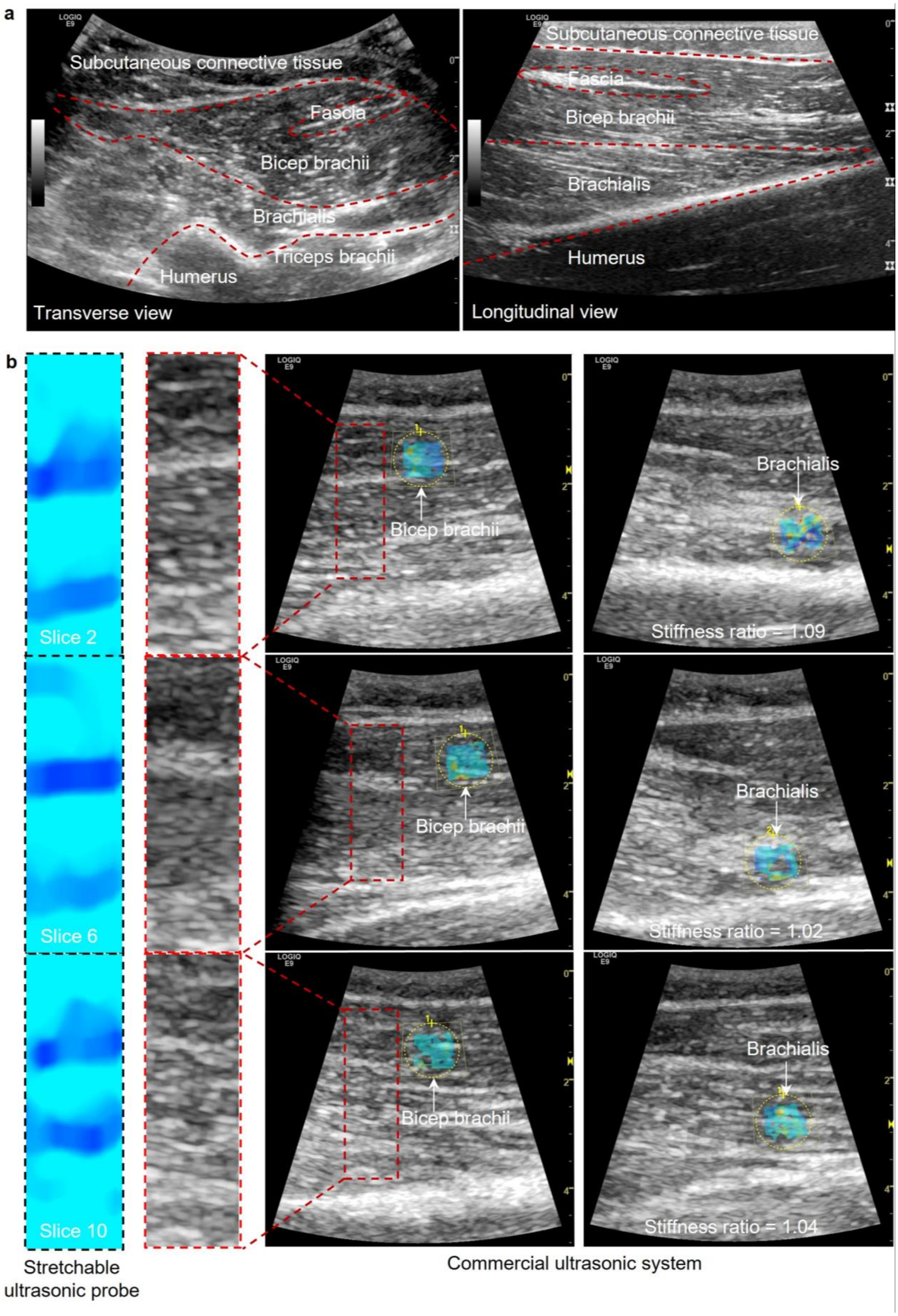

Supplementary Figure 50. The full view of the upper arm measured by a commercial ultrasonic system. (**a**) Transverse and longitudinal B-mode images of the upper arm by a commercial ultrasonic system. Representative anatomical structures have been labelled. (**b**) B-mode images overlaid with corresponding modulus measurements. Representative structures and the stiffness ratio of bicep brachii and brachialis from the commercial system highly match those from the stretchable ultrasonic patch.

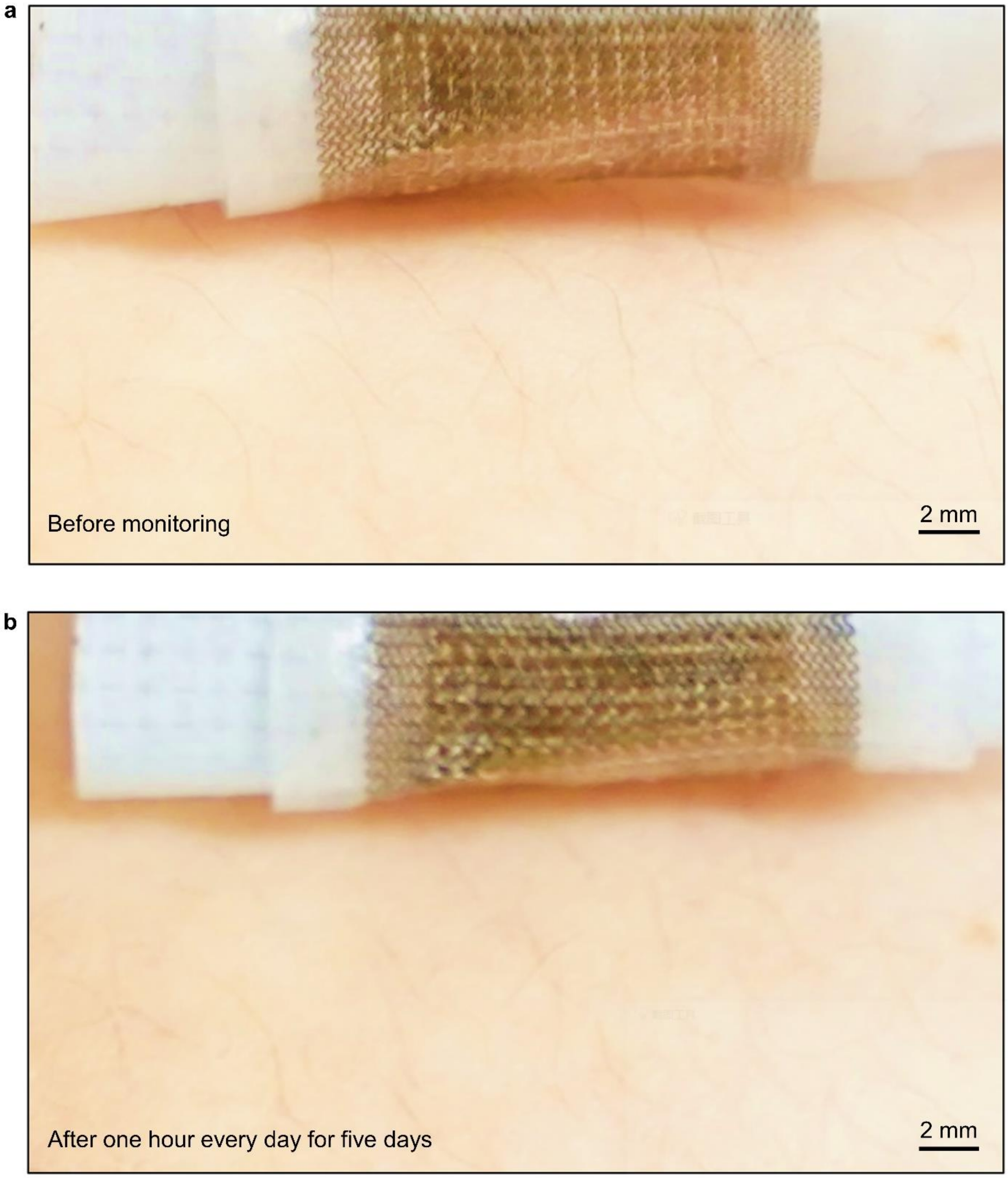

Supplementary Figure 51. Optical images of skin before and after monitoring. The device was mounted on the upper arm one hour every day for five days. No obvious skin irritation occurs, showing that the device is appropriate for long-time monitoring.

Table 1. Intra-session and inter-day reliabilities

	Intraclass correlation coefficient	Standard error of measurement (%)
Intra-session reliability	0.94	0.04
Inter-day reliability	0.95	0.03

Table S1. Reliability quantification in intra-session and inter-day testing. The intraclass correlation coefficient and the standard error of measurement are used to evaluate the relative and absolute reliabilities. Standard error of measurement is a statistical measure used to assess the error or uncertainty in a test or measurement. It measures the variation of the same test or measurement across multiple repetitions. The smaller the standard error of measurement, the higher the reliability of the test or measurement. Standard error of measurement is different from standard deviation that is used to quantify the amount of variation or dispersion in a set of data, representing the degree of difference between each data point and the mean value.

Movie S1. Simulation illustrating the principle of ultrasound elastography. The principle of ultrasound elastography is ultrasonographic imaging based on quasi-static compression. A model was built with a cubic matrix and a cylinder inclusion. The modulus of the inclusion is twice as high as that of the matrix. Before compression, the inclusion cannot be visualized. As the compression proceeds, the inclusion gradually appears.

Supplementary References

1 Fung, Y.-C. *Biomechanics: mechanical properties of living tissues*. (Springer Science & Business Media, 2013).

2 Voutouri, C. & Stylianopoulos, T. Accumulation of mechanical forces in tumors is related to hyaluronan content and tissue stiffness. *PLoS ONE* **13**, e0193801 (2018).

3 Dietrich, C. F. *et al.* Strain elastography-how to do it? *Ultrasound Int. Open* **3**, E137 (2017).

4 Botar-Jid, C. *et al.* The contribution of ultrasonography and sonoelastography in assessment of myositis. *Med. Ultrason.* **12**, 120-126 (2010).

5 Brandenburg, J. E. *et al.* Quantifying passive muscle stiffness in children with and without cerebral palsy using ultrasound shear wave elastography. *Dev. Med. Child Neurol.* **58**, 1288-1294 (2016).

6 Gao, J. *et al.* Quantitative ultrasound imaging to assess the biceps brachii muscle in chronic post-stroke spasticity: preliminary observation. *Ultrasound Med. Biol.* **44**, 1931-1940 (2018).

7 Illomei, G., Spinicci, G., Locci, E. & Marrosu, M. Muscle elastography: a new imaging technique for multiple sclerosis spasticity measurement. *Neurol. Sci.* **38**, 433-439 (2017).

8 Lv, F. *et al.* Muscle crush injury of extremity: quantitative elastography with supersonic shear imaging. *Ultrasound Med. Biol.* **38**, 795-802 (2012).

9 Lacourpaille, L. et al. Time-course effect of exercise-induced muscle damage on localized muscle mechanical properties assessed using elastography. *Acta Physiol.* **211**, 135-146 (2014).

10 Drakonaki, E. Ultrasound elastography for imaging tendons and muscles. *J. Ultrason.* **12**, 214 (2012).

11 Brandenburg, J. E. *et al.* Ultrasound elastography: the new frontier in direct measurement of muscle stiffness. *Arch. Phys. Med. Rehabil.* **95**, 2207-2219 (2014).

12 Gao, J., Du, L.-J., He, W., Li, S. & Cheng, L.-G. Ultrasound strain elastography in assessment of muscle stiffness in acute levodopa challenge test: a feasibility study. *Ultrasound Med. Biol.* **42**, 1084-1089 (2016).

13 Diridollou, S. *et al.* In vivo model of the mechanical properties of the human skin under suction. *Skin Res. Technol.* **6**, 214-221 (2000).

14 Samani, A., Zubovits, J. & Plewes, D. Elastic moduli of normal and pathological human breast tissues: an inversion-technique-based investigation of 169 samples. *Phys. Med. Biol.* **52**, 1565 (2007).

15 Sugihara, T., Ohura, T., Homma, K. & Igawa, H. The extensibility in human skin: variation according to age and site. *Br. J. Plast. Surg.* **44**, 418-422 (1991).

16 Bhushan, B. Nanotribological and nanomechanical properties of skin with and without cream treatment using atomic force microscopy and nanoindentation. *J. Colloid Interface Sci.* **367**, 1-33 (2012).

17 Marturano, J. E., Arena, J. D., Schiller, Z. A., Georgakoudi, I. & Kuo, C. K. Characterization of mechanical and biochemical properties of developing embryonic tendon. *Proc. Natl. Acad. Sci.* **110**, 6370-6375 (2013).

18 Jenkyn, T. R., Ehman, R. L. & An, K.-N. Noninvasive muscle tension measurement using the novel technique of magnetic resonance elastography (MRE). *J. Biomech.* **36**, 1917-1921 (2003).

19 Gennisson, J. L., Deffieux, T., Fink, M. & Tanter, M. Ultrasound elastography: principles and techniques. *Diagn. Interv. Imaging* **94**, 487-495 (2013).

20 Dong, L. *et al.* Quantitative compression optical coherence elastography as an inverse elasticity problem. *IEEE J. Sel. Top. Quantum Electron.* **22**, 277-287 (2015).

21 Garra, B. S. Elastography: history, principles, and technique comparison. *Abdom. Imaging* **40**, 680-697 (2015).

22 Kennedy, B. F., Kennedy, K. M. & Sampson, D. D. A review of optical coherence elastography: fundamentals, techniques and prospects. *IEEE J. Sel. Top. Quantum Electron.* **20**, 272-288 (2013).

23 Varghese, T. Quasi-Static Ultrasound Elastography. *Ultrasound Clin.* **4**, 323-338 (2009).

24 Ferreira, E. R., Oberai, A. A. & Barbone, P. E. Uniqueness of the elastography inverse problem for incompressible nonlinear planar hyperelasticity. *Inverse Prob.* **28**, 065008 (2012).

25 Ta, C. N., Eghtedari, M., Mattrey, R. F., Kono, Y. & Kummel, A. C. 2-tier in-plane motion correction and out-of-plane motion filtering for contrast-enhanced ultrasound. *Invest. Radiol.* **49**, 707-719 (2014).

26 Kaminski, J. T., Rafatzand, K. & Zhang, H. K. in *Medical Imaging 2020: Image-Guided Procedures, Robotic Interventions, and Modeling.* 113151D (International Society for Optics and Photonics, 2020).

27 Gerlach, S., Kuhlemann, I., Ernst, F., Fürweger, C. & Schlaefer, A. Impact of robotic ultrasound image guidance on plan quality in SBRT of the prostate. *Brit. J. Radiol.* **90**, 20160926 (2017).

28 Bowles, F. A. Observations on attenuation and shear-wave velocity in fine-grained, marine sediments. *J. Acoust. Soc. Am.* **101**, 3385-3397 (1997).

29 W. Urban, M., Alizad, A., Aquino, W., F. Greenleaf, J. & Fatemi, M. A review of vibro-acoustography and its applications in medicine. *Curr. Med. Imaging Rev.* **7**, 350-359 (2011).

30 Pandya, H. J., Chen, W., Goodell, L. A., Foran, D. J. & Desai, J. P. Mechanical phenotyping of breast cancer using MEMS: a method to demarcate benign and cancerous breast tissues. Lab Chip **14**, 4523-4532 (2014).

31 Dagdeviren, C. *et al.* Conformal piezoelectric systems for clinical and experimental characterization of soft tissue biomechanics. *Nat. Mater.* **14**, 728-736 (2015).

32 Li, B., Shi, Y., Fontecchio, A. & Visell, Y. Mechanical imaging of soft tissues with a highly compliant tactile sensing array. *IEEE. Trans. Biomed. Eng.* **65**, 687-697 (2017).

33 Yu, X. *et al.* Needle-shaped ultrathin piezoelectric microsystem for guided tissue targeting via mechanical sensing. *Nat. Biomed. Eng* **2**, 165-172 (2018).

34 Romero-Laorden, D. *et al.* Analysis of parallel computing strategies to accelerate ultrasound imaging processes. *IEEE Trans. Parallel Distrib. Syst.* **27**, 3429-3440 (2016).

35 Yuan, J. *et al.* Real-time photoacoustic and ultrasound dual-modality imaging system facilitated with graphics processing unit and code parallel optimization. *J. Biomed. Opt.* **18**, 086001 (2013).

36 Goncharsky, A. V. & Romanov, S. Y. Supercomputer technologies in inverse problems of ultrasound tomography. *Inverse Prob.* **29**, 075004 (2013).

37 Wang, Y. *et al.* Assessment of tumor stiffness with shear wave elastography in a human prostate cancer xenograft implantation model. *J. Ultrasound Med.* **36**, 955-963 (2017).

38 Giovagnorio, F., Andreoli, C. & De Cicco, M. L. Color Doppler sonography of focal lesions of the skin and subcutaneous tissue. *J. Ultrasound Med.* **18**, 89-93 (1999).

39 Drakonaki, E., Allen, G. & Wilson, D. Ultrasound elastography for musculoskeletal applications. *Brit. J. Radiol.* **85**, 1435-1445 (2012).

40 Cafarelli, A., Miloro, P., Verbeni, A., Carbone, M. & Menciassi, A. Speed of sound in rubber-based materials for ultrasonic phantoms. *J. Ultrasound* **19**, 251-256 (2016).

41 Song, Z., Ding, H., Li, J. & Pu, H. Circular curve-fitting method for field surveying data with correlated noise. *J. Surv. Eng.* **144**, 04018010 (2018).

42 Wang, Z., Ha, S. & Kim, K. in *Medical Imaging 2012: Ultrasonic Imaging, Tomography, and Therapy.* 83201L (International Society for Optics and Photonics, 2012).

43 Porras, D., Sepúlveda-Sepúlveda, A. & Csapó, T. G. in *2019 International Joint Conference on Neural Networks (IJCNN).* 1-8 (IEEE, 2019).

44 Quinsac, C., Basarab, A., Kouamé, D. & Grégoire, J.-M. in *2010 IEEE International Ultrasonics Symposium.* 363-366 (IEEE, 2010).

45 Hore, A. & Ziou, D. in *2010 20th international conference on pattern recognition.* 2366-2369 (IEEE, 2010).

46 Luo, J. & Konofagou, E. E. A fast normalized cross-correlation calculation method for motion estimation. *IEEE Trans. Ultrason. Ferroelectr. Freq. Control* **57**, 1347-1357 (2010).

47 Konofagou, E. E., Ophir, J., Kallel, F. & Varghese, T. Elastographic dynamic range expansion using variable applied strains. *Ultrason. Imaging* **19**, 145-166 (1997).

48 Varghese, T. & Ophir, J. A theoretical framework for performance characterization of elastography: The strain filter. *IEEE Trans. Ultrason. Ferroelectr. Freq. Control* **44**, 164-172 (1997).

49 Yang, F., Chong, A., Lam, D. C. C. & Tong, P. Couple stress based strain gradient theory for elasticity. *Int. J. Solids Struct.* **39**, 2731-2743 (2002).

50 Kallel, F. & Ophir, J. A least-squares strain estimator for elastography. *Ultrason. Imaging* **19**, 195-208 (1997).

51 Tanaka, M. & Dulikravich, G. S. *Inverse problems in engineering mechanics*. (Elsevier, 1998).

52 Tikhonov, A. N., Goncharsky, A., Stepanov, V. & Yagola, A. G. *Numerical methods for the solution of ill-posed problems*. Vol. 328 (Springer Science & Business Media, 2013).

53 Goenezen, S. *et al.* Linear and nonlinear elastic modulus imaging: an application to breast cancer diagnosis. *IEEE Trans. Med. Imaging* **31**, 1628-1637(2012).

54 Francois Dord, J. *et al.* in *Ultrasound Elastography for Biomedical Applications and Medicine* 129-142 (John Wiley & Sons., Hoboken, 2018).

55 Gokhale, N. H., Barbone, P. E. & Oberai, A. A. Solution of the nonlinear elasticity imaging inverse problem: the compressible case. *Inverse Prob.* **24**, 045010 (2008).

56 Hansen, P. C. Analysis of discrete ill-posed problems by means of the L-curve. *SIAM Rev.* **34**, 561-580 (1992).

57 Oberai, A. A., Gokhale, N. H. & Feijóo, G. R. Solution of inverse problems in elasticity imaging using the adjoint method. *Inverse Prob.* **19**, 297 (2003).

58 Hughes, T. J. *The finite element method: linear static and dynamic finite element analysis*. (Courier Corporation, 2012).

59 Byrd, R. H., Lu, P., Nocedal, J. & Zhu, C. A limited memory algorithm for bound constrained optimization. *SIAM J. Sci. Comput.* **16**, 1190-1208 (1995).

60 Barbone, P. E. & Oberai, A. A. Elastic modulus imaging: some exact solutions of the compressible elastography inverse problem. *Phys. Med. Biol.* **52**, 1577 (2007).

61 Song, D., Hugenberg, N. & Oberai, A. A. Three-dimensional traction microscopy with a fiber-based constitutive model. *Comput. Methods Appl. Mech. Eng.* **357**, 112579 (2019).

62 Flynn, J. R., Ward, S., Abich, J. & Poole, D. in *International Conference on Engineering Psychology and Cognitive Ergonomics.* 23-30 (Springer, 2013).

63 Jang, K.-I. *et al.* Self-assembled three dimensional network designs for soft electronics. *Nat. Commun.* **8**, 1-10 (2017).

64 Sirohi, J. & Chopra, I. Fundamental understanding of piezoelectric strain sensors. *J. Intell. Mater. Syst. Struct.* **11**, 246-257 (2000).

65 Ma, Y. T., Zhong, J., Zhang, L. & Wu, Y. L. in *Applied Mechanics and Materials.* 24-30 (Trans Tech Publications Ltd, 2012).

66 Wang, C. *et al.* Continuous monitoring of deep-tissue haemodynamics with stretchable ultrasonic phased arrays. *Nat. Biomed. Eng.* **5**, 749-758 (2021).

67 Papadacci, C., Bunting, E. A. & Konofagou, E. E. 3D Quasi-Static Ultrasound Elastography With Plane Wave In Vivo. *IEEE Trans. Med. Imaging* **36**, 357-365 (2017).

68 Srinivasan, S., Righetti, R. & Ophir, J. Trade-offs between the axial resolution and the signal-to-noise ratio in elastography. *Ultrasound Med. Biol.* **29**, 847-866 (2003).

69 Varghese, T. & Ophir, J. An analysis of elastographic contrast-to-noise ratio. *Ultrasound Med. Biol.* **24**, 915-924 (1998).

70 Montaldo, G., Tanter, M., Bercoff, J., Benech, N. & Fink, M. Coherent plane-wave compounding for very high frame rate ultrasonography and transient elastography. *IEEE Trans. Ultrason. Ferroelectr. Freq. Control* **56**, 489-506 (2009).

71 Joshi, M., Dillman, J. R., Towbin, A. J., Serai, S. D. & Trout, A. T. MR elastography: high rate of technical success in pediatric and young adult patients. *Pediatr. Radiol.* **47**, 838-843 (2017).

72 Niitsu, M., Michizaki, A., Endo, A., Takei, H. & Yanagisawa, O. Muscle hardness measurement by using ultrasound elastography: a feasibility study. *Acta Radiol.* **52**, 99-105 (2011).

73 Kishimoto, K., Sakuraba, K., Kubota, A. & Fujita, S. The effect of concentric and eccentric exercise on muscle hardness. *Juntendo Med. J.* **64**, 371-378 (2018).

74 Abdi, H. Coefficient of variation. *Encycl. Res. Des.* **1**, 169-171(2010).

75 Hotfiel, T. *et al.* Advances in delayed-onset muscle soreness (DOMS): Part I: Pathogenesis and diagnostics. *Sportverletz.-Sportschaden* **32**, 243-250 (2018).

76 Skinner, H. A. *The origin of medical terms*. (Baltimore: Williams & Wilkins, 1961).

77 Kargarfard, M. *et al.* Efficacy of massage on muscle soreness, perceived recovery, physiological restoration and physical performance in male bodybuilders. *J. Sports Sci.* **34**, 959-965 (2016).

78 Petrofsky, J. S. *et al.* Cold vs. Heat after exercise—Is there a clear winner for muscle soreness. *J. Strength Cond. Res.* **29**, 3245-3252 (2015).

79 Paulsen, G. *et al.* Time course of leukocyte accumulation in human muscle after eccentric exercise. *Med. Sci. Sports Exerc.* **42**, 75-85 (2010).

80 Smith, L. L. *et al.* The effects of athletic massage on delayed onset muscle soreness, creatine kinase, and neutrophil count: a preliminary report. *J. Orthop. Sports Phys. Ther.* **19**, 93-99 (1994).

81 Lavender, A. P. & Nosaka, K. A light load eccentric exercise confers protection against a subsequent bout of more demanding eccentric exercise. *J. Sci. Med. Sport* **11**, 291-298 (2008).

82 Semmler, J. G., Tucker, K. J., Allen, T. J. & Proske, U. Eccentric exercise increases EMG amplitude and force fluctuations during submaximal contractions of elbow flexor muscles. *J. Appl. Physiol.* **103**, 979-989 (2007).

83 Tosovic, D., Than, C. & Brown, J. The effects of accumulated muscle fatigue on the mechanomyographic waveform: implications for injury prediction. *Eur. J. Appl. Physiol.* **116**, 1485-1494 (2016).

84 Mueller-Wohlfahrt, H.-W. *et al.* Terminology and classification of muscle injuries in sport: the Munich consensus statement. *Br. J. Sports Med.* **47**, 342-350 (2013).

85 Howell, J., Chleboun, G. & Conatser, R. Muscle stiffness, strength loss, swelling and soreness following exercise ‐ induced injury in humans. *J. Physiol.* **464**, 183-196 (1993).

86 Proske, U. & Morgan, D. L. Muscle damage from eccentric exercise: mechanism, mechanical signs, adaptation and clinical applications. *J. Physiol.* **537**, 333-345 (2001).

87 Proske, U. & Allen, T. J. Damage to skeletal muscle from eccentric exercise. *Exerc. Sport Sci. Rev.* **33**, 98-104 (2005).

88 Murayama, M., Nosaka, K., Yoneda, T. & Minamitani, K. Changes in hardness of the human elbow flexor muscles after eccentric exercise. *Eur. J. Appl. Physiol.* **82**, 361-367 (2000).

89 Green, M., Sinkus, R., Gandevia, S., Herbert, R. & Bilston, L. Measuring changes in muscle stiffness after eccentric exercise using elastography. *NMR Biomed.* **25**, 852-858 (2012).

90 Pearcey, G. E. *et al.* Foam rolling for delayed-onset muscle soreness and recovery of dynamic performance measures. *J. Athl. Train.* **50**, 5-13 (2015).

91 Heiss, R. *et al.* Advances in delayed-onset muscle soreness (DOMS)–part II: treatment and prevention. *Sportverletz.-Sportschaden* **33**, 21-29 (2019).

92 Peake, J. M., Neubauer, O., Della Gatta, P. A. & Nosaka, K. Muscle damage and inflammation during recovery from exercise. *J. Appl. Physiol.* **122**, 559-570 (2017).
93 Guo, J. *et al.* Massage alleviates delayed onset muscle soreness after strenuous exercise: a systematic review and meta-analysis. *Front. Physiol.* **8**, 747 (2017).
94 Dupuy, O., Douzi, W., Theurot, D., Bosquet, L. & Dugué, B. An evidence-based approach for choosing post-exercise recovery techniques to reduce markers of muscle damage, soreness, fatigue, and inflammation: a systematic review with meta-analysis. *Front. Physiol.* **9**, 403 (2018).
95 Nelson, N. Delayed onset muscle soreness: is massage effective? *J. Bodyw. Mov. Ther.* **17**, 475-482 (2013).
96 Mayer, J. M. *et al.* Continuous low-level heat wrap therapy for the prevention and early phase treatment of delayed-onset muscle soreness of the low back: a randomized controlled trial. *Arch. Phys. Med. Rehabil.* **87**, 1310-1317 (2006).
97 Petrofsky, J. *et al.* The efficacy of sustained heat treatment on delayed-onset muscle soreness. *Clin. J. Sport Med.* **27**, 329-337 (2017).
98 Malanga, G. A., Yan, N. & Stark, J. Mechanisms and efficacy of heat and cold therapies for musculoskeletal injury. *Postgrad. Med.* **127**, 57-65 (2015).
99 Jeon, S., Ye, X., Miller, W. M. & Song, J. S. Effect of repeated eccentric exercise on muscle damage markers and motor unit control strategies in arm and hand muscle. *J. Sport Health Sci.* **4**, 44-53 (2022).
100 Clarkson, P. M., Nosaka, K. & Braun, B. Muscle function after exercise-induced muscle damage and rapid adaptation. *Med. Sci. Sports Exerc.* **24**, 512-520 (1992).
101 Nosaka, K., Sakamoto, K., Newton, M. & Sacco, P. The repeated bout effect of reduced-load eccentric exercise on elbow flexor muscle damage. *Eur. J. Appl. Physiol.* **85**, 34-40 (2001).
102 Liu, T., Babaniyi, O. A., Hall, T. J., Barbone, P. E. & Oberai, A. A. Noninvasive in-vivo quantification of mechanical heterogeneity of invasive breast carcinomas. *PLoS ONE* **10**, e0130258 (2015).
103 Qian, X. *et al.* Ultrasonic micro-elastography for accessing biomechanical properties of the cornea. *Invest. Ophthalmol. Visual Sci.* **58**, 4331-4331 (2017).
104 Qian, X. *et al.* Ultrasonic elastography to assess biomechanical properties of the optic nerve head and peripapillary sclera of the eye. *Ultrasonics* **110**, 106263 (2020).
105 Debernard, L., Robert, L., Charleux, F. & Bensamoun, S. F. Analysis of thigh muscle stiffness from childhood to adulthood using magnetic resonance elastography (MRE) technique. *Clin. Biomech.* **26**, 836-840 (2011).
106 Loomba, R. *et al.* Novel 3D magnetic resonance elastography for the noninvasive diagnosis of advanced fibrosis in NAFLD: a prospective study. *Am. J. Gastroenterol.* **111**, 986 (2016).
107 Kennedy, B. F. *et al.* In vivo three-dimensional optical coherence elastography. *Opt. Express* **19**, 6623 (2011).
108 Kang, H. *et al.* 2D Ultrasonic Array-based Optical Coherence Elastography. *IEEE Trans. Ultrason. Ferroelectr. Freq. Control* **68***, 1096-1104* (2020).
109 Seo, C. H. & Yen, J. T. Sidelobe suppression in ultrasound imaging using dual apodization with cross-correlation. *IEEE Trans. Ultrason. Ferroelectr. Freq. Control* **55**, 2198-2210 (2008).
110 Bouchet, P. *et al.* Artifacts and technical restrictions in 2D shear wave elastography. *Ultraschall Med. Eur. J. Ultrasound* **41**, 267-277 (2020).
111 Hu, H. *et al.* Stretchable ultrasonic transducer arrays for three-dimensional imaging on complex surfaces. *Sci. Adv.* **4**, eaar3979 (2018).